AN EXPERIMENTAL STUDY OF CONCURRENT METHODS FOR ADAPTIVELY CONTROLLING VERTICAL TAIL BUFFET IN HIGH PERFORMANCE AIRCRAFT

A Thesis
Presented to
The Academic Faculty

by

Patrick J. Roberts

In Partial Fulfillment
of the Requirements for the Degree
Doctor of Philosophy in the
School of Aerospace Engineering

Georgia Institute of Technology
Fall 2007

AN EXPERIMENTAL STUDY OF CONCURRENT METHODS FOR ADAPTIVELY CONTROLLING VERTICAL TAIL BUFFET IN HIGH PERFORMANCE AIRCRAFT

Approved by:

Dr. S. Hanagud, Committee Chair
School of Aerospace Engineering
Georgia Institute of Technology

Dr. S. Hanagud, Advisor
School of Aerospace Engineering
Georgia Institute of Technology

Dr. J. Craig
School of Aerospace Engineering
Georgia Institute of Technology

Dr. E. Johnson
School of Aerospace Engineering
Georgia Institute of Technology

Dr. Calise
School of Aerospace Engineering
Georgia Institute of Technology

Date Approved: 31 August 2007

The dedication of my thesis is to my parents, Jim and Patricia Roberts,
my wife, Felicia, my daughter, Nicole and my son, Derek,
for their continued support in completing my doctorate.

ACKNOWLEDGEMENTS

I would like first to thank my advisor, Dr. Sathya Hanagud, for his time, his support and the knowledge that he shared with me during the course of this research work. I would like to thank Dr. Jun Bong Yang for his help with the adaptive neural network. I would like to thank all the members of my PhD committee. I would like to thank Dr. Jeff Jagoda for his support. I would also like to thank Dr. Maxime Bayon De Noyer for the time and effort he took to teach me about tail buffet, smart structures and experimental techniques. I would like to thank Dr. Xia Lu for her help in the thermodynamic background of piezoceramics and for all for all of those interesting technical discussions. I would like to thank Umesh Patel for all of his assistance. I would like to thank the machine shop staff of the School of Aerospace Engineering at the Georgia Institute of Technology, Harry Rudd and Wayne Springfield, who built parts for the wind tunnel model. Finally, I would like to thank God for giving me the opportunity to pursue my passion.

Contents

List of Tables

List of Figures

SUMMARY

High performance twin-tail aircraft, like the F-15 and F/A-18, encounter a condition known as tail buffet. At high angles of attack, vortices are generated at the wing fuselage interface (shoulder) or other leading edge extensions. These vortices are directed toward the twin vertical tails. When the flow interacts with the vertical tail it creates pressure variations that can oscillate the vertical tail assembly. This results in fatigue cracks in the vertical tail assembly that can decrease the fatigue life and increase maintenance costs.

For many years, research has been conducted to understand this phenomenon of buffet and to reduce its adverse effects on the fatigue life of aerospace structures. Many proposed solutions to this tail buffet problem have had limited success. These include strengthening the tail, modifying the vortex flow, using an active rudder control, and leading edge extensions. Some of the proposed active controls include piezoelectric actuators. Recently, an offset piezoceramic stack actuator was used on an F-15 wind tunnel model to control buffet induced vibrations at high angles of attack. The controller was based on the acceleration feedback control methods.

In this thesis a procedure for designing the offset piezoceramic stack actuators is developed. This design procedure includes determining the quantity and type of piezoceramic stacks used in these actuators. The changes of stresses, in the vertical tail caused by these actuators during an active control, are investigated.

In many cases, linear controllers are very effective in reducing vibrations. However, during flight, the natural frequencies of the vertical tail structural system changes as the airspeed increases. This in turn, reduces the effectiveness of a linear controller. Other causes such as the unmodeled dynamics and nonlinear effects due to debonds also reduce the effectiveness of linear controllers. In this thesis, an adaptive neural network is used to augment the linear controller to correct these effects.

Chapter I

LITERATURE REVIEW

1.1 Separated flows over a Twin-tailed aircraft

High angles of attack change the airflow over the wing-fuselage structure of a high performance twin-tail aircraft which results in the formation of vortices. These vortices separate and impact the vertical tails as shown in Figure 1.

Figure 1: Unsteady flow of an F/A-18 at high angle of attack

The buffet phenomenon was first reported in 1931[23]. In 1948, Outman[72] studied the problem of eliminating separation and buffet-induced vibrations. In 1955, Fung[25] defined buffeting as the irregular motion of a structure or parts of a structure excited by turbulence in the flow. In 1958, Pearcey[78] used wind tunnel tests to develop a method to observe the flow separation effects at the trailing edge of an aircraft wing. In 1975, Bachalo[5] was able

to study the flow separation in three dimensions by using wedges affixed to flat plates.

In 1990 Tai[100] used a grid zone approach to characterize the flow separation patterns for an F-14A wing with twin tails. Tai observed a massive flow separation at Mach numbers as low as 0.6. Komerath[48, 49], in 1990, conducted a study to define the low-speed, high angle of attack aerodynamic flow of an F-15. Komerath observed when using a steady laser sheet visualization technique on a 1/32 scale model that flow separation and reversal propagated on the outside of the vertical tails with an increasing angle of attack. However,the flow on the inner surfaces always remained attached. This condition caused pressure differences between the inboard and outboard sides of the vertical tail and resulted in an oscillatory motion of the vertical tail.

In 1971, Soderman[96] demonstrated that at maximum lift an aircraft with a single T-tail experienced severe tail buffet. In 1994, X-29 flight testing was halted due to severe tail buffet[34]. On this aircraft accelerometers on the vertical tail measured 110g at 16 Hz, at 25 degrees angle of attack. In 2000, Breitsamter[9] investigated the tail buffet problem on the single vertical tail of the EF-2000.

1.2 Tail Buffet of High Performance Twin Tail Aircraft

In the early seventies, cracks on the F-15 vertical tails were observed six months after they were put into service[21]. These cracks allowed moisture into the honeycomb structure of the vertical tail assembly and caused the forward box to corrode and caused skin disbonds.

In 2001, Tavoularis[101, 102] performed an experimental investigation on the effect of sideslip and rolling maneuvers on tail buffet. The speed range of this study was Mach 0.25 to 0.80. At roll angles of 30 degrees, there was a significant reduction in the normal forces.

In 2004, Morton[63] developed an improved model of the loading on the vertical tail by separated vortices on the F/A-18 using Detached Eddy Simulation (DES). Anderson[2] conducted preliminary studies on the F-22 aircraft at low air speeds to characterize the tail buffet on this aircraft. He found that the F-22 did suffer from the tail buffet effect. LEX fences reduced but did not eliminate the tail buffet[2]. The testing was at angles of attack up to 32 degrees.

1.3 Tail Buffet Alleviation

1.3.1 Passive approaches

Passive control methods have been studied to reduce tail buffet induced vibrations. Corrective actions, in the 1970's, consisted of design improvements to reduce stress concentrations. Later models of the F-15 experienced higher flight loads that caused the tail buffet induced vibrations to be dominated by the second bending mode[21]. Because the second mode caused severe curvature in the upper portion of the tail, the solution to this problem was to stiffen the torque box. In 1993, Ferman et al.[21] proposed a solution to stiffen the vertical tail structure by designing a bonded exoskin. The promise of this exoskin solution was that it would reduce the vibrations in the vertical tail without reinforcements of the secondary structure. The added mass was a total of eight pounds per vertical tail. An issue with this solution was the delamination of the exoskin itself and increase of the stresses away from the exoskin.

In 1994, Gee[27] numerically investigated the effect of a fore body tangential slot-blowing on an F/A-18 aircraft. The 16-inch slot was located 3 in. and 11 in. aft of the nose of the aircraft. The wind tunnel tests showed a slight reduction in the tail buffet induced vibrations. Designs of new aircraft have considered one of the loading conditions to be the dynamic buffet load.

The use of small fences at F/A-18 leading edge extensions(LEX)[52, 26, 79, 37, 36, 93, 92, 91, 51, 61] to reduce buffet loads have been widely studied. LEX fences were very effective at low angles of attack. Their effectiveness was greatly reduced at high angles of attack where the buffet conditions were at their worst.

In 2000, Sheta[89] developed models to investigate the effect of stream wise fences on the twin-tail buffet of a generic fighter aircraft. Twin stream wise fences were located at the 30% chord-station of the delta wing. The results indicated that these fences were effective in reducing the aerodynamic loading that caused buffet, especially at angles of attack less than 30 degrees.

In 2002, Ghee[28] investigated various fillet shapes at the strake-wing juncture of a 76/40 degree double-delta wing model. The angles of attack were varied from -2 to 40 degrees.

The tunnel dynamic pressure was 26.74 psf and the Reynolds number was 1.3×10^6. A diamond fillet shape was found to reduce tail buffet measured pressures by as much as 60% compared to a parabolic fillet and shift the tail buffet to a higher frequency. Linear and parabolic fillet shapes were found to increase tail buffet above the baseline case.

1.3.2 Active Control

Passive control efforts of tail buffet have contributed to a reduction of the fatigue damage. The passive systems added additional weight to the tail structure. Active control of tail buffet induced vibrations were considered to reduce the added weight.

In 1995, Ashley[84, 4] suggested the use of the rudder itself as the "effector" on the F/A-18 to reduce the magnitude of the transfer function between the pressure differential of the two sides of the vertical tail and the auto power spectra of the rudder bending moment. Sensors were in the form of accelerometers. A signal proportional to the acceleration was then multiplied by a gain and directly fed back to control the rudder angle that reduced the RMS level of the bending moment. This control scheme produced a 33% reduction in RMS moment at 32 degrees AOA and 300 psf. Some of the drawbacks of this control scheme were that the reaction time of the rudder was slow and the control scheme was not as effective at lower frequencies as it was at higher frequencies. This same control scheme was applied to the F-15 at its worse buffet conditions of $\alpha = 22$ degrees and 245 psf. In this case, the RMS was sufficiently reduced but instabilities did set in.

In 1995 Lazarus et al.[50] performed a numerical study to assess the effectiveness of piezoelectric wafer actuators and LQG control to reduce tail buffet vibrations in an F/A-18 tail. One hundred and six actuator pairs were placed in the model on both skins of the vertical tail. The actuators had a maximum thickness of 0.15 inches. These actuators were placed inside the tail skin near expected high strain locations. Each actuator induced as much as 200 microstrains, displaying the need for multiple actuators. This finite element model was very detailed in that it included the plant model, structural dynamics, unsteady aerodynamic forces, dynamics of the sensors, actuators, anti-aliasing filters, LQG controller, and amplifiers. Actual flight data was used to evaluate the effectiveness of this control

scheme. The added weight of this system was approximately twenty three pounds. The theoretical results showed that greater than 50% reduction in RMS strain and greater than 60% increase in damping in the first mode was realized, for less than an 8% increase in weight.

In 1996, Moore[62] used over one hundred piezoceramic wafers bonded to the inside of the vertical tail skin to achieve a 57% reduction in worst case buffet conditions. A high percentage of the strain in the vertical tail structural system during these buffet induced vibrations was in the skin that made this solution very appealing. The sensors used were strain gage rosettes and the control scheme was MIMO LQG. The issue with this solution was the installation of the actuators and sensors required that the tail skin must be completely removed. In that same year, Hauch[35] developed the Active Vertical Tail (AVT) which successfully reduced the buffet response of structures by utilizing piezoelectric actuators, strain gauge sensors, and simple control techniques. The AVT was a 5%-scale, aeroelastically tailored structure with twin vertical tails that exhibited vibration responses similar to a full-scale aircraft structure. It designed such that it's piezoelectric actuators could provide control authority to control the first two bending modes. Piezoceramic wafers were installed on the vertical tail spars. The AVT was wind tunnel tested on a generic twin-tailed, double-delta fighter model at angles of attack and dynamic pressures representative of actual aircraft flight envelopes including -25 to 65 degrees angle of attack. At high angles of attack, leading-edge vortices of the models impinge upon the AVT. The control scheme used in this work was proportional, integral, and differential (PID) feedback. Measurements were taken from accelerometer sensors which were used with the piezoelectric actuators and collocated strain gauge sensors to either minimize the acceleration at the AVTs tip or the strain at the root of the tail. Control gains were verified to be a nonlinear function of angle of attack, dynamic pressure, and location of the actuator and sensor pair. PSD showed a 65% decrease in vibrations. The RMS response below 200 Hz was reduced by approximately 20%.

1.3.2.1 Piezoelectric stack actuators and vibration control

Piezoceramic actuators have been produced in many different forms which include PZT wafers and bimorphs. One form of piezocermic actuator was in the form of piezoceramic stacks. Piezoceramic stacks were used as force inducing actuators in truss elements[81] and for vibration reduction in plates by placing the stack between a stiffener and the plate[108]. These actuators were also implemented as bending moment inducing actuators by placing the stack within cutouts in stiff beams and plates[82] or mounting the stack in an external assembly for active tail buffet control[60].

In 1997, Nitzsche et al.[68, 69, 70] evaluated two different active control strategies for tail buffet alleviation. These two methods were the active rudder approach[4] and a new smart structures strain actuation approach. The two control strategies that were studied used Linear Quadratic Gaussian (LQG) method of the Optimum Control Theory.

In 1997, Moses[64], as part of the Actively Controlled Response of Buffet Affected Tails (ACROBAT) program, used a 1/16th scale model of an F/A-18 to compare two types of actuators for active damping of buffet-induced vibrations; (1) An active rudder and (2) piezoelectric-wafer actuators. When controlling vibrations at the first bending mode using a simple gain in a SISO control scheme the piezoelectric actuators were able to reduce the PSD up to 60% at 37 degrees angle of attack.

In 1999, Suleman[99] also used piezoceramic wafers for sensing and actuation on an experimental sweptback flat wing model. The control objective was to control buffet induced vibrations and flutter in the wing. The wing model consisted of a NACAOO12 airfoil which contained a rectangular aluminum plate structure. The rectangular plan form wing had a 240 mm span and 140 mm chord. Twelve piezoceramic actuator patches (38 x 25 x 0.2mm) were bonded to the top and bottom of the wing near the cantilevered end. Two patches were used for sensing. The control law was a proportional feedback control. In the buffet test the closed loop tests showed a 30% reduction in vibration.

Maxime Bayon De Noyer et al.(1999, 2003)[16] designed an actuator assembly called the Offset Piezoceramic Stack Actuator (OPSA) (See figures 2 and 3). The control moments were achieved by placing a piezoceramic stack, which used the more efficient d_{33} coefficient,

parallel to the controlled structure at a selected distance from the neutral axis and at a selected orientation. The actuator assembly was made of two structural elements bonded to the controlled system. The active element, a piezoceramic stack, was clamped with rounded contacts between the blocks for reliability issues. Tests were conducted using a 1/16th scale model of an F-15. A 100mV/g accelerometer was placed on the upper trailing tip of the starboard vertical tail. In this position the sensor observed both bending and torsion modes. Two types of acceleration feedback control were used (1) crossover design (the frequency of the controller was the same as the plant frequency to be controlled) and (2) H_2 optimization. Wind tunnel tests were conducted with 9 psf and 22 degrees angle of attack. The controllers were designed to control both the first bending and torsional mode. Results showed that RMS acceleration reduction by a factor of 5 (80% reduction) was obtained. This was the largest reduction compared to previous proposed techniques.

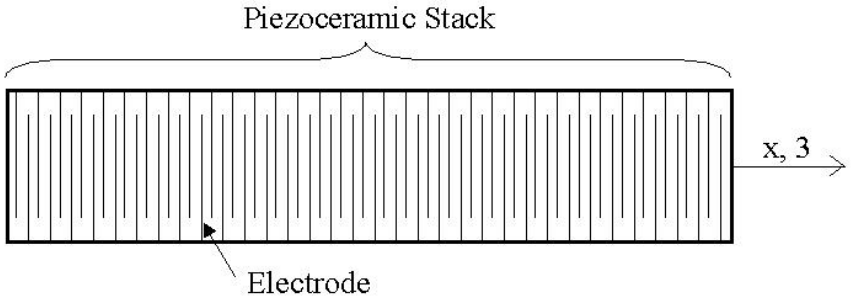

Figure 2: Co-fired Piezoceramic Stack Configuration

Also, in 1999 Spangler and Jacques[97] were able to test the Buffet Load Alleviation system (BLA), on a full size F/A-18. The actuators in the BLA system consisted of several layers of 0.020 inch thick piezoceramic material (type PZT-SA). These actuators were both along the elastic axis and parallel to the elastic axis (See Figure 4). The exact locations of the actuators were derived from a finite element model using the strain distributions of the tail in modes that were to be controlled. 50% reduction in RMS when compared to the open loop was achieved but only at very benign conditions. However, they found that linear amplifiers were not capable of achieving 50% reduction in the most severe buffet conditions. This research also indicated the limitation of piezoceramic wafers which use the

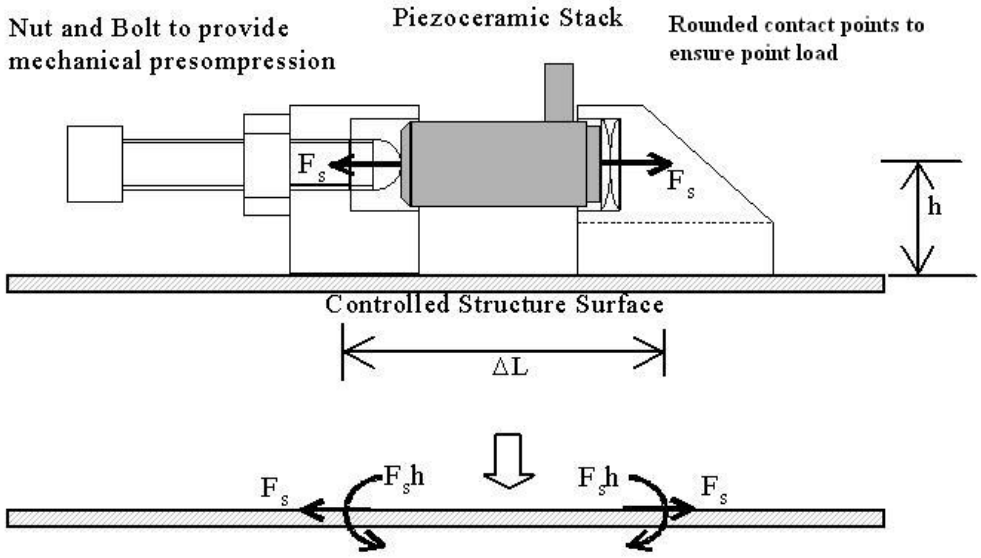

Figure 3: Offset Piezoceramic Stack Actuator

d_{31} coefficient. Another drawback of this system was an additional weight of 225 lb. per tail.

1.3.2.2 Redistribution of stresses due to actuators

Finite element modeling methods have been used to obtain stresses around the bonding edges of piezoelectric wafers that were bonded to a beam. In 1996 Varadan[103] used a finite element model to create a cantilever structure containing a viscoelastic material (VEM) layer sandwiched between a piezoelectric actuator and the base structure. This hybrid arrangement was called an active constrained layer damper (ACLD). Vibrations caused a shear strain in the core made of VEM which, in turn, dissipated the energy which reduced the magnitude of vibrations. The control law used in this work was a velocity feedback controller. This work showed that stresses at the "bond edges" and in the structures in the vicinity of the piezoelectric wafer can increase as the applied force increases.

In 1997 Seeman et al.[87] modeled the effect of stresses in a simply supported beam actuated by piezoelectric actuators which were bonded to the top and bottom surfaces. The results of their finite element simulation showed that stresses in the beam were highest at the beams resonant frequency.

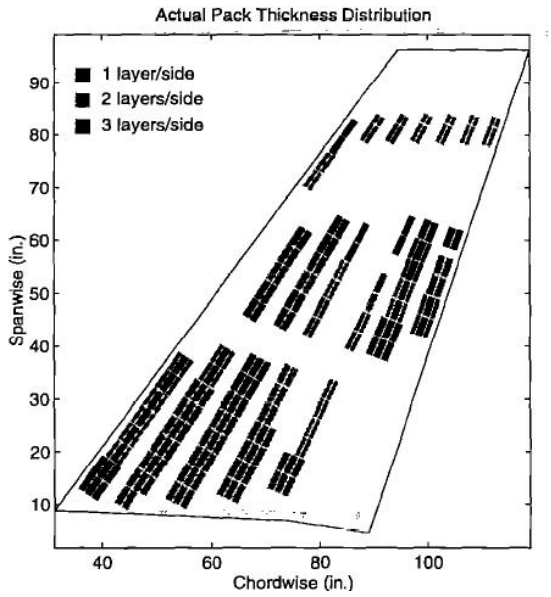

Figure 4: Actuator distribution of the Buffet Load Alleviation system (BLA)

In 2002 Luo and Tang[59] modeled a PZT patch bonded at the root of a cantilever beam. The PZT patch was 0.001m thick and 0.01m in length. They found that shear and peel stresses were maximum at the PZT patch edge.

1.3.2.3 Flow control

In 2000, Kandil[46] used computer models to investigate the effectiveness of adaptive flow control for twin-tall buffet alleviation. This method used control ports at locations on the vertical tail surface. The idea was to use positive or negative flow control to reduce the pressure differential across the tail surface, thus reducing the vibration of the tail. To model the open loop each time step began by solving the fluid flow problem while keeping the twin tail rigid. The Navier-Stokes equations were solved using an implicit, flux-difference splitting finite-volume scheme. The initial flow field conditions along with the pressure difference across the thickness of the tails were determined. The pressure difference was used to generate the normal forces and twisting moments per unit length of the tail. Next, the equations were solved sequentially to obtain the bending and torsion deformation of each tail. The grid displacement equations were then used to compute the new grid coordinates. For the closed loop control the adaptive flow control was applied starting with the initial flow

field conditions, which were obtained with the twin tail kept rigid. Suction or blowing was determined by the derived volume flow rate as proportional to the instantaneous pressure difference across the tail at the location of sensing pressure port. Results showed that the first bending mode PSD was reduced by approximately 50% at the tip and the torsion mode was reduced by 75%.

In 2001, Flynn[22] showed that a permeable surface, passing air through a plenum, reduced the amplitude of the buffet excitation. In 2001, Sheta[90] used additional blowing techniques such as tangential central blowing (TCB), tangential vortex blowing (TVB), and tangential span wise blowing (TSB) to inject high-momentum fluid into the vortical flow of generic fighter aircraft flying at 30 degrees angle of attack. These techniques strengthened the vortex that delayed the breakdown of the flow. In the developed simulation, the amplitude of the first bending mode was reduced by 43%. Though large other techniques discussed earlier [16, 46] have produced much larger reductions in the buffet induced vibrations.

In that same year El-Badawy and Neyfeh[18, 19] used saturation based control and piezoceramic patches mounted near the root of the tail as vibration absorbers to reduce steady state vertical tail vibrations on a 1/16th scale model of an F-15. Sensors were in the form of strain gages. The frequency suppressed was at primary resonance. Experiments were conducted using MATLAB/SIMULINK, positive position feedback control, and DSpace DSP, which verified these results. The actuators used were two piezoelectric patches made from lead-zirconate-titanate (PZT). A whole order of magnitude reduction in vibration amplitude was achieved.

In that same year (2001), Burnham et al.[10] developed finite element models of an F/A-18 vertical tail which used active rudder and piezoelectric actuators in tandem. Using a more advanced version of the Buffet Load Alleviation (BLA) system produced 30% to 70% vertical tail buffet response reductions for flight conditions ranging from moderate to severe buffet. This was accomplished with a maximum commanded rudder position of ± 2 degrees (15 Hz) and about 10 lbs of piezoelectric actuators attached to the vertical tail skin and operated at a peak power level of 2000 watts.

Also in 2001, Appa et al.[3] modeled a smart rudder system in which piezoelectric actuators were installed in the rudder at the hinge line. This system was called the Active Control Surface Modal (ACSM) device that generated unsteady aerodynamic damping to alleviate more effectively the aeroelastic structural instability, vibration and dynamic loads. An active control surface modal deformation was created by pairs of antagonistically activated actuators. The light-weight upper and lower surface skins were activated at high frequencies that encompassed the wide band spectrum of buffet, gust and self excited flutter phenomena. Although, the ACSM was an integral part of the rudder, independent control laws were employed to serve the buffet load and the flight control requirements. Thus, the ACSM device generated unsteady aerodynamic damping out-of-phase with the external (buffet/gust) or self-excited air loads (flutter) to reduce or eliminate the undesirable dynamic effects on the aircraft. Results showed 60 to 80 percent reduction in peak stress.

In that same year, Sheta[94] numerically investigated PZT wafer actuators installed on the inboard and outboard surfaces of the vertical tail of an F/A-18 to control the buffet responses in the first bending and torsion modes (Figure 5). A single-input-single-output (SISO) controller was designed to drive the active piezoelectric actuators. Measured acceleration was entered into two control laws $(CLaw)_{tip}$ and $(CLaw)_{root}$ which control the tip and root PZT patches, respectively. Each of the control laws had different control law gains. These gains were used to set the peak magnitude of the control law to unity. A switch was used to close or open the control loop of either the tip or the root control law. The output signals of the controllers were I_{tip} and I_{root} which was sent into voltage amplifiers with gains of K_{tip} and K_{root}. The voltage signal was then applied to drive the PZT actuators causing strain actuation. A multidisciplinary analysis was performed by taking into account the fluid dynamics, structure dynamics, electrodynamics of the piezoelectric actuators, fluid-structure interfacing, and the grid motion, which were integrated into a multidisciplinary computing environment that controls the temporal synchronization of the analysis. The PSD magnitude of the tip acceleration in the first torsion mode was reduced by about 69%. The RMS value of tip acceleration was reduced by about 10%. The PSD magnitude of the tip acceleration in the first bending mode was also reduced by about 22%.

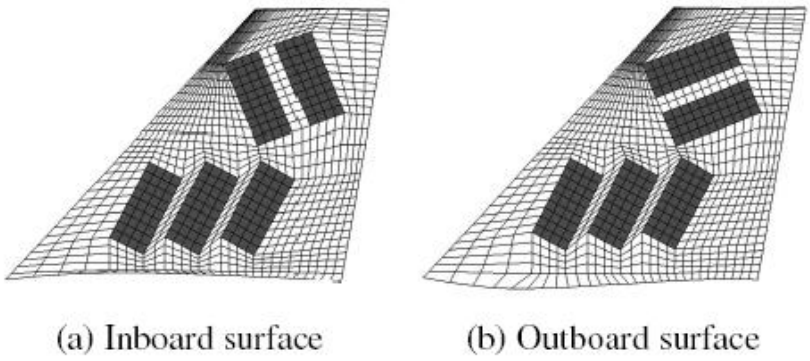

Figure 5: Aeroservoelastic model of the FA-18 vertical tail[94]

In 2004, Ferman[20] performed subsonic wind-tunnel tests of a 4.7%-scale model of the F-15 fighter. Tangential blowing was introduced from three points: the nose, the wing-root leading edge, and the gun bump, flowing back to the tails. Several blowing pressure values were used at angles of attack from 0 degrees to 32 degrees. Results showed that blowing was seen to lower the buffet pressures only by a few percent. The amount of buffet induced vibration reduction using his method does not come close the previous efforts by Hanagud and Kandil[16, 46]. The level of response varied somewhat between bending and torsion moments and acceleration data. Also, the trends depended upon the angle of attack, yaw, and frequency bands. In some cases, blowing actually increased the dynamics of the vertical tail response slightly. The most effective blowing position was the wing blowing position followed by the gun position and then the nose position (which was the least effective).

In summary, the largest reduction of buffet induced vibration was by Bayon de Noyer and Hanagud. They have shown an 80% reduction (in four months) in a wind tunnel at high angles of attack, using offset piezoceramic stack actuators, accelerometer sensors, and acceleration feedback control.

1.4 Neural networks in active damping of structures

In 1993, Drakunov et al.[17] used a neural network along with a sliding mode controller to track the output of a simulated Euler-Bernoulli beam with piezoelectric strips along one

of its sides. The neural network was used to learn and perform integral transformations of the distributed parameter system. In the simulation, the first two modes of the beam were excited. Results show that when the neural network was used it was able to track the output of the beam.

In 1995, Long et al.[57] developed simulation models of neural network controllers for vibration suppression using sensors and actuators that were non-collocated. Actuators and sensors were non-collocated for a variety of reasons such as when the optimum control location was different from the optimum point of control observability, damage to the structure may not allow collocated sensor/actuators, and other physical constraints. PZT elements were designed as sensors to measure angular displacement and angular velocity. Long controlled a cantilever beam using what was called a forward dynamics controller. The control procedure worked as follows: the state at time k was fed to the neurocontroller which generated a list of trial controls spanning the range of admissible control. These controls together with the state (at time k) were fed to the forward dynamics neural net. A trial response for each trial control was produced and the corresponding cost (J) was computed. The control corresponding to the smallest J was selected, which produced a new plant response at time *k+1*. For each time step this procedure was repeated. During an on-line learning interval, the plant output was compared to the estimated plant output from the forward dynamics neural net model. The error was used in back propagation to update weights of the neural network. Using an impulse excitation the open loop tip displacement of the experimental cantilever beam was 0.25 in. When the controller was turned on the displacement was reduced to zero in 1.5 seconds. When a 1 Hz sine wave was used as the excitation, the cantilever beam tip displacement was 2 in. When the controller was turned on the displacement was reduced to one inch.

In predictive control, the plant model was used to predict future behavior of the plant which was then used for future control performance[30]. In 1996, Pado and Damle[76] used a cantilevered beam and a neural network with predictive control to run at much higher bandwidths. The system consisted of a 28-inch aluminum beam with an accelerometer at the free end and a PZT actuator close at the root. The first two modes of the beam were

at 5 and 31 Hz. For this neural predictive control, the neural network shown in Figure 6 was used.

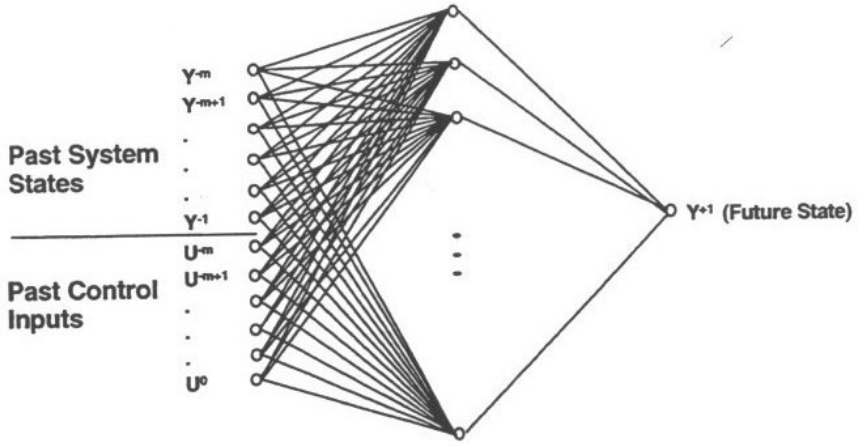

Figure 6: A Neural Network plant model for predictive control[76]

The neural network used in this effort was called the Multi-Layer Perceptron (MLP) and was the active element in the Neural Predictive Control (NPC). It used backpropagation to train the network. This type of network was called a universal approximator and was able to learn a function to a specified degree of accuracy. This network was very compact. It was also able to model nonlinear systems. The drawback of this type of neural network was that it takes longer to train than other types of neural networks. The beam was driven with a random excitation from 0 - 185Hz. The response was fed into the Neural Network and passed through a digital tapped-delay-line for m past time steps. Both the current and past control inputs were also fed into the network in the same manner. As in typical backpropagation the output from the neural network was compared with the actual sensor output and the difference between the two was used to adjust the weights of the neural network. Once the network was trained, the current state information was fed into the neural network as well as the first proposed control input. Referring to Figure 7, the Multi-Step Horizon Look Ahead took this input and projected n steps into the future.

In equation (1) the value of n was determined by the modes of the plant and the control rate. The value of n was between 1 and 20 and was called the horizon. This horizon was then passed to the Performance Index that was a cost function. It was comprised of

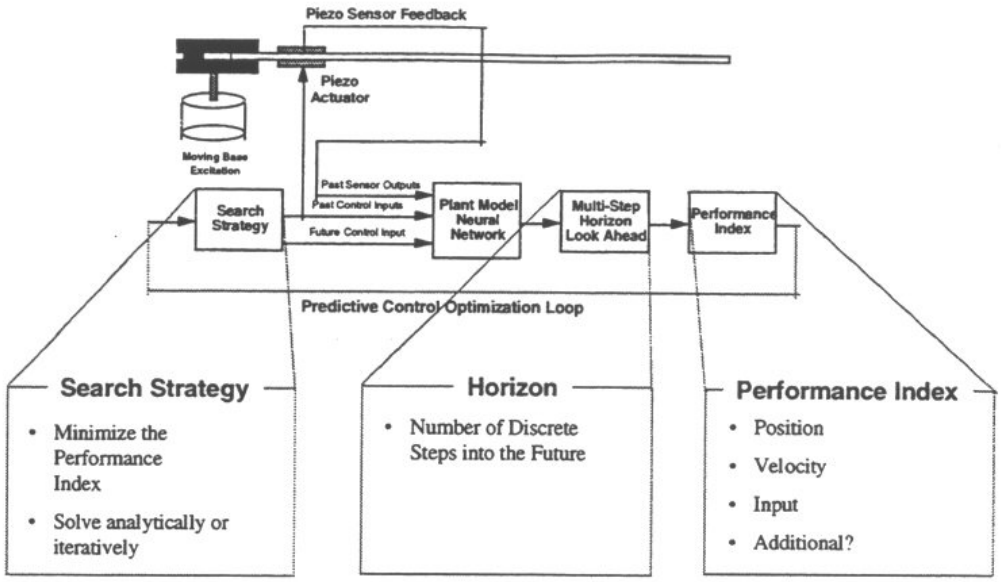

Figure 7: Predictive Neural Network implementation on a cantilevered beam[76]

future predictions of the neural network model (position), its derivatives (velocity), and the proposed control (input). Each of these parameters were weighted and tailored to a particular system using the following equation.

$$C = \sum_{i=1}^{n} (G_p Y_i^2 + G_v \dot{Y}_i^2 + G_I I^2) W^i \tag{1}$$

where

C was the cost of the selected input (I)

i was the horizon index

n was the horizon window

G_p was the position gain

Y_i was the predicted state of the plant at horizon i

G_v was the velocity gain

G_I was the input gain

W^i was the future state weighting factor

Once the value of C was determined, it was passed to the search strategy. Before testing began it took 5 minutes to train the neural network and another five minutes to tune the cost function. In test results, the neural network results were similar to a pole placement controller which was 36dB when controlling a linear plant.

In that same year, Lu et al.[58] used a neural network to control vibrations on a simulation of a simply supported beam with structural nonlinearities, modeling error, parameter imprecision, and disturbance. Specifically, they developed a neural algorithm to design the structural vibration control system and a neural network controller. The location of the actuator was at x = 1/6L and the sensor was at 5/6L. The control had a two-step process: (1) Learn the dynamic characteristics of the structure (2) Control the system to obtain results as good as an LQR control system. Results showed that this controller could eliminate the vibrations within seven seconds.

Also in 1996, Wang and Sinha[104] addressed the issue of controlling uncertainties in a single degree of freedom system by the development of a hybrid controller. The sources of these uncertainties were changes in system parameters and excitation frequencies. In a numerical model this hybrid controller was composed of a classical discrete-time LQR and two feed forward multi-layer neural networks known as Multilayer Neural Network A (MNNA) and Multilayer Neural Network B (MNNB). The neural networks controlled the uncertainties in the system. The uncertainties were in the form of system parameters such as stiffness and damping and excitation frequencies. MNNA compensated for modeling errors in the output of the model. MNNB corrected the control input for the vibration response. A spring-mass system was subjected to a sinusoidal excitation to test this controller. Different values of stiffness and damping were introduced into the model with an approximately 50% reduction in the amplitude of the displacement for steady state vibrations. Both neural networks were trained prior to testing.

In 1998, Spencer et al.[98] used an adaptive neural network to control vibrations on a cantilever beam. A numerical model and an experiment to control vibrations in a cantilever beam were created. The beam dimensions were 20 x 1 x 1/16 inches. The actuators used in

the experiment were PZT-5H (2 x 1 x 0.01 inches) from Morgan Matroc. These actuators applied control moments at specific points along the beam. A set of PZT actuators were bonded at the root of the cantilever beam to provide excitation force. These excitation forces were in the form of periodic external disturbances. This was modeled numerically and tested experimentally. In the numerical model, the beam rotated at each point where an actuator was placed. The actuators were modeled as torsional springs and the external disturbances were torques applied at these joints. The controller had three parts; (1) an underlying proportional-derivative component, (2) an adaptive component, and (3) a neural network. The measured tip acceleration in the open loop was 0.5 g. In the closed loop the reduction in acceleration amplitude was approximately 90%.

In 2001, Jha and He[44] developed an adaptive controller called the Direct Adaptive Neural Network Controller (DANNC) to reduce vibrations in an experimental cantilever beam. An adaptive neural network did learn while it controlled so there was no pre-training. This type of neural network was required for applications where changes in the system or environment, including uncertainties, occurred and the controller was required to adapt to these conditions while controlling the plant. Training used the Levernberg-Marquardt backpropagation algorithm. Two ACX PZT actuators were bonded to the beam at the root. Acceleration was measured at the free end of the beam. The goal of the controller was to control the first mode subjected to impulse, and band-limited white noise disturbances. The first two modes of the beam occurred at 6.2 Hz and 37 Hz. For the first mode impulse excitation, the settling time was reduced over 80%. For the sine wave, the controller learning was completed in four cycles (about 0.5 seconds) and RMS of the vibration amplitude was reduced by 90%. However, during training the closed loop response was somewhat larger than the open loop. Even though the goal was to control the first mode, the controller was able to control the second mode with RMS reduction of 86%. During a white noise disturbance (0-50 Hz) the RMS was reduced by about 50%.

In that same year, Sharma and Calise[88] derived a method to augment existing state feedback linear controllers with an adaptive neural network. The benefit of augmenting with a neural network was to preserve the current controller architecture. This method

added the neural network signal to the linear controller signal to control uncertainties in the plant. This network was numerically modeled where the excitation was a square wave and an unstable plant. The control objective was to track the response and keep the plant stable. With the adaptive neural network it showed a 2.5% error in position tracking. Some of the restrictions of this controller were that it required full state feedback and that it attempted to match the closed loop plant to the response model state for state. Any uncertainties satisfied the matching condition where the neural network tried to enforce the same relationships between the plant states and their derivatives as those in the response model.

In 2003, Yang et al.[107, 105] experimentally validated this work by successfully controlling a 3-disk torsional pendulum and an inverted pendulum using this adaptive neural network (Figure 8). Only the bottom disk(θ_3) was actuated by a brushless DC servo motor.

Figure 8: The 3-disk Torsional Pendulum System

Two experiment cases where successfully demonstrated (1) collocated sensor and actuator and (2) non-collocated sensor and actuator.

1.5 Neural networks in the control of buffet induced vibrations

One of the first uses of neural networks in the control of buffet induced vibrations was to characterize the buffet-induced pressures on the aircraft vertical tail. These buffet pressures were from a highly nonlinear relationship between upstream geometric and aerodynamic parameters. In 1993, Pado and Jacobs[73] needed to predict the location, magnitude, and frequency content under any flight condition from these buffet pressures. Even though there were many important advances in the field of computational fluid dynamics researchers were not capable at that time of predicting the separated flow dynamic pressure environment around the vertical tail. However, neural networks at that time could only focus on overall parameters such as error. So, a new neural network had to be developed. These two researchers developed a new hybrid cascading neural network (HCNN) which had the ability to both extrapolate as well as to perform the dynamic scaling necessary to retain shape features of the pressure frequency spectra. This was accomplished while using noisy data.

Data was acquired from the work on vortex tail interactions by the NASA Langley Research Center and was used to train the HCNN. Pado and Jacobs used a rigid tail of a 76-degree delta wing model with five Kulite pressure sensors on the vertical tail. This tail was adjustable along the longitudinal axis. Many neural network architectures were considered such as Radial Basis Function Network, General Regression Neural Network, and Multi Layer Perceptron trained with backpropagation. Only the Radial Basis Function Network coupled with a multiquadratic function was capable of accomplishing the distance interpolation, which led to the required extrapolation, thus the hybrid label. Stresses were modeled using FEM as the aerodynamic pressure was greatest at the leading edge of the tail and decreased towards the trailing edge. For frequency dependent data a forty nine output architecture was used to construct the power spectral density in the frequency range of interest. A single neural network was not capable of handling the variation in PSD as a function of angle of attack, especially at low and high magnitudes, so a scaling or cascading method was derived. The predicted RMS pressure was input to the multilayer perceptron, which were used to predict the basic shape of the PSD. This performed a dynamic scaling. Overall RMS error magnitude was within 5% of the experimental PSD values in the range

of interest. In 1994, Jacobs et al.[43] extended the model to include a twin flexible tail. The two tails were capable of being adjusted laterally so that the tails were tested inside and outside the vortex flow. This allowed further HCNN training for future tail designs when considering tail buffet.

In a related field, one of the early attempts of the active control of an aeroelastic wing structure was in 1995[86] in a joint NASA/Boeing effort, as part of the Adaptive Neural Control of Aeroelastic Response (ANCAR) project, using transonic wind tunnel data to train a neural network for flutter suppression. The goal of this program was to develop a neural network based adaptive control scheme using what was called the Benchmark Active Controls Technology (BACT) wind tunnel model. The wind tunnel used was the Transonic Dynamics Tunnel (TDT) at NASA Langley. The tunnel was a single return, variable density transonic wind tunnel. The test section measured 16 ft by 16 ft. The BACT wind tunnel model was a rectangular wing with a NACA 0012 airfoil cross section. Trailing edge control surfaces and spoilers were independently controlled. The adaptive neural network was used to schedule 56 flutter suppression control laws with fixed gains. Each law used a corresponding state space model. The state space models in this design used the same structural and aerodynamic models with varying Mach number and dynamic pressure. The range of Mach numbers was 0.3 to 0.9 and the range of dynamic pressure was 75 to 250 psf. These state space models were used to design a fixed gain control law, which were optimized to minimize accelerometer output for each combination of Mach number and dynamic pressure. A fixed gain feedback control law was designed to stabilize and minimize the response over all the state space models. Root locus and zero placement was used in the design of the feedback control law. The neural network was trained using backpropagation. The examples used to train the neural network were in the continuous domain rather than in the discrete domain because the continuous domain coefficients vary smoothly as a function of Mach number and dynamic pressure and do not require high numerical precision. Experimental results clearly showed that the trailing edge RMS acceleration was lower with the neural network than with the fixed gain controller by approximately 10%.

In 1996, Lichtenwainer et al.[55, 56] used Neural Predictive Control (NPC), as part

of the Adaptive Neural Control of Aeroelastic Response (ANCAR) program, to control flutter on the BACT wing model in the Transonic Dynamics Tunnel (TDT) at the NASA Langley Research Center. On the wing, the trailing edge flap was used as the actuator and accelerometers were placed next to the flap and acted as sensors. The NPC was used in a SISO control scheme whose control laws were a function of Mach number (M) and dynamic pressure (q). Phase I of this work used both a fixed gain controller and Model Predictive Control (MPC) neural network for semi-adaptive control to tailor poles and zeros at each M and q. More specifically, a set of fifty six combinations of M and q were created and used to train the network. Results showed that the neural network reduced the RMS slightly more than the fixed gain. Phase II implemented a fully adaptive flutter suppression system using the MPC architecture (See Figure 9).

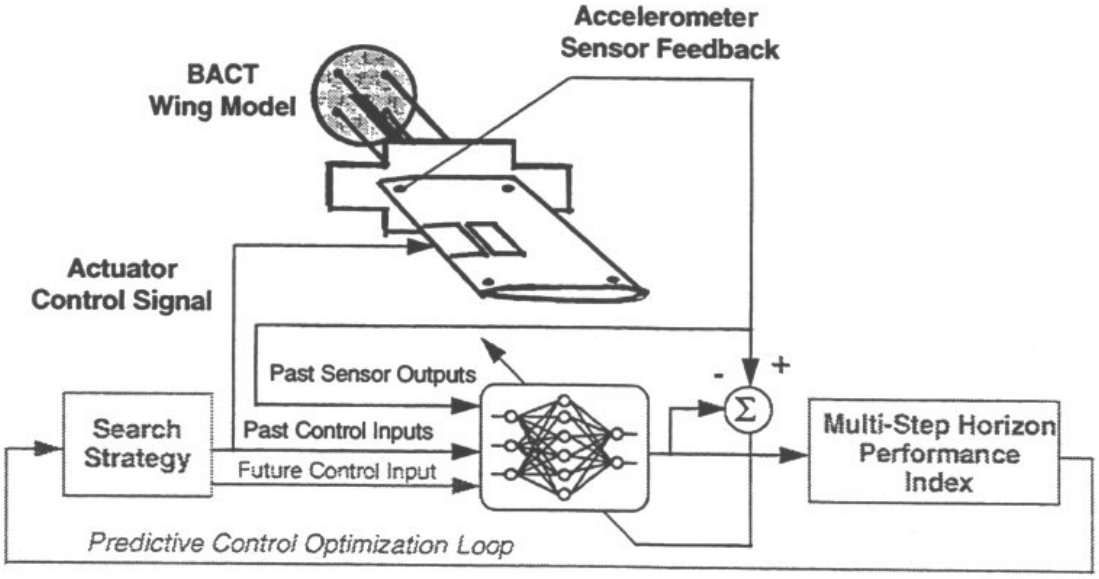

Figure 9: Neural Predictive Control System Architecture on BACT wing PhaseII[55]

This phase II neural network was trained before use and updated on-line to cope with changing flight conditions and plant dynamics. In these tests, the SISO control was demonstrated up to 500 Hz. There were several steps to this process. First, the control started with an untrained network. Initial training took place by using white noise to excite the plant and measuring the response of the plant in the open loop. The sequence of white

noise sent to the aileron was for four seconds, then a 2.7 second learning interval, followed by a 6.7 second control interval. After this, learning and control occurred simultaneously, updates to the neural network were allowed every 6.7 seconds. This control scheme had the capability to update itself depending on the CPU speed, control cycle rate, and the amount of data required for accurate plant modeling. This type of control showed an improvement over the semi-adaptive controller, however, the search and learning times did take some time depending on the complexity of the control scheme and the plant model.

In 1998 and 1999, Pado and Lichtenwalner[75, 74] were the first to use a neural network to actively control tail buffet. This research was from a joint Boeing, St. Louis/NASA Langley Research Center effort to reduce the tail buffet effect that reduces the fatigue life of many aircraft. Neural networks were chosen as the solution due to their ability to model the plants nonlinearities and their adaptability. A Neural Predictive Control (NPC) neural network was created as shown in Figure 10. A wind tunnel test was setup at the NASA Langley Transonic Dynamics Tunnel (TDT) using a 1/16th scale model aircraft of a YF-17 (later known as the F/A-18). The model was configured with a scaled flexible vertical tail, mounted on the port side of the model. The control mechanism on the starboard tail was an active rudder to control the first mode (bending) and a PZT patch to control the second mode (torsion). The port tail had two PZT patches as actuators to control bending and torsional vibrations. The flexible tails used an aluminum spar and balsa wood cross sections. A hydraulic actuator was incorporated into the tail to move the rudder during the controlled runs. The strain gages were used as sensors to control bending and accelerometers were used as sensors to control torsion.

Because the magnitude of buffet was a function of dynamic pressure and angle of attack, RMS pressure was experimentally determined at six different angles of attack (AOA) between 20 and 40 degrees and at dynamic pressures of 3.5, 5.2, 7.8, and 10.0 psf. Researchers assumed that over 80% of the tail damage occurred in these regimes. There were two modes of interest in the test; first bending at 18 Hz and first torsion at 58 Hz. Control authority was a measure of how effective the control was for targeted control states. In this case, control authority was measured by using a Rotational Variable Displacement Transducer

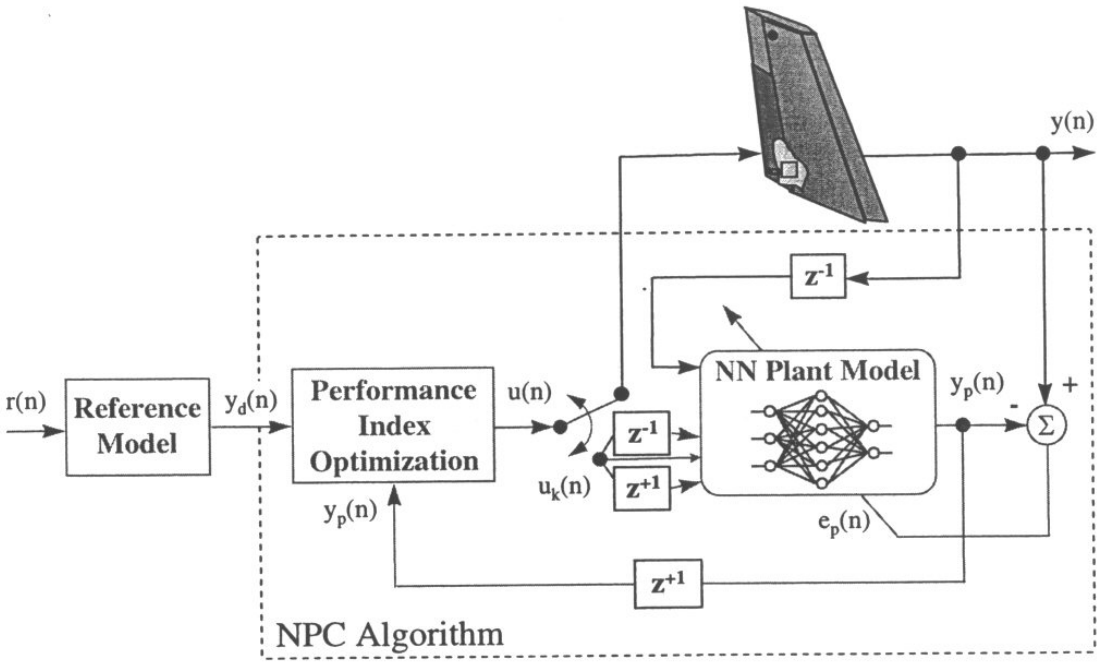

Figure 10: Neural Predictive Control Buffet Load Alleviation System[75]

(RVDT).

For training purposes prior to implementation, the neural network plant model was used with rudder to strain gage transfer functions. They started with seven degrees AOA and performed random excitation tests from 0 to 200 Hz. The output from the network was compared to the actual sensor output and the weights of the neural network plant model were adjusted using backpropagation. The SISO system was trained using the same method as mentioned with the BACT wing except for the MIMO system. They tried two different techniques. The first technique used a single integrated network. Past actuator control inputs from each of the actuators and past states from the sensors were fed into a single neural network. The second technique used multiple, independent SISO controllers. These were separately trained but used simultaneously. In these tests the highest buffet loading occurred at 34 degrees angle of attack. Using the NPC controller and the rudder, the first bending mode reduction in RMS was 20%. First torsion mode reduction was 12%. The MIMO solution had somewhat better results. First bending was reduced by 30% and 10% in first torsion. The starboard tail had less reduction in RMS. This showed that using a

control surface for tail buffet alleviation was not as effective as using an actuator separately for this purpose. These reductions are not as much as those demonstrated by Bayon de Noyer and Hanagud[31] without neural networks.

Chapter II

MOTIVATION FOR THESIS

2.1 Problem

Problem 1: During high-angle-of-attack maneuvers of the F/A-18 aircraft, there is an unsteady flow over the vertical tails. Unsteady flow is the result of a breakdown of vortices produced at the leading edge and intersection of the wing and fuselage. In addition,unsteady flow causes buffet-induced vibrations of the vertical tails. This leads to early and premature fatigue cracks in the vertical tail structure of the F/A-18. Many different solutions are proposed to solve this problem but with very limited results. An exception is the offset piezoceramic stack actuators that are very effective (80% reduction of the RMS in four modes) in reducing vibrations in the wind tunnel tests of a 1/16th scale F-15 model vertical tail and a full-scale lab setup. However, there is no systematic procedure to design and optimize the OPSA system.

Problem 2: Currently, linear controllers are designed and implemented to show the feasibility of reducing buffet induced vibrations in the vertical tail of twin tailed aircraft. However, unmodeled dynamics due to the fuselage and wings and nonlinear vibrations due to debonding of the skin, caused by moisture, cannot be accommodated by linear controllers. Thus, it is necessary to adaptively compensate the linear controller under these conditions.

Problem 3: In most structures, fatigue critical areas are associated with regions of high stresses. Passive stiffening of structures usually displaces these high stress regions to other regions of the structure. Thus, for most applications, active vibration control is preferred. However, the question of whether an active vibration control scheme involving a set of bonded actuators will reduce stresses in the whole structure or create new high stress areas near the actuators need answers.

2.2 Objectives

Based on the discussion in Chapter 1 and the discussions in section 2.1, the following are the objectives of the proposed research program:

Objective 1: Develop procedures to design and optimize the offset piezoceramic actuators assemblies controllers and sensors to reduce buffet induced vibration. The design includes the selection of piezoceramic stacks, the detailed design of the actuator assembly, the number of such actuators, the actuator locations and the orientations to meet the design objectives.

Objective 2: Develop procedures to design adaptive neural network controllers to augment the linear controller and control the tail buffet-induced vibrations. The adaptive neural network control should accommodate the unmodeled dynamics and any nonlinear vibrations due to the delaminations or debonding in the vertical tail structure.

Objective 3: The third objective of this work is to analyze the stress distribution changes that are caused by the use of OPSAs during their use as active vibration control actuators.

2.3 Justification

Buffet induced vibrations reduce the fatigue life of vertical tails in high performance aircraft. A solution must be found that can retrofit current aircraft in operation. As available actuator location and available power for active control in an aircraft are very limited, any additional control system needs to be small and use very little power. The offset piezoceramic stack actuator meets these requirements.

In previous work (see Chapter 1), it has been shown that the OPSA along with acceleration feedback control can reduce vibrations in several modes of an F-15 vertical tail. It has also been shown that an adaptive neural network can be designed to augment a linear controller. If an adaptive neural network could be used to augment a linear acceleration feedback controller then the adaptive control system can significantly increase the fatigue life of the vertical tail.

Bonded actuators like the OPSA, show a lot of promise in reducing vibrations. These actuators have the potential to reduce high stresses, thus, extending the fatigue life of the

structure. These are low cost actuators and could save many times their value by reducing the number of fatigue cracks and the associated vehicle maintenance cost.

2.4 Outline

In Chapter 3, a procedure has been developed to design and optimize the OPSA for needed control authority. This has been applied to the design of actuators to control buffet induced vibrations in F-15 and F-18 aircraft.

In Chapter 4, a control scheme has been designed and developed to use an adaptive neural network, to augment a linear controller, which controls vibrations in a F/A-18 vertical tail as structural parameters shift from the design state. The structural parameter shifts occur due to increase in air speed and disbonds. Both numerical simulation and experiments show the effectiveness of this control scheme are discussed.

In Chapter 5, stresses in a beam and a plate structure with active vibration control OPSA are studied. This study shows that bonded OPSA's can reduce stresses including the local to the area around the actuator of the same order of magnitude as the controlled vibrations.

In Chapter 6, conclusions of this work are summarized and recommendations for future work are discussed.

Chapter III

FATIGUE LIFE ENHANCEMENT OF F-15 AND F-18 VERTICAL TAILS USING PIEZOCERAMIC STACK ACTUATORS AND VIBRATION CONTROL

In this chapter, a systematic procedure is developed to design the offset piezoceramic stack actuator (OPSA) parameters and the selected controller parameters including placement of sensors and actuators. The objective of the design is to deliver the needed control authority to dampen the specified buffet-induced vertical tail vibrations, during high angle of attack maneuvers, to a specified level that will improve the fatigue life. This includes designing the actuator assembly parameters of OPSA, selecting stacks from available commercial piezoceramic stacks, and the number of the needed piezoceramic stacks to achieve a specified performance under the specified worst buffet scenario. The design procedure starts with a structural dynamic model for the closed loop system.

3.1 Structural Dynamic Model

In this study, the closed loop system consists of an F/A-18 vertical tail structural dynamic model with attached OPSA assemblies, and selected controllers. This can be generalized to any high performance aircraft. The selected controller is the acceleration feedback controller (AFC). It is possible to develop a detailed finite element model for such a closed loop system. However, to parametrically understand the actuations of the OPSA, understand the effects of the actuator assembly parameters and the controller parameters, including the number of stacks, a simplified analytical model is preferred. Specifically, the tail structure is modeled with coupled bending and torsional motions. The dynamics of the fin structural assembly with OPSA is then described by partial differential equations. In this study, the acceleration feedback control system is described by ordinary differential equations coupled to the structural dynamic differential equations.

3.1.1 Acceleration Feedback Controllers

In previous investigations of the control of tail buffet induced vibrations, many different types of controllers such as neural predictive controller[74], LQG[50, 62, 97, 68, 69], PID[35], frequency domain compensation[64], and direct feedback[4] are used. Each controller has some advantages and some drawbacks. The selected AFC controller has a relative degree of two between the denominator and the numerator of the controller transfer function (See eqn (37)). Thus, the magnitude of the transfer function decreases rapidly (fast roll-off rate) as the frequency increases. The fast roll-off avoids any interaction with unmodeled higher order modes in the plant-model. The phase angle is beneficial for designing the system with non-collocated sensors and actuators. Using acceleration feedback, a second order compensator was first developed[29, 45, 95] with unconditional stability for single degree of freedom systems with collocated pairs of sensors and actuators. In the published work of Bayon de Noyer and Hanagud[32, 15] acceleration feedback control was used for non-collocated actuators and sensors.

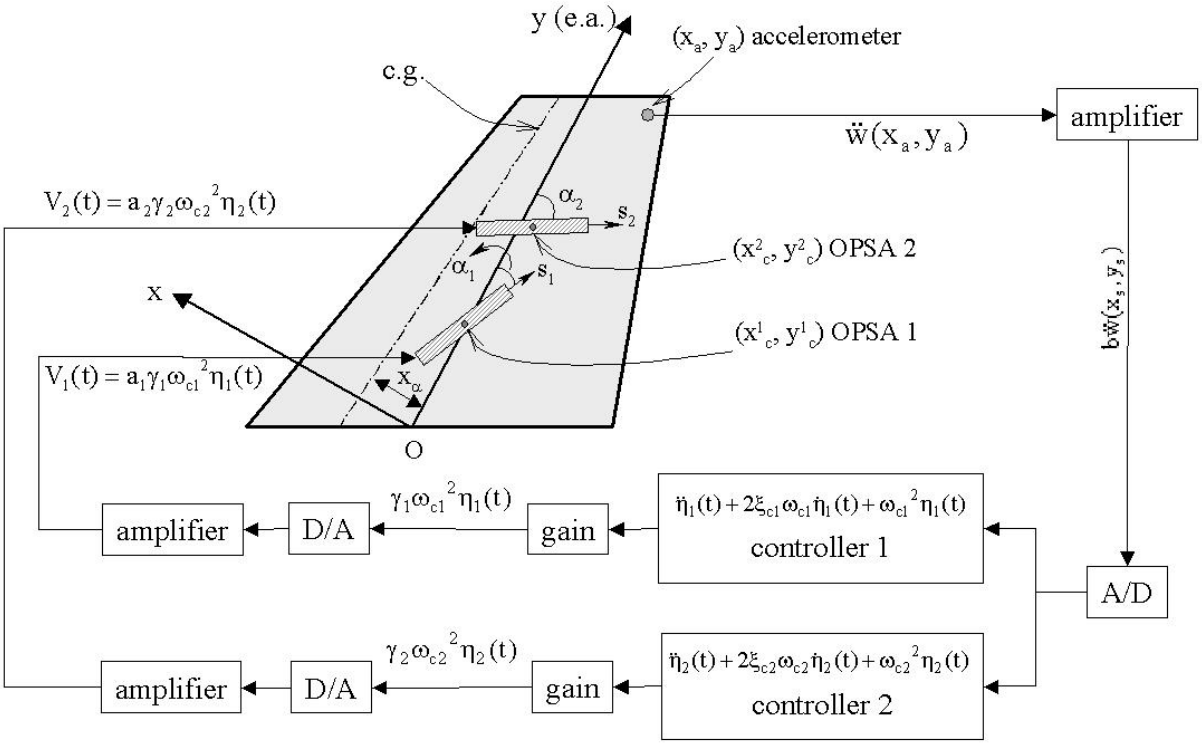

Figure 11: The diagram of the F/A-18 active control system.

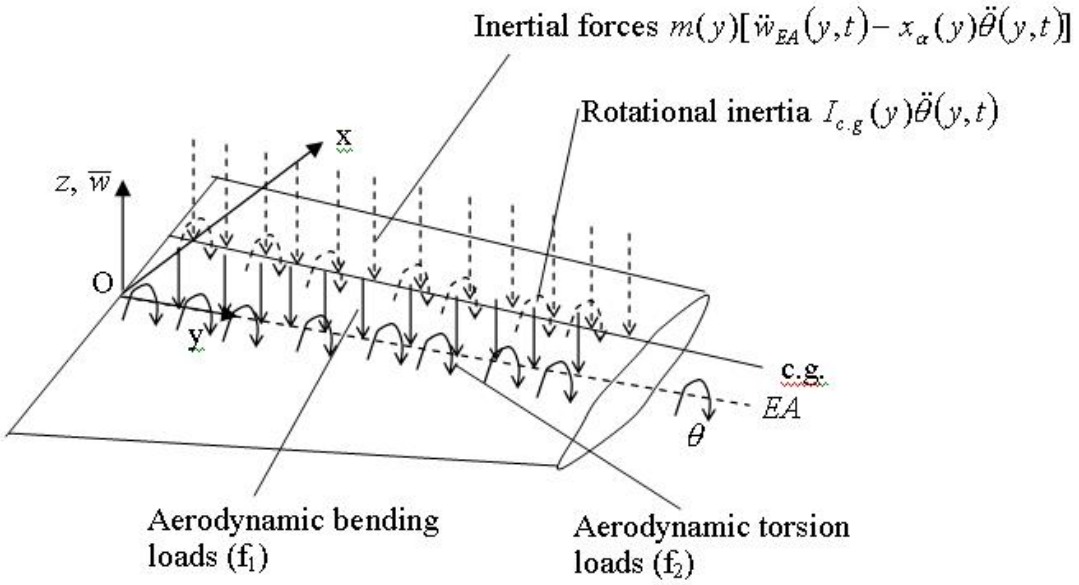

Figure 12: Free body diagram of aerodynamic and inertial loading on F/A-18 Vertical tail

3.1.2 Model for the Closed-Loop System

The elastic axis of the vertical tail structure is chosen as the y-axis (see Figures 11 and 12). One sensor (e.g. accelerometer), located at (x_a, y_a), provides the input (i.e. the structural response of the tail) to controllers. The outputs of controllers are multiplied by gains γ_i and are applied to the stacks in OPSAs. Two sets of OPSAs are mounted on the tail structure. Each set of OPSA includes several piezoceramic stacks, whose outputs are additive. As shown in Figure 11, the i^{th} OPSA is orientated at an angle α_i to the elastic axis of the tail. The center of OPSA i is located at (x_c^i, y_c^i). When subjected to an electric field the forces exerted by each piezoceramic stack on the structure are divided into two parts: two point moments (that are decomposed into bending and torsional moments) and a pair of extensional forces (Figure 3). Using the free body diagrams of Figures 3 and 12 and the OPSA locations as seen in Figure 11 the governing equations for this closed-loop system are given by equations (2) through (4).

$$m(y)\frac{\partial^2 w}{\partial t^2} - mx_\alpha(y)\frac{\partial^2 \theta}{\partial t^2} + \frac{\partial^2}{\partial y^2}(EI(y)\frac{\partial^2 w}{\partial y^2}) = -\sum_{i=1}^{n} n_s^i F_s^i h \cos\alpha_i \frac{d}{dy}[\delta(y-y_2^i) - \delta(y-y_1^i)] + f_1(y,t) \tag{2}$$

$$-I_\alpha\frac{\partial^2 \theta}{\partial t^2} + mx_\alpha(y)\frac{\partial^2 w}{\partial t^2} + \frac{\partial}{\partial y}(GJ(y)\frac{\partial \theta}{\partial y}) = -\sum_{i=1}^{n} n_s^i F_s^i h \cos\alpha_i \frac{d}{dy}[\delta(y-y_2^i) - \delta(y-y_1^i)] + f_1(y,t) \tag{3}$$

$$\ddot{\eta}_i(t) + 2\zeta_{ci}\omega_{ci}\dot{\eta}_i(t) + \omega_{ci}^2\eta_i(t) = b\ddot{\overline{w}}(x_a, y_a, t) \qquad i = 1, 2, ..., n \tag{4}$$

where

$$f_1(y,t) = \int_c \Delta p(x,y,t)dx; f_2(y,t) = \int_c x\Delta p(x,y,t)dx \tag{5}$$

$\delta(\cdot)$ is the Dirac Delta function. Generalized aerodynamic bending loads $f_1(y,t)$ and aerodynamic torsion loads $f_2(y,t)$ are given by equation (5). The force generated by the stack is given by

$$F_s(t) = -A_s Y_s^E d_{33} E_{field}(t) \tag{6}$$

where A_s is the cross sectional area of the piezoceramic stack, Y_s^E is the stack Youngs modulus, d_{33} is the piezoceramic transverse coefficient, and $E_{field}(t)$ is the electric field applied to the stack. Eqn (4) is a linear second order controller equation. The acceleration sensor input to this equation is multiplied by the sensor influence coefficient b to represent the true signal into the controller. Any effects that are induced by the axial forces on bending and torsional vibrations are assumed to be small. The study by Hanagud et al.[83] showed the induced frequency reductions are small due to these axial force effects. The displacement of the vertical tail at any position (x,y) of the tail, $\overline{w}$(x,y,t), is contributed from both bending and torsional motions[25].

$$\overline{w}(x,y,t) = w(y,t) + x\theta(y,t) \tag{7}$$

The input voltage of the OPSA, $V_i(t)$, is the product of the actuator flexibility influence parameter a_i, controller gain γ_i and control signal $\omega_{ci}^2\eta_i(t)$ (see Figure 11). That is,

$$V_i(t) = a_i \Gamma_i \omega_{ci}^2 \eta_i(t) \qquad\qquad i = 1, 2, ..., n \tag{8}$$

The following geometric relations are needed for further analysis.

$$x_1^i = x_c^i - \frac{L_s}{2} sin(\alpha_i); x_2^i = x_c^i + \frac{L_s}{2} sin(\alpha_i); y_1^i = y_c^i - \frac{L_s}{2} cos(\alpha_i); y_2^i = y_c^i + \frac{L_s}{2} cos(\alpha_i) \tag{9}$$

$$\frac{\partial \overline{w}}{\partial s_i} = \frac{\partial \overline{w}}{\partial x}\frac{\partial x}{\partial s_i} + \frac{\partial \overline{w}}{\partial y}\frac{\partial y}{\partial s_i} = \frac{\partial \overline{w}}{\partial x} sin(\alpha_i) + \frac{\partial \overline{w}}{\partial y} cos(\alpha_i) \qquad\qquad i = 1, 2, ..., n \tag{10}$$

It is assumed that

$$\overline{w}(x, y, t) = \sum_{j=1}^{N} g^j(x, y)\xi_j(t) \tag{11}$$

where $g^j(x, y)$ is the j^{th} coupled bending-torsion basis functions of the tail, which is obtained by following the Appendix A. From equation (149) of the Appendix A, it is shown that

$$w(y, t) = \sum_{i=1}^{N} g_w^i(y)\xi_i(t) = \{\boldsymbol{\alpha}(y)\}^T [\boldsymbol{\Phi}]\{\boldsymbol{\xi}\} \tag{12}$$

$$\theta(y, t) = \sum_{j=1}^{N} g_\theta^j(y)\xi_j(t) = \{\boldsymbol{\beta}(y)\}^T [\boldsymbol{\Theta}]\{\boldsymbol{\xi}\} \tag{13}$$

where $\{\boldsymbol{\xi}\} = \{\xi_1, ..., \xi_N\}^T \{\boldsymbol{\alpha}(y)\}$ and $\{\boldsymbol{\beta}(y)\}$ are characteristic vectors of selected bending and torsion modes respectively (see equations (135) in Appendix A). $[\boldsymbol{\Phi}]$ and $[\boldsymbol{\Theta}]$ are the eigenvectors listed as in equation (147).

The coupled bending-torsional vibrations of a cantilever beam are used as trial and test functions and mode shapes of the closed loop system are determined by Galerkins method.

Because the basis functions that satisfy the boundary conditions are known as the trial and test functions [See Appendix A], the Galerkin method is used to solve the closed loop system of equations. Equations (12) and (13) are substituted into (2) and (3). Multiplying equations (2) and (3) by $\{\boldsymbol{\alpha}(y)\}$ and $\{\boldsymbol{\beta}(y)\}$ respectively, integrating with respect to y from 0 to L, and using equation (146), this gives

$$[\boldsymbol{B}](\{\ddot{\boldsymbol{\xi}}\} + [2\boldsymbol{\zeta\omega}]\{\dot{\boldsymbol{\xi}}\} + [\boldsymbol{\omega}^2]\{\boldsymbol{\xi}\} = \{\boldsymbol{f}_{ctrl}\} + \{\boldsymbol{f}_{aero}\} \tag{14}$$

where

$$[B]_{M\times N} = \begin{bmatrix} [C_{11}]\,[\Phi] - [C_{12}]\,[\Theta] \\ [C_{22}]\,[\Theta] - [C_{21}]\,[\Phi] \end{bmatrix} = \begin{bmatrix} [A_{11}]\,[\Phi] \\ [A_{22}]\,[\Theta] \end{bmatrix} \left[\omega^2\right]^{-1} \tag{15}$$

$$\{\boldsymbol{f}_{ctrl}\}_{M\times 1} = \left\{ \begin{pmatrix} \sum_{i=1}^{n} n_s^i F_s^i h cos(\alpha_i) \boldsymbol{d}_w \\ \sum_{j=1}^{n} n_s^j F_s^j h cos(\alpha_j) \boldsymbol{d}_\theta \end{pmatrix} \right\} \tag{16}$$

$$\{\boldsymbol{f}_{aero}\}_{M\times 1} = \left\{ \begin{pmatrix} \int_0^L f_1(y,t)\boldsymbol{\alpha}(y)dy \\ \int_0^L f_2(y,t)\boldsymbol{\beta}(y)dy \end{pmatrix} \right\} \tag{17}$$

$$\{\boldsymbol{d}_w\}_{M_1\times 1} = \left\{ \frac{d\alpha_1}{dy}\Big|_{y=y_1^i}^{y=y_2^i}, \ldots, \frac{d\alpha_{M_1}}{dy}\Big|_{y=y_1^i}^{y=y_2^i} \right\}^T \tag{18}$$

$$\{\boldsymbol{d}_\theta\}_{M_2\times 1} = \left\{ \beta_1(y)\Big|_{y=y_1^j}^{y=y_2^j}, \cdots, \beta_{M_2}(y)\Big|_{y=y_1^j}^{y=y_2^j} \right\}^T \tag{19}$$

$$\{\eta\}_{n\times 1} = \{\eta_1, \cdots, \eta_n\}^T \tag{20}$$

$$[2\zeta_c\omega_c]_{n\times n} = diag(2\zeta_{c1}\omega_{c1}, \cdots, 2\zeta_{cn}\omega_{cn}) \tag{21}$$

$$[2\zeta\omega]_{n\times n} = diag(2\zeta_1\omega_1, \cdots, 2\zeta_n\omega_n) \tag{22}$$

$$[\omega_c^2]_{n\times n} = diag(\omega_{c1}^2, \cdots, \omega_{cn}^2) \tag{23}$$

$$\{\mathbf{1}\}_{n\times 1} = \{1, \cdots .1\}^T \tag{24}$$

Matrices $[\boldsymbol{C}_{11}]$, $[\boldsymbol{C}_{12}]$, $[\boldsymbol{C}_{21}]$, $[\boldsymbol{C}_{22}]$, and $[\boldsymbol{\omega}^2]$ are listed in Appendix A. Multiplying the both sides of equation (15) by $[\boldsymbol{D}]_{N\times M} = ([\boldsymbol{B}]^T[\boldsymbol{B}])^{-1}[\boldsymbol{B}]^T$, this gives

$$\{\ddot{\boldsymbol{\xi}}\} + [2\boldsymbol{\zeta\omega}]\{\dot{\boldsymbol{\xi}}\} + [\boldsymbol{\omega}^2]\{\boldsymbol{\xi}\} = [\boldsymbol{D}]\{\boldsymbol{f}_{aero}\} \tag{25}$$

In these equations, ξ and η are the modal coordinates of the first bending mode of the structure and of the compensator; respectively; ω, ω_c, ξ and ξ_c are the natural frequencies and the damping ratios of the structure and the compensator, respectively; and γ is the scalar gain applied to the feedback signal.

3.2 Control of the 1st Mode

From the previous studies of Moses[64] and Ashley[4] on suppression of F/A-18 buffet induced vibration, it has been inferred that controlling the 1^{st} bending and 1^{st} torsion mode will also reduce higher modes and thus greatly extend the fatigue life of the structure. The first bending mode is considered to demonstrate the design problem. The model is simplified to include only one degree of freedom, i.e. N=1 which corresponds to the first bending mode. The closed-loop system reduces to a two degrees of freedom AFC system.

$$\begin{aligned} &\ddot{\xi}_1 + 2\zeta_1\omega_1\dot{\xi}_1 + \overline{\omega}_1^2\xi_1 = -n_s^1\overline{a}\Gamma_1\omega_{c1}^2\eta_1 + \overline{f}_1(t) \\ &\ddot{\eta}_1 + 2\zeta_{c1}\omega_{c1}\dot{\eta}_1 + \omega_{c1}^2\eta_1 = \overline{b}\ddot{\xi}_1 \end{aligned} \tag{26}$$

where

$$\overline{\omega}_1^2 = \omega_1^2(1 + \Omega^{-1}n_s^1k_s^\epsilon h(cos\alpha_1\{\boldsymbol{\Phi}^1\}^T\{\boldsymbol{d}_w\} + sin\alpha_1\{\boldsymbol{\Theta}^1\}^T(\{\boldsymbol{d}_{x\theta}\} + \{\boldsymbol{d}_\theta\}))\hat{a}) \tag{27}$$

$$\overline{a} = \Omega^{-1}\omega_1^2k_s^Ea_1\hat{a} \tag{28}$$

$$\overline{f}_1(t) = \Omega^{-1}\omega_1^2\hat{f}_1(t) \tag{29}$$

$$\overline{b} = b\{\boldsymbol{\alpha}(y_a)\}^T\{\boldsymbol{\Phi}^1\} + x_a\{\boldsymbol{\beta}(y_a)\}^T\{\boldsymbol{\Theta}^1\} \tag{30}$$

For measured differential pressure

$$\hat{f}_1(t) = \int_0^L\int_c \Delta p(x,y,t)(\{\boldsymbol{\Phi}^1\}^T[A_{11}]\{\boldsymbol{\alpha}(y)\} + x\{\Theta^1\}^T[A_{22}]\{\boldsymbol{\beta}(y)\})dxdy \tag{31}$$

For measured acceleration at a point

$$\hat{f}_1(t) = \int_0^L\int_c \frac{m}{A}\frac{\partial^2\overline{w}(x,y,t)}{\partial t^2}\delta(x-x_a)\delta(y-y_a)(\{\boldsymbol{\Phi}^1\}^T[A_{11}]\{\boldsymbol{\alpha}(y)\}+x\{\Theta^1\}^T[A_{22}]\{\boldsymbol{\beta}(y)\})dxdy \tag{32}$$

$$\hat{a} = h(cos\alpha_1\{\boldsymbol{\Phi}^1\}^T[A_{11}]\{\boldsymbol{d}_w\} + sin\alpha_1\{\boldsymbol{\Theta}^1\}^T[A_{22}](\{\boldsymbol{d}_\theta\}) \tag{33}$$

$$\{\boldsymbol{d}_{x\theta}\} = \left\{x\frac{d\beta_1}{dy}\Big|_{(x_1^i,y_1^i)}^{(x_2^i,y_2^i)}, \cdots, x\frac{d\beta_{M_2}}{dy}\Big|_{(x_1^i,y_1^i)}^{(x_2^i,y_2^i)}\right\}^T \tag{34}$$

$$\Omega = \{\boldsymbol{\Phi}^1\}^T[A_{11}]^2\{\boldsymbol{\Phi}^1\} + \{\boldsymbol{\Theta}^1\}^T[A_{22}]^2\{\boldsymbol{\Theta}^1\} \tag{35}$$

From equation (27), the OPSA is represented by the second term. This shows that the OPSAs stiffen the tail structure as the values of the second term are always positive.

This stiffening causes the closed-loop system to have a slightly higher natural frequency $\overline{\omega}_1$ than that of corresponding open-loop system ω_1. The difference between these frequencies increases with the offset h, the axial stiffness of stacks, the number of stacks and the deflection curvature at OPSA location. It also depends on the aligning orientation of OPSA, α_1.

3.3 Single Degree of Freedom Transfer Function

The transfer function of the response and the excitation for the open-loop system is given by equation eqn.(36). The closed-loop transfer functions of the excitation and the response, the controller signal and the response, the controller signal and the excitation, respectively, are given by equations (37) through (39).

$$G_{\xi f}^{open}(s) = \frac{\Xi_1^{open}(s)}{\overline{F}_1(s)} = \frac{1}{(s^2 + 2\zeta_1\omega_1 s + \omega_1^2)} \tag{36}$$

$$G_{\xi f}^{closed}(s) = \frac{\Xi_1^{closed}(s)}{\overline{F}_1(s)} = \frac{(s^2 + 2\zeta_{c1}\omega_{c1}s + \omega_{c1}^2)}{(s^2 + 2\xi_1\omega_1 s + \omega_1^2)(s^2 + 2\zeta_{c1}\omega_{c1}s + \omega_{c1}^2) + \Gamma_1\omega_{c1}^2 n_s^1 \bar{a}\bar{b}s^2} \tag{37}$$

$$G_{\eta\xi}^{closed}(s) = \frac{I_1(s)}{\Xi_1^{closed}(s)} = \frac{\bar{b}s^2}{(s^2 + 2\zeta_{c1}\omega_{c1}s + \omega_{c1}^2)} \tag{38}$$

$$G_{\eta f}^{closed}(s) = \frac{I_1(s)}{\overline{F}_1(s)} = \frac{\bar{b}s^2}{(s^2 + 2\zeta_1\omega_1 s + \omega_1^2)(s^2 + 2\zeta_{c1}\omega_{c1}s + \omega_{c1}^2) + \Gamma_1\omega_{c1}^2 n_s^1 \bar{a}\bar{b}s^2} \tag{39}$$

The Laplace transform of each variable is represented by the corresponding capital letter. The transfer function between the control signal and the plant displacement is derived from eqn(26) as follows

$$G_{\xi\eta}^{closed}(s) = \frac{\Xi_1^{closed}(s)}{I_1(s)} = \frac{-n_s^1\bar{a}\Gamma\omega_c^2}{\left(s^2 + 2\zeta_1\omega_1 + \bar{\omega}_1^2\right)} \tag{40}$$

3.4 Controller Authority Analysis

The objective of the controller is to minimize the displacement response. Hence, the optimal approach for the design of the acceleration feedback controller based on the minimization of the H_2 norm of the closed loop receptance for a given control gain[6]. For such a design, the gain of the controller is a design parameter and the frequency and damping ratio of the controller are

$$\omega_c = \omega_s \tag{41}$$

$$\zeta_c = \frac{1}{2}\sqrt{a_i b \Gamma} \tag{42}$$

In general, the controller parameters are written as functions of structural parameters (i.e., ω_1, ξ_1) and generalized influence parameters of OPSA and sensor (i.e., $\overline{a}$, $\overline{b}$). That is,

$$\omega_{c1} = h_\omega(\omega_1, \zeta_1, \overline{a}, \overline{b}) \tag{43}$$

$$\xi_{c1} = h_\xi(\omega_1, \zeta_1, \overline{a}, \overline{b}) \tag{44}$$

$$\Gamma_1 n_s^1 = h_\Gamma(\omega_1, \xi_1, \overline{a}, \overline{b}) \tag{45}$$

From equations (37) and (38)

$$I_1(j\omega) = \frac{-\overline{b}\omega^2}{(-\omega^2 + j2\zeta_1\omega_1\omega + \omega_1^2)(-\omega^2 + j2\zeta_{c1}\omega_{c1}\omega + \omega_{c1}^2) - \Gamma_1\omega_{c1}^2 n_s^1 \overline{a}\overline{b}\omega^2}\overline{F}_1(j\omega) \tag{46}$$

In this design $\omega = \omega_1$ is chosen. Then,

$$|I_1|_{\omega\omega_1} = \Big|\frac{-\overline{b}}{(j2\xi_1)(-\omega_1^2 + j2\zeta_{c1}\omega_{c1}\omega_1 + \omega_{c1}^2) - \Gamma_1\omega_{c1}^2 n_s^1 \overline{a}\overline{b}}\Big||\overline{F}_1(j\omega)| \tag{47}$$

Substituting the controller parameters given by equations (43) through (45) into equation (47), it is noted that the coefficient on the right-hand side of equation (47) is written as a function of structural parameters and generalized influence parameters of OPSA and sensor. Then,

$$|I_1|_{\omega=\omega_1} = h_g|\overline{F}_1(j\omega_1)| \tag{48}$$

where

$$h_g(\omega_1, \zeta_1, \overline{a}, \overline{b}) = \Big|\frac{-\overline{b}}{(j2\zeta_1)(-\omega_1^2 + j2h_\zeta h_\omega\omega_1 + h_\omega^2) - h_\gamma h_\omega^2 \overline{a}\overline{b}}\Big| \tag{49}$$

From equation (116) and (8), the expression for the blocked force as $|F_c|$ is shown to be

$$|F_c| = k_s^E|V_1(t)| = k_s^E a_1\Gamma_1\omega_{c1}^2|I_1| \tag{50}$$

The maximum block force of a piezoceramic stack is $|F_c|_{max}$. The maximum force that is delivered is a fraction of $|F_c|_{max}$. This is denoted as $|\hat{F}_c|_{max}$

$$|F_c|_{\omega=\omega_1} = k_s^E a_1\Gamma_1\omega_{c1}^2|I_1|_{\omega=\omega_1} \le |\hat{F}_c|_{max} \tag{51}$$

then

$$\Gamma_1 \le \frac{|\hat{F}_c|_{max}}{k_s^E a_1\omega_{c1}^2|I_1|_{\omega=\omega_1}} \tag{52}$$

Substituting equation (48) into (52), the maximum gain under operation is given by,

$$\Gamma_{1,max} = \frac{|\hat{F}_c|_{max}}{k_s^E a_1 \omega_{c1}^2 |I_1|_{\omega=\omega_1}} = \frac{1}{k_s^E a_1 h_\omega^2 h_g} \frac{|\hat{F}_c|_{max}}{|\overline{F}_1(j\omega_1)|} \tag{53}$$

To assure that the designed controller gain is achieved, the specified control performance is realized and the operational safety of the stack is maintained, the designed gain from equation (45) is required to to be less than the maximum gain given in equation (53). This means,

$$\Gamma_{1,design} \leq \Gamma_{1,max} \Leftrightarrow \frac{h_\Gamma}{n_s^1} \leq \frac{1}{k_s^E a_1 h_\omega^2 h_g} \frac{|\hat{F}_c|_{max}}{|\overline{F}_1(j\omega_1)|} \tag{54}$$

From equation (54), the number of actuators is given by

$$n_s^1 \geq \frac{h_\Gamma k_s^E a_1 h_\omega^2 h_g |\overline{F}_1(j\omega_1)|}{|\hat{F}_c|_{max}} \tag{55}$$

Therefore, the minimum number of needed stacks $n_{s,min}^1$ is given by

$$n_{s,min}^1 = h_\Gamma k_s^E a_1 h_\omega^2 h_g \frac{|\overline{F}_1(j\omega_1)|}{|\hat{F}_c|_{max}} \tag{56}$$

To illustrate the procedure, controller parameters[32, 16, 81] (see Appendix A) are derived. From equations(159), it is shown that

$$h_\omega = \omega_1, h_\Gamma = \frac{(\zeta_{c1} - \zeta_1)^2}{|\bar{a}\bar{b}|} \tag{57}$$

From equation (49) h_g is given by

$$h_g = \Big| \frac{\bar{b}}{(\zeta_{c1} + \zeta_1)^2 \omega_1^2} \Big| \tag{58}$$

Substituting equations (57) and(58) into equation (56), the minimum number of needed stacks n^1 is shown to be

$$n_{s,min}^1 = \frac{(\zeta_{c1} - \zeta_1)^2}{(\zeta_{c1} + \zeta_1)^2} \frac{k_s^E a_1}{|\overline{a}|} \frac{|\overline{F}_1(j\omega_1)|}{|F_c|_{max}} = \Big(1 - \frac{2\zeta_1}{\zeta_{c1} + \zeta_1}\Big)^2 \frac{1}{\hat{a}} \frac{|\bar{F}_1(j\omega_1)|}{|\hat{F}_c|_{max}} \tag{59}$$

It has been shown that the minimum number of needed stacks is proportional to the maximum magnitude of encountered aerodynamic loads $|\bar{F}_1(j\omega_1)|$. However, the number can be reduced through choosing "high performance piezoceramic stacks (with large maximum block force $F_{c,max}$)", and/or aligning OPSAs to yield a large generalized influence

Table 1: Open Loop modal Parameters

Mode	Frequency (Hz)	*Damping Ratio* (ζ_1)
1^{st} *Bending Mode*	16.73	0.6%
1^{st} *Torsion Mode*	46.77	0.8%

parameter $\hat{a}$. This number is not dependent on the choice of sensor as the $\overline{b}$ term cancels. From Appendix A, the magnitude of vector $\{\boldsymbol{\Theta}^1\}$ is much smaller than that of $\{\boldsymbol{\Phi}^1\}$, i.e. the first bending-torsional mode is dominated by bending. Thus, the contribution of the second term to the generalized influence parameter can be neglected when compared to the contribution of the first term.

$$\hat{a} \approx h\Delta L cos\alpha_1 \{\boldsymbol{a}^1\}^T [A_{11}] \{\boldsymbol{R}_w\} \qquad [lb \cdot in^2] \tag{60}$$

where

$$\{\boldsymbol{R}_w\} = \{R_{w1}(y_c) \qquad R_{w2}(y_c)\}^T, R_{wi}(y_c) = \frac{\alpha_i'(y_2) - \alpha_i'(y_1)}{L_s} \qquad i = 1, 2$$

where R_{wi} is the curvature of the i^{th} bending mode at y=y_c. From equation (60), it is shown that designing a large offset h, and aligning the OPSA as closely as possible along the elastic axis, a larger value of actuator influence parameter $\hat{a}$ increases the applied control moments. Since $[\boldsymbol{A}_{11}]$ is positive definite, a location of OPSA to a position with large curvature increases the influence parameter. Then, the best location for OPSAs is at the root of the tail and along the elastic axis (i.e. $\alpha_i = 0°$). In summary, the design parameters to obtain a minimum number of piezoceramic stacks are the maximum blocked force $\hat{F}_{c,max}$ for the selected piezoceramic stack, the stack length L_s, the controller damping *c1*, the OPSA offset h, the orientation of OPSA 1, and the location of OPSA y_c. When some specific commercial piezoceramic stacks are chosen, the first two parameters are fixed. The other parameters are subject to other constraints by the design.

The open-loop modal information, obtained from the Figure 18 of the reference[4], is presented in Table 1. From flight test data in reference[4], the worst scenario of buffeting condition is at a 32 degree angle of attack and 300 psf aerodynamic pressure at sea level. The PSD of differential pressure at a typical location on the tail is adapted from the Figure

2 of reference[4].

$$\boldsymbol{PSD}|_{max} = 1.14 psi^2 \tag{61}$$

From the PSD at this typical point, the PSD of the generalized aerodynamic load is calculated using equation (156). M_1 and M_2 are are defined as the number of bending and torsional modes respectively. In Appendix A, $M_1 = M_2 = 2$ is selected. Then, the weighting function g(x,y) as shown in equation (31) becomes

$$g(x,y) = (\{\boldsymbol{\Phi}^1\}^T[A_{11}]\{\boldsymbol{\alpha}(y)\} + x\{\Theta^1\}^T[A_{22}]\{\boldsymbol{\beta}(y)\})$$

The associated generalized aerodynamic modal load is calculated as

$$PSD_1|_{max} = 2.68 \times 10^{21} lb^4 in^6 \tag{62}$$

Then,

$$|\hat{F}_1(j\omega_1)|_{max} = 1.80 \times 10^{13} lb^2 in^3 \tag{63}$$

3.5 Overall procedure

The following is a general procedure for designing an active control system based on using OPSAs as the active element.

1. Characterize the tail structure to be controlled to determine the modes of the structure which are to be controlled. This is typically performed with a random excitation or calculated.

2. Choose the modes to be controlled. Depending on the specific aircraft, particular modes(s) will be dominant. These dominant modes are the modes to be controlled.

3. Determine the actuator and sensor placement. The sensor is placed for maximum observability of the controlled mode(s). Actuator placement is determined by equation (9).

4. Numerically determine the actuator and sensor flexibility influence coefficients per equations (28) and (30).

Table 2: The minimum number of needed piezoceramic stacks ($\alpha_1 = 0, y_c = L_s/2$)

Controller Damping $\zeta_{c1} = 2\% \Rightarrow$ *Response Reduction* 49.6%			
piezoceramic stack ($F_{c,max}, L_s$)	Offset h		
	1 in.	2.5 in.	4 in.
P-830.10 (1 kN, 3 in.)	1688	676	422
P-247.70 (30 kN, 5.7 in.)	32	13	8
Controller Damping $\zeta_{c1} = 4\% \Rightarrow$ *Response Reduction* 79.4%			
P-830.10 (1 kN, 3 in.)	3180	1272	745
P-247.70 (30 kN, 5.7 in.)	59	24	15

5. Determine the type of stack to be used in the control. This allows the calculation of k_s^E.

6. Determine the maximum amount of aerodynamic loading from equations similar to (31) or (32)

7. Determine the maximum amount of gain of the system. It is designed such that the maximum amount of voltage a piezoceramic stack is rated for.

8. To obtain the minimum number of stacks needed equation similar to (59) is used.

9. Determine the final placement of actuators

10. Controller implementation and validation

The needed minimum numbers of selected commercial piezoceramic stacks for various specific performances are estimated and listed in Table 2. The design parameters α_1 and y_c are chosen to be 0 degrees and $L_s/2$ according to the discussions in above. For selected piezoceramic stack, the maximum block force $F_{c,max}$ and L_s are fixed. By varying the controller damping ξ_{c1} and the offset h, the minimum number of piezoceramic stacks is determined by equation (56), which uses the crossover theory. The expected reductions of vibration magnitude are calculated by using equation (161).

3.6 Controller Parameters and Performance

Following the crossover-point theory illustrated in the Appendix A, two specific controllers are designed. The parameters are listed in Table 3. The corresponding transfer functions are shown in Figure 13. The following parameters are used in the design of the controllers.

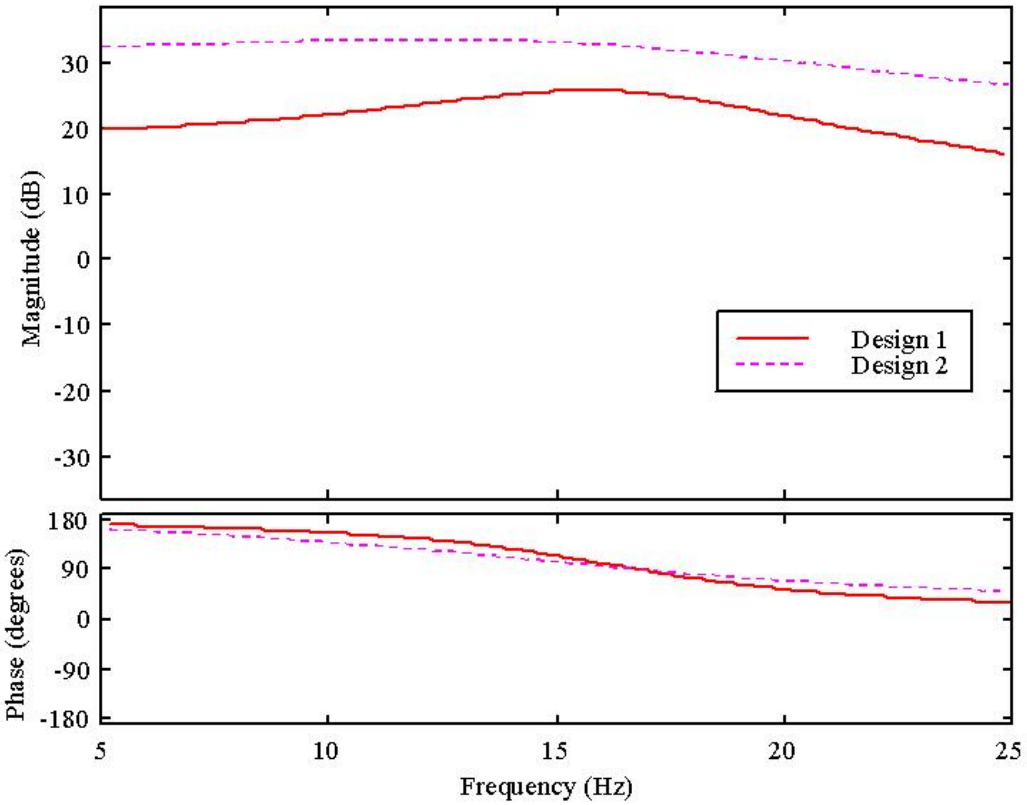

Figure 13: Controller Transfer functions

Table 3: Designed controllers for F/A-18 vertical stabilizer

	Controller Parameters		
Design	*Frequency* f_c (Hz)	*Damping Ratio* ζ_c	*Gain* γ
1	16.73	2%	0.06
2	16.73	4%	0.38

- PI P-247.70 HVPZT stacks as the actuator
- a=10 : This value assumes a PI HVPZT amplifier is used which multiplies the controller voltage by 10.
- n=10 : The number of piezoceramic stacks.
- h=2.5 inch : OPSA offset.
- b=1 : PCB 303A02 accelerometer with a 1v/g sensitivity placed at (x_s, y_s)=(0, L)

With these parameters the gains for two different controller designs are calculated by using equation (158).

The modal transfer functions for both open and closed-loop systems are presented in Figure 14 and show the estimated the performance of the designed AFC. The reductions for design 1 and 2 at the peak (f=16.73Hz), are 55% and 74%, respectively, which are quite close to what was estimated in Table 2. The reductions of PSD of root bending moment at 32 degree angle of attack and 300 psf aerodynamic pressure are calculated and presented in Figures 15 and 16. The open-loop data are obtained from Figure 18 in the reference[4].

3.7 Summary

In this chapter acceleration feedback controllers are designed, with sufficient control authority by using smart structures-based offset piezoceramic stack actuators (OPSA), to control buffet-induced vibrations. The OPSA actuators are designed to provide sufficient control authority to control the buffet induced vibrations in an F/A-18 aircraft. Questions of optimum placement of these actuators, optimum design of the controllers and minimum number of needed actuators are addressed. These solutions are required to accurately design minimum weight controllers with sufficient control authority, observability issues are

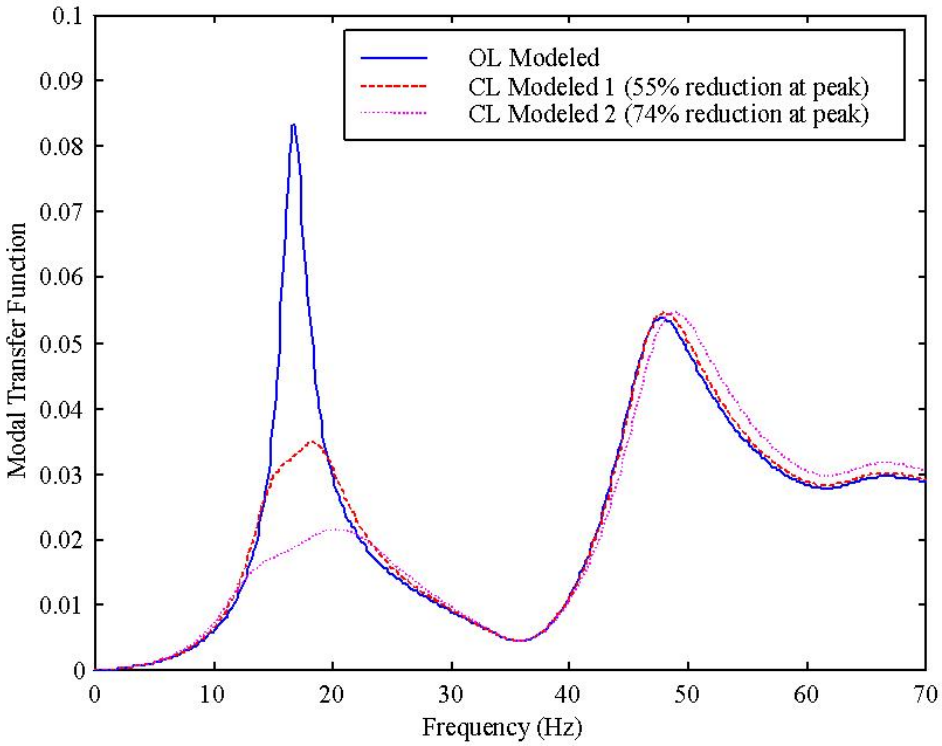

Figure 14: The open and closed-loop modal transfer function

also addressed where necessary.

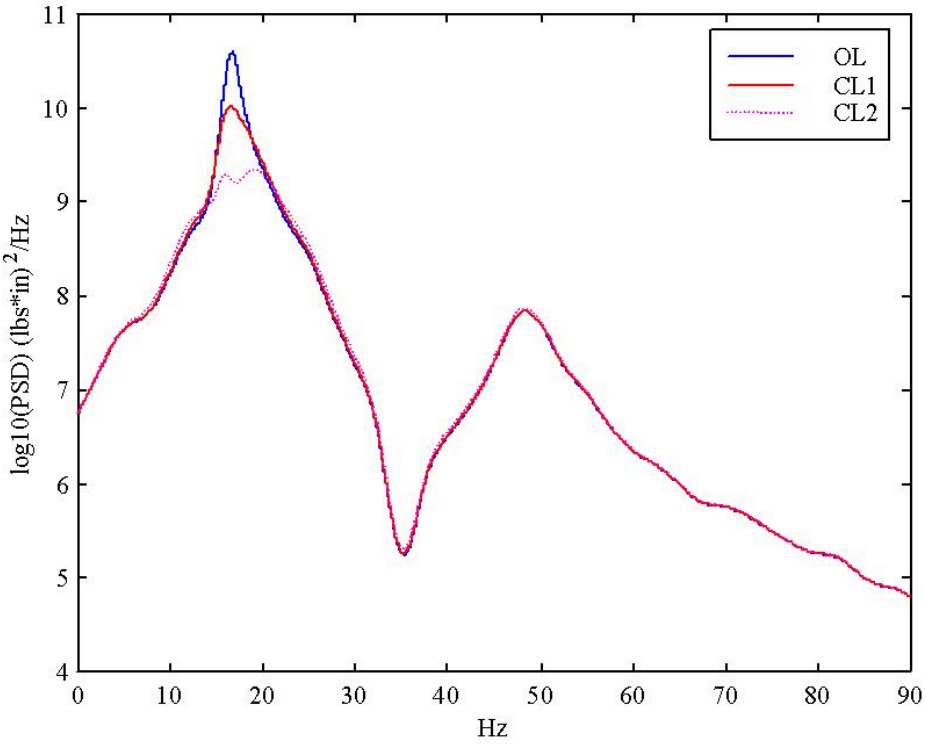

Figure 15: Open and closed loop PSD of F/A-18 tail root bending moment at 32° angle of attack and 300psf aerodynamic pressure logarithm scale

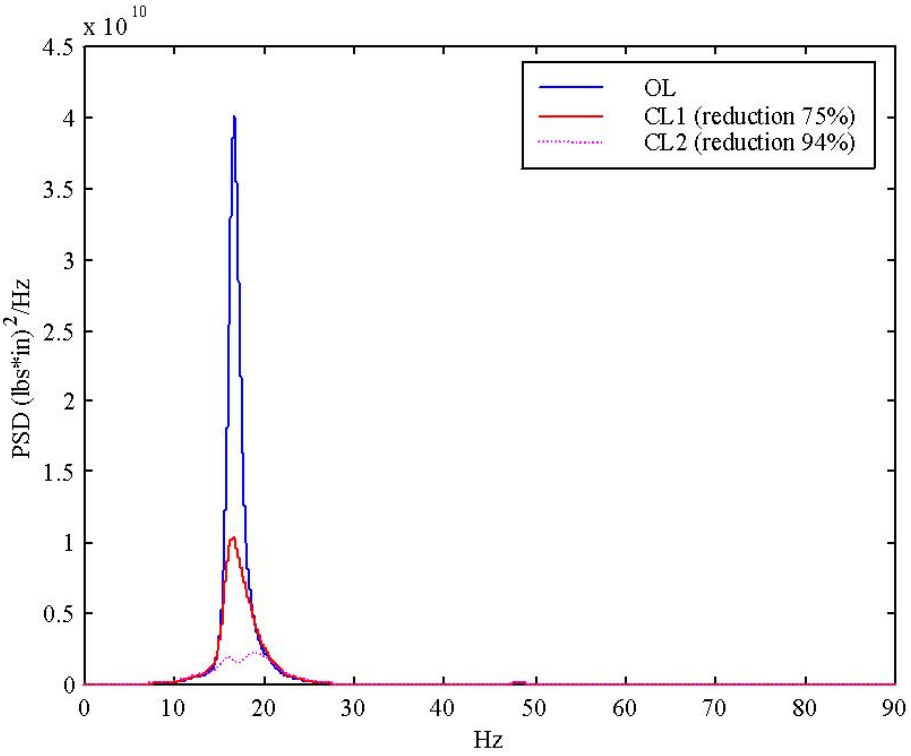

Figure 16: Open and closed loop PSD of F/A-18 tail root bending moment at 32° angle of attack and 300psf aerodynamic pressure linear scale

Chapter IV

ADAPTIVE NEURAL NETWORK AUGMENTATION FOR CONTROL OF BUFFET INDUCED VIBRATIONS

4.1 Source of uncertainties due to debonds in the F/A-18 vertical tail

In the case of the F/A-18 vertical tail there are two primary sources of uncertainty (1) frequency shift due to changes in the airspeed and (2) delaminations between the skin and the honeycomb core. In the first case as the airspeed increases the value of the first bending natural frequency increases[7]. Such a shift of the natural frequency causes controllers, which are tuned to this frequency, to become much less effective.

Debonds between the skin and the stiffener/honeycomb can occur for a variety of reasons such as fatigue due to buffet loading and/or moisture introduced through fatigue cracks. As these debonds grow the structural frequency changes would be significant. The objective is to determine if the adaptive neural network is capable of augmenting a linear controller and control buffet induced vibrations with a debond in a vertical tail.

Lestari[53] studied the effects of nonlinearities due to dbonds on the vibration of beams by including the nonlinear axial stretch effects and amplitude dependent axial interactions. When a beam with delamination vibrates, the delaminated segment of the beam is subjected to an axial load due to the resistance of the rest of the beam on the delaminated segment (Figure (17). This load adds a nonlinear term in the governing equation of the beam (64). This model is modified to study vibration of the vertical tail.

The delaminated section is not completely free to vibrate. It is free to vibrate away from the beam but cannot penetrate the beam when it moves toward the beam.

The linear free vibration analysis allows the delaminated segment to separate from the rest of the beam. For a thin delamination, as in the case of a skin on the F/A-18 tail, the delaminated segment is approximated by of an Euler-Bernoulli beam segment with elastic lateral and rotational supports.

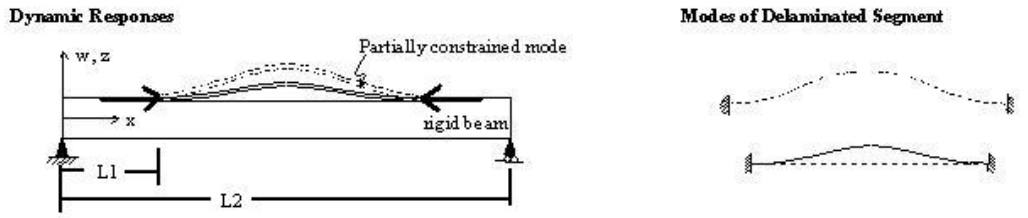

Figure 17: Rigid beam and partially constrained elastic delaminated segment[53]

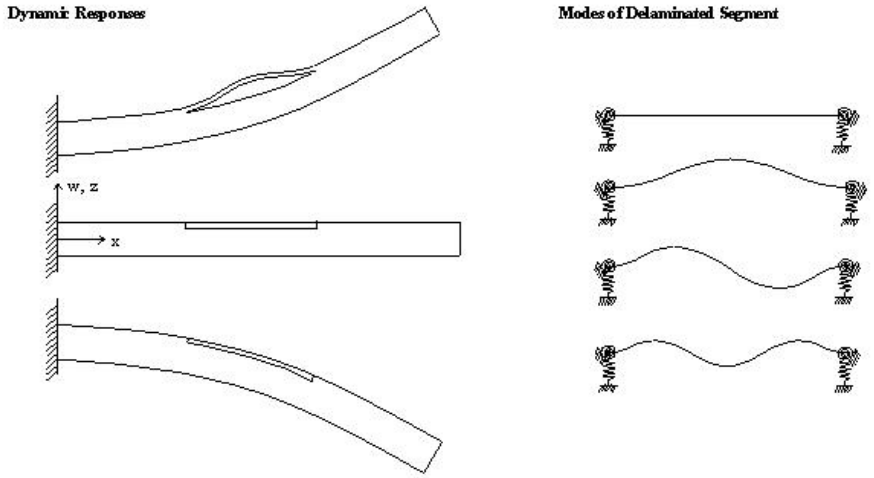

Figure 18: Free and constrained modes in dynamic response[53]

The delaminated segment deflects away from the rest of the beam when the compression load on the delaminated segment exceeds the buckling load of the segment. This corresponds to the first mode. When the beam deflects in the other direction the delamination is in tension. Then, the two segments move together corresponding to the second mode in the free vibration analysis or the first fully constrained mode. The penetration is thus avoided.

To begin describing the development, the equation of motion with the nonlinear term is as follows.

$$EI\frac{\partial^4 w}{\partial x^4} + \mu\frac{\partial^2 w}{\partial^2 t} + P\frac{\partial^2 w}{\partial x^2} - \frac{EA}{2L}\int_0^L \left(\frac{\partial w}{\partial x}\right)^2 dx\frac{\partial^2 w}{\partial x^2} = F(x,t) \tag{64}$$

where *EI* is the flexural rigidity, *EA* is the axial rigidity, L is the length of the beam, μ is the mass per unit length, P is the axial load and *F(x,t)* is the lateral loading function. The nonlinear term that appears in equation (64) is due to the interaction of the transverse deflection and the axial force caused by axial restraint. The beam may vibrate with large amplitudes; however, deflections are assumed small enough that the linear approximation for curvatures is still valid.

The boundary conditions at x=0 are

$$\alpha_0 \mathrm{w}_0 = -\mathrm{EI}\frac{\partial^3 w}{\partial x^3}, \quad \beta_0 \frac{\partial \mathrm{w}}{\partial \mathrm{x}} = \mathrm{EI}\frac{\partial^2 w}{\partial \mathrm{x}^2} \tag{65}$$

The boundary conditions at x=L are

$$\alpha_1 \mathrm{w}_1 = \mathrm{EI}\frac{\partial^3 w}{\partial x^3}, \quad \beta_1 \frac{\partial \mathrm{w}}{\partial \mathrm{x}} = -\mathrm{EI}\frac{\partial^2 w}{\partial \mathrm{x}^2} \tag{66}$$

where α_0 and α_1 are the linear spring constants, and β_0 and β_1 are the rotational spring constants at x=0 and L, respectively.

4.1.1 Nonlinear Vibration Analysis for Fixed Beams

The exact solution for the nonlinear problem of vibrations of buckled beams with fixed ends is expanded using Jacobi elliptic functions[53]. The linear modes shape for a fixed-fixed beam is

$$\phi(x) = \cos\left(\tfrac{\gamma x}{L}\right) - \cosh\left(\tfrac{\gamma x}{L}\right) + R\left(\sin\left(\tfrac{\gamma x}{L}\right) - \sinh\left(\tfrac{\gamma x}{L}\right)\right) \tag{67}$$

where

$$R = \frac{\sin(\gamma) + \sinh(\gamma)}{\cos(\gamma) - \cosh(\gamma)} \tag{68}$$

γ is a constant that depends on the boundary conditions of the beam.

The displacement function is assumed in the following form to solve the nonlinear problem

$$w_i(x,t) = \hat{a}_i \phi_i(x) \psi_i(t) \tag{69}$$

In this equation, $\psi_i(t)$ is an arbitrary function of time, $\phi_i(x)$ are the original mode shapes of Figure (18) and $\hat{a}_i$ are arbitrary constants. Substituting equation (69) and its derivatives into the governing equation (64) for the nonlinear problem, then multiplying by ϕ_j and integrating in the domain of the beam gives

$$\ddot{\psi} + \left(\frac{EI}{\mu}\Phi_4 + \frac{P}{\mu}\Phi_2\right)\psi - \frac{EI}{2\mu L}\left(\frac{\hat{a}}{r}\right)^2 \Phi_1 \Phi_2 \psi^3 = 0 \tag{70}$$

where

$$\Phi_4 = \frac{\int_0^L \phi^{(iv)}\phi dx}{\int_0^L \phi^2 dx}, \quad \Phi_2 = \frac{\int_0^L \phi''\phi dx}{\int_0^L \phi^2 dx}, \quad \Phi_1 = \int_0^L \left(\phi'\right)^2 dx \tag{71}$$

r is the radius of gyration, and is defined as

$$r = \sqrt{\frac{I}{A}} \tag{72}$$

Integrating equation (70) once with respect to time gives

$$\left(\frac{d\psi}{dt}\right)^2 = \chi_1(1-\psi^2) + \frac{\chi_2}{2}(1-\psi^4) \tag{73}$$

where

$$\chi_1 = \left(\frac{EI}{\mu}\Phi_4 + \frac{P}{\mu}\Phi_2\right), \quad \chi_2 = -\frac{EI}{2\mu L}\left(\frac{\hat{a}}{r}\right)^2 \Phi_1 \Phi_2 \tag{74}$$

The parameter χ_1 and χ_2 are regrouped in the following way

$$p^2 = \chi_1 + \chi_2, \quad k^2 = \frac{\chi_2}{2p^2} \tag{75}$$

such that the differential equation has solutions in terms of Jacobi elliptic function. Equation (73) is rewritten as follows

$$\left(\frac{d\psi}{d(pt)}\right)^2 = (1-\psi^2)(k^2\psi^2 - k^2 + 1) \tag{76}$$

assuming $\psi = cos\varphi$ a Jacobi elliptic function with the modulus k is obtained

$$pt = \int_0^{\varphi} \frac{d\varphi}{\sqrt{(1 - k^2 \sin^2 \varphi)}} \tag{77}$$

From the inversion of equation (77) the solution for ψ is obtained as follows

$$\psi = cn[pt, k] \tag{78}$$

The Jacobi elliptic functions are real for real p and real k^2 between 0 and 1. For $k^2 = 0$ the function reduces to the elementary trigonometric function cos(pt) with the period of 2π. In this case, the motion of the beam is harmonic. In other words the nonlinear effects are not included, for $\chi_2 = 0$. For $k^2 = 1$ the function reduces to elementary functions sech(pt) and the motion of the beam is aperiodic, approaching the straight position asymptotically with time. In this case, the external axial resistance load from the end of the beam on the delaminated segment, P, exceeds the buckling load of the beam segment and the axial load due to axial stretching cannot compensate this load. Therefore, when the axial load is greater than the buckling load, large amplitude deflections are required in order to cause the beam to vibrate, such that $\chi_2 > \chi_1$. The period of the function cn[pt, k] is 4K and is defined by using the complete elliptic integral.

$$4K = 4 \int_0^{\pi/2} \frac{d\varphi}{\sqrt{1 - k^2 \sin^2 \varphi}} \tag{79}$$

The corresponding frequency for this nonlinear problem for each mode is defined by using the following

$$\tilde{\omega}_i = \frac{\pi \sqrt{\chi_1 + \chi_2}}{2K} \tag{80}$$

Using equation (69) the expression for the solution for the free vibration of a buckled beam with arbitrary rotational end restraints is obtained in the form of

$$L1 < x < L2; w(x,t) = \hat{a} \left\{ \cos\left(\tfrac{\gamma x}{L}\right) - \cosh\left(\tfrac{\gamma x}{L}\right) + R\left(\sin\left(\tfrac{\gamma x}{L}\right) - \sinh\left(\tfrac{\gamma x}{L}\right)\right) \right\} cn\,[pt, k] + w_{verticaltail} \tag{81}$$

This will be the uncertainty in the response.

4.2 Adaptive control methods

It is assumed that a linear acceleration feedback controller is already installed on an aircraft to control buffet induced vibrations in the vertical tail and cannot be replaced. The linear controller must be augmented in such a way as to recognize any shift in the modal frequency or added unmodeled dynamics or nonlinear dynamics due to disbonds and adjust its ability to control it. If the form of the uncertainties is not well understood adaptive methods are used to estimate and cancel the effect of uncertainty while operating in parallel with the linear controller. One of the most promising forms of adaption is the use of neural networks.

4.2.1 Background of neural networks

Neural networks are universal approximators, meaning that there exists a set of weights (**N**,**M**) and basis functions F (Figure (19)) that are used to approximate a map y=f(x) to arbitrary accuracy for all $x \in X$, where X is a bounded set in $\Re^n$[24]. The weights of the connections from the input layer to the hidden layer are the elements of $\boldsymbol{N}$. The weights of the connections between the hidden layer and the output layer are the elements of $\boldsymbol{M}$. The input to each F is the product of N_i and x, where N_i is the i^{th} row of $\boldsymbol{N}$, and x is the input vector. The mapping ability of a neural network is derived from its ability to adjust the weights ($\boldsymbol{N}$, $\boldsymbol{M}$) of the connections between the nodes.

One of the key developments in neural network research are the equations that determine and relate **N** and **M**. These equations are called update laws. In order to use a neural network for a given task the weights of these connections must be determined. The process of adjusting these weights is called training the network. This training typically proceeds as follows

1. A set of inputs is fed into the network.

2. The calculated network output is compared to the correct output and any difference is considered an error.

3. The error is used to adjust the network weights by the use of update laws.

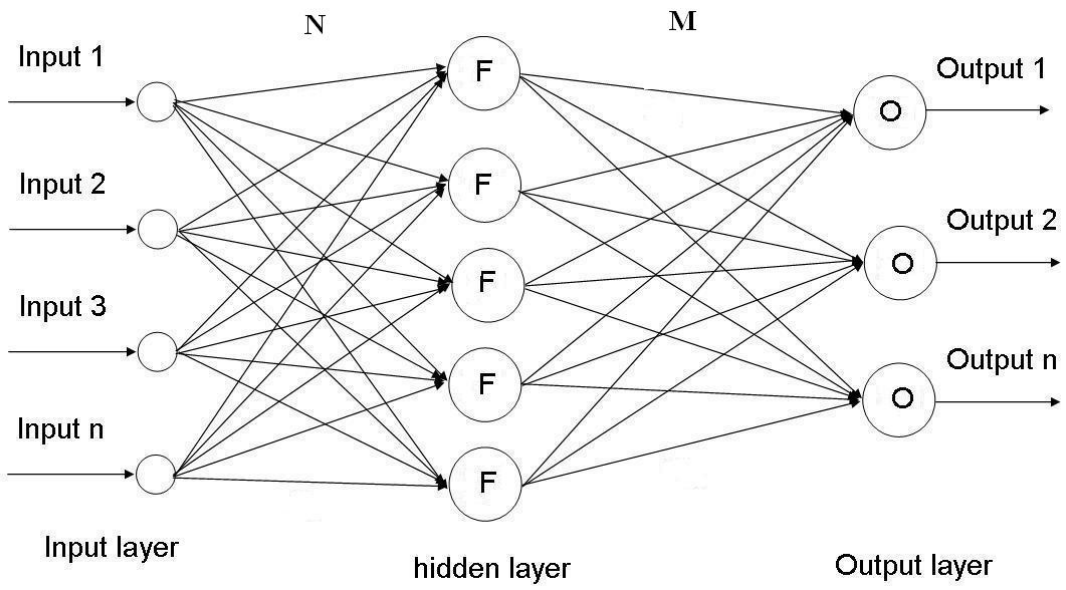

Figure 19: A typical multi-layered neural network

This process is repeated until the amount of error falls within a specified tolerance. For an adaptive neural network this adjustment of the weights or training must occur while the neural network is in use[12].

4.3 Neural network control system for F-18

In sections 4.1 and 4.2, two important problems that occur in the field of the control of buffet-induced vibrations are discussed. The problems originate from mechanisms that lead to uncertain systems. In the recent past, there are many approaches that have addressed these uncertainties. Some of these achievements include robust design methods[66, 11], output feedback controllers[41], back-stepping design methods[8], input-to-state stability[77], and decentralized stabilization[67]. Most of the progress in the control of uncertain systems is based on certain restrictive assumptions on the types of nonlinearities in the system. To remove some of the restrictive assumptions neural networks have been used to cancel the effect of unmodeled uncertainty[12, 13, 107, 105, 40, 39].

In the problem of the control of buffet-induced vibrations in twin tail aircraft there are parameter shifts. The unknown debonds include a nonexistence of debonds to many debonds of variable sizes, unknown locations and unknown orientations. The control problem is not

one of tracking a bounded smooth reference trajectories $y_{ci}(t)$. The objective of the control is to minimize or reduce to zero all the measured outputs y_i.

4.3.1 Problem formulation

The strict relative degree is determined by the number of times the system output must be differentiated such that the control term appears in the equation[85]. For linear systems the relative degree is determined by the difference between the number of poles minus zeros. The adaptive neural network research is based [13, 105] on relative degree that is greater than zero to determine design parameters.

The relative degree of acceleration is zero as seen by multiplying eqn. (40) by s^2. Therefore, because the measured output of the plant is acceleration, this would preclude the use of the adaptive neural network. However, if the output is filtered the relative degree that the neural network observes is greater than zero. For this work a band pass filter is used to filter the output of the plant. A typical bandpass filter is of the form

$$H(s) = \frac{K_f s}{s^2 + B_f s + \omega_o^2} \tag{82}$$

where

- K_f : Filter gain
- B_f : 3-dB Bandwidth (rad/s)
- ω_o^2 : Resonant Frequency (rad/s) or center frequency of passed frequency band

The band pass filter has a relative degree of one. The plant output is passed through the band pass filter then this filtered signal is passed to the neural network. The transfer function of the filtered plant where the plant output is acceleration is given as

$$G_{Plant_f} = \frac{-n_s^1 \bar{a} \Gamma \omega_c^2 s^2}{\left(s^2 + 2\zeta_1 \omega_1 s + \bar{\omega}_1^2\right)} \frac{K_f s}{(s^2 + B_f s + \omega_o^2)} \tag{83}$$

Therefore, when using the band pass filter the neural network observes the F-18 plant/linear controller to have relative degree of one. Any delamination is weakly nonlinear so this relative degree assumption should still be valid.

The system is written in normal form[85]

$$
\begin{aligned}
&\dot{x}_1 = x_2 \\
&\vdots \\
&\dot{x}_4 = -\left(B_f + 2\zeta_1\omega_1\right) x_4 - \left(\omega_0^2 + 2\zeta_1\omega_1 B_f + \bar{\omega}_1^2\right) x_3 - \left(2\zeta_1\omega_1\omega_0^2 + B_f\bar{\omega}_1^2\right) x_2 - \omega_0^2\bar{\omega}_1^2 x_1 \\
&-n_s^1\bar{a}\Gamma\omega_c^2 K_f[u + \Delta_1(z_2, \boldsymbol{\xi}, u)] \\
&\dot{z}_2 = f(z_2, \boldsymbol{\xi}) \\
&y = x_5
\end{aligned}
\tag{84}
$$

where $u \in R^1$ and $y \in R^1$ are the control and measurement variables, $\boldsymbol{\xi} = [x_1 \cdots x_r]$, z_2 represents the unmodelled dynamics, and Δ_1 is the matched uncertainty which is defined as.

$$
\begin{aligned}
&\Delta_1(z_2, \boldsymbol{\xi}, u) = \tfrac{1}{n_s^1\bar{a}\Gamma\omega_c^2 K_f}[h(z_2, \boldsymbol{\xi}, u) + \left(B_f + 2\zeta_1\omega_1\right) x_4 + \left(\omega_0^2 + 2\zeta_1\omega_1 B_f + \bar{\omega}_1^2\right) x_3 \\
&+ \left(2\zeta_1\omega_1\omega_0^2 + B_f\bar{\omega}_1^2\right) x_2 + \omega_0^2\bar{\omega}_1^2 x_1 + n_s^1\bar{a}\Gamma\omega_c^2 K_f u]
\end{aligned}
\tag{85}
$$

where h is an unknown continuous function. For the linear controller the state space model becomes

$$
\begin{aligned}
\dot{x}_c &= A_c x_c + B_c(y_c) \\
u_c &= C_c^t x_c + D_c(y_c)
\end{aligned}
\tag{86}
$$

where

$$
A_c = \begin{bmatrix} 0 & 1 \\ -\omega_1^2 & -2\zeta_1\omega_1 \end{bmatrix} \tag{87}
$$

$$
B_c = \begin{bmatrix} 0 \\ \bar{b} \end{bmatrix} \tag{88}
$$

$$
C_c = \begin{bmatrix} 1 & 0 \end{bmatrix} \tag{89}
$$

$$
D_c = 0 \tag{90}
$$

where $\bar{b}$ is defined in the last chapter as a structural influence coefficient. The linear controller is designed to track y=0. With the linear controller defined in state space the

following system matrices are defined as

$$\bar{A} = \begin{bmatrix} A_m - b_m D_c & 0 & b_m C_c^T \\ 0 & 0 & 0 \\ -B_c & 0 & A_c \end{bmatrix}$$
$$\bar{B} = \begin{bmatrix} b_m D_c \\ 0 \\ B_c \end{bmatrix} \tag{91}$$
$$\bar{c}_y = \begin{bmatrix} 1 \\ 0 \\ 0 \end{bmatrix}$$

where

$$\begin{aligned} A_m &= [(B_f + 2\zeta_1\omega_1)] \\ b_m^T &= \left[n_s^1 \bar{a}\Gamma\omega_c^2 K_f\right] \end{aligned} \tag{92}$$

$\overline{A}$ is designed to meet Hurwitz which means the real part of the eigenvalues of $\overline{A}$ are negative. Let

$$u = u_c - u_{ad} \tag{93}$$

When the control signal u is applied to the system in (84), it results in the following closed loop system

$$\begin{aligned} \dot{x} &= \bar{A}x - \bar{B}u_{ad} + \Delta_1 \\ \dot{z}_2 &= f(z_2, \xi) \\ y &= \bar{c}_y x \end{aligned} \tag{94}$$

The objective of the control design is to augment the linear controller (u_c) with the adaptive signal (u_{ad}) so that Δ_1 is canceled. The error vector is defined as

$$E^T \triangleq \left[(\xi)^T (z_2)^T (x_c)^T\right] \tag{95}$$

Using eqn. (94) the modified error dynamics formulation is written as

$$\begin{aligned} \dot{E} &= \bar{A}E + \bar{B}(u_{ad} - \Delta_1) \\ z &= \bar{C}E \end{aligned} \tag{96}$$

where z contains the signals for feedback.

$$z = \begin{bmatrix} y \\ x_c \end{bmatrix} \tag{97}$$

This gives

$$\bar{C} = \begin{bmatrix} -\bar{\omega}_1^2 & -2\zeta 1\bar{\omega}_1 \\ 1 & 0 \end{bmatrix} \tag{98}$$

When structural parameters shift due to damage or aeroelastic effects they can change in an unpredictable manner. The neural network signal then augments the linear controller signal and approximately cancels the effect of the uncertainty. Equation (96) shows that the control signal u_{ad} is designed to approximately cancel the matched uncertainty Δ_1. The reason it is approximate and not exact is because Δ_1 is uncertain or not entirely known. A single hidden layer in the adaptive neural network is used to approximate Δ_1.

Because $\overline{A}$ is Hurwitz by design there exists a unique solution P $= P^T > 0$ such that for any $Q > 0$ (See Appendix D)

$$\bar{A}^T P + P\bar{A} + Q = 0 \tag{99}$$

The value of P is used in the neural network update laws. The neural network input vector φ is constructed using the input to the plant u and its output y as follows

$$\varphi(t) = [1 \;\; \mathbf{u}_d^T(t) \;\; \mathbf{y}_d^T(t)]^T \tag{100}$$

where

$$\mathbf{u}_d^T(t) = [u(t) \;\; u(t-d) \;\; \ldots u(t-(n_1-r-1)d]^T \tag{101}$$

$$\mathbf{y}_d^T(t) = [y(t) \;\; y(t-d) \;\; \ldots y(t-(n_1-1)d]^T \tag{102}$$

in which n_1 is the length of the window and is generally required to be greater or equal to the system dimension n, $d > 0$ is a user defined time delay, and r is the relative degree of the output[13].

The neural network signal in each time estimate is calculated to be

$$u_{ad} = \hat{M}^T \sigma\left(\hat{N}^T \varphi\right) \tag{103}$$

Yang et al.[106] derived the update law which is used in this work to train this neural network in eqn. (104)

$$\begin{aligned} \dot{M} &= -\Gamma_M \left[\left(\hat{\sigma} - \hat{\sigma}'(N^T\varphi) \right) E^T P \bar{B} + kM \right] \\ \dot{N} &= -\Gamma_N \left[\varphi E P \bar{B} M^T \hat{\sigma}'(N^T\varphi) + kN \right] \end{aligned} \tag{104}$$

where the following parameters are defined as:

- Γ_M and $\Gamma_N > 0$: Positive definite adaptation gain matrices which are adjusted by the user until the desire neural network performance is achieved.
- $k > 0$: σ-modification constant.
- $\hat{\sigma}'$: The basis function Jacobian computed at each estimate
- $\hat{\sigma}$: The basis function in each hidden layer node
- E : The training signal.
- φ : The input signal to the neural network.
- $\bar{B}$: Input coefficient matrix in state space.
- P : Positive definite solution to the Liapunov equation in (99).

This update law in (104) is different from the law originally derived by Lewis[54] in that these update laws use P and $\bar{B}$ in the first term.

The sigmoid function σ used in this work for the basis function takes the form

$$\sigma = \frac{1}{1 + e^{-t}} \tag{105}$$

Because the goal of the control design is to remove any vibration (y=0) there is no need for a reference model. Therefore, one of the objectives of the control design in this work is to augment the linear controller (u_c) with the adaptive signal (u_{ad}) so that Δ_1 is canceled without the use of a reference model. A block diagram of the control scheme is shown in Figure (20).

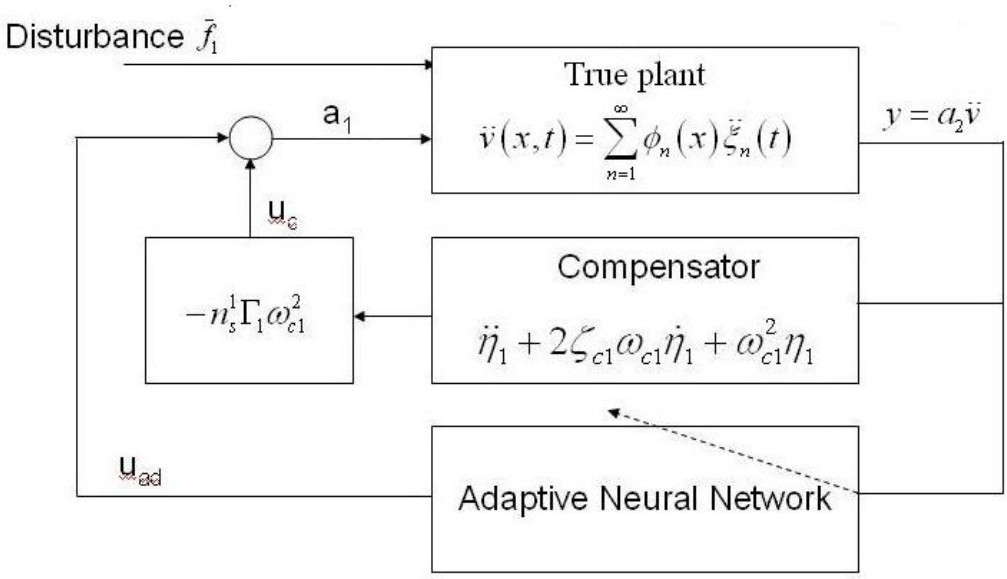

Figure 20: Adaptive Control Augmentation

4.3.2 Overall procedure

The following is a general procedure for designing an active control system based on using OPSAs as the active element with an augmented adaptive neural network.

1. The first step is to characterize the tail structure to be controlled to identify modes of the structure which are controlled. This is typically performed with a random excitation.

2. The next step is to choose the modes to be controlled. Depending on the specific aircraft, particular modes(s) will be dominant. These dominant modes are the modes to be controlled.

3. Then, it is necessary to determine the actuator and sensor placement. The sensor is placed for maximum controlled mode(s) observability. Actuator placement is determined by equation (9).

4. Numerically the actuator and sensor flexibility influence coefficients per equations (28) and (30) are determined.

5. The type of stack to be used in the control is determined. This allows the calculation of k_s^E.

6. Then, the maximum amount of aerodynamic loading is calculated from equation (31) or (32)

7. The maximum amount of gain the equipment used can produce is determined. This must be limited by the maximum voltage a piezoceramic stack is rated for.

8. To obtain the minimum number of stacks needed equation (59) is used.

9. Input/adjust neural network gain matrices to obtain desired neural network response

10. Initial implementation of controller. If network weights do not converge, repeat previous step.

11. Controller implementation and validation. In this step, the closed loop behavior is tested and compared with known results. If the controller is numerically implemented then its performance must be compared to theoretical performance. If the controller is experimentally implemented then its performance must be compared to numerical performance.

4.4 Experimental F-18 control system

4.4.1 Model construction

To experimentally test the buffet induced vibrations on the tails and the control scheme, a wind tunnel aeroelastically scaled model of the F/A-18 vertical tail is constructed. The scaling is calculated by using the Strouhal number (106) equation. Typically, subsonic rigid wind tunnel models are manufactured from hard materials to ensure relative rigidity of the parts of the model. The main requirement of the wind tunnel model used in this investigation is that the portion of the model forward from the empennage to be rigid as possible while allowing an aeroelastically scaled empennage system to be fully attached to the rigid parts of the model assembly. The previous research in tail buffet alleviation with the F-15[15] was successful in creating subsonic wind tunnel models that meet this

requirement by modifying commercially available airplane kits. The model for this work is a 1/12th scale F-18 model kit purchased from JD Enterprises (http://www.jdenterprise.net).

A first step in the construction process is to stiffen the fuselage so that it is relatively rigid (Figure 21). A wing box/fuselage skeleton is designed and constructed for this purpose. This steel structure is a wing box assembly with attach points in the rear for the empennage, a plate on the bottom for a stinger mounting bracket, and a T-beam welded to the front which is extended to the nose. The wings are attached to the wing box by means of three bolts in each wing. Aluminum spacers in the shape of the root airfoil are sandwiched between the inside of the fiberglass skin and the body stiffening structure. The primary purpose of the bolts and space is for local stiffening and to carry the wing loads. The rigidity of the wings is increased so that no wing response is observed at the vertical tails when the model is subjected to a random excitation.

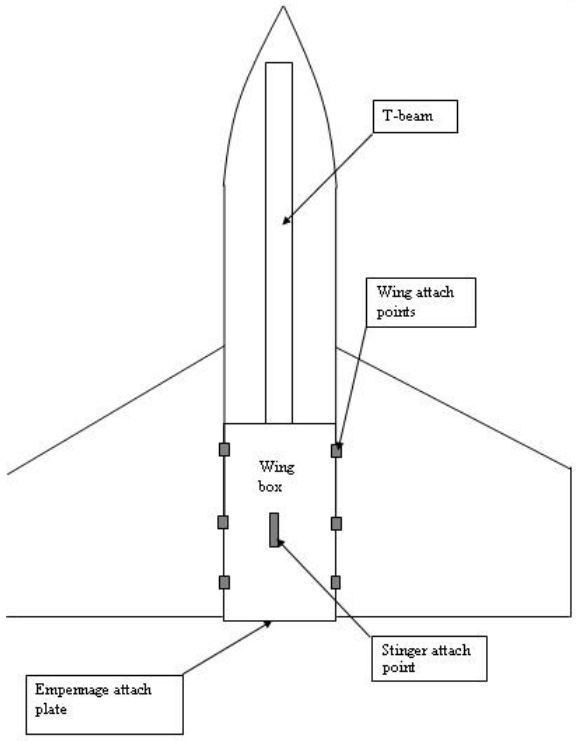

Figure 21: F/A-18 wind tunnel model steel sub-structure

The specifications of the F/A-18 aircraft model are given in Table 4. The fuselage is made of epoxy fiberglass, with glass encapsulated foam core wings.

Table 4: Dimensions of the Modified F/A-18 model

Length	63 inches
Wing Span, shortened	29 inches
Weight Approx (empty)	28 lbs
Scale	$\frac{1}{12}^{th}$ scale

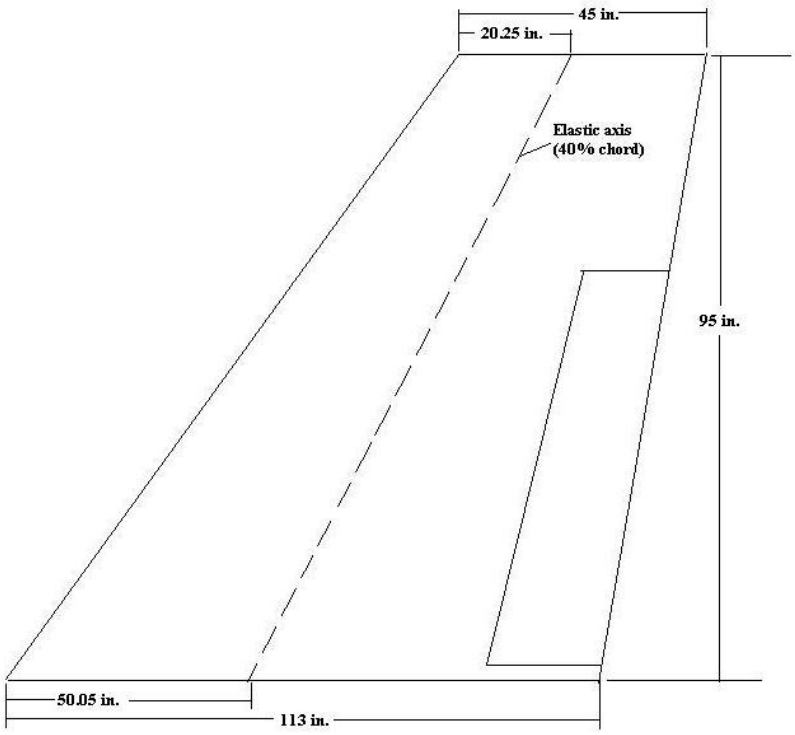

Figure 22: Dimension of F/A-18 vertical tail (full scale)[4]

The wind tunnel used is the Georgia Tech Research Institute (GTRI) Model Test Section (MTF) closed return, subsonic wind tunnel. The cross sectional dimensions of this tunnel are 43-3/8 inches tall x 30-3/8 inches wide. The usable length of the tunnel is 90 inches. To obtain 32 degrees of angle of attack (worst case scenario) the model is mounted from the side of the tunnel to clear the walls when pitched to higher α. This is acceptable as this test does not measure forces and moments through the balance. The full wingspan of the original model is 48 inches, which is too large for the wind tunnel test section width. Therefore, 9 inches is removed from the wing at each wing tip. Symmetric oval end plates are attached to the new wing tips to abate any vortices that could be created from 3-D lifting wing tip geometries after wing shortening.

Severe buffeting occurs when the dynamic pressure is approximately 300 psf, 32 degrees angle of attack on the actual full-scale F-18[4]. Since this model is 1/12 scale, the ratio of characteristic lengths is 1/12. The mean chord of the F-18 vertical tail is 79 inches. The GTRI tunnel is capable of obtaining dynamic pressures of up to 15 psf. The GTRI wind tunnel staff set a sustained limit of 12 psf (= 31.42 m/s) for the experiments due to the size of the model when compared to the cross section area of the tunnel (46 in. $\times$ 48 in.).

To determine the aeroelastic scale factor for the vertical tail the reduced frequency r is determined. The reduced frequency, r, is defined to be a function of the vertical tail mean aerodynamic chord, c, the buffet frequency, f, and the free stream velocity, U_∞ The equation is of the form:

$$r = \frac{f \times c}{U_\infty} \tag{106}$$

f frequency

c characteristic length

U_∞ air stream speed

$$\frac{f_{model}}{f_{actual}} = \frac{U_{\infty model}}{U_{\infty actual}} \times \frac{c_{actual}}{c_{model}} = \frac{31.42 m/s}{201.17 m/s} \times 12 = 1.8742 \tag{107}$$

The horizontal and vertical tails are designed and manufactured at Georgia Tech in the composites lab. A fiber/matrix mixture of a glass fiber cloth with 0-90 deg woven weave,

and Bondo resin with hardener is used to make the composite tails. These materials are the same materials used in the previous F-15 tail buffet work[71]. A vacuum process is used during curing to remove any trapped air bubbles between the lamina. The horizontal tails have a metal rod inserted at mid-span for stiffening purposes and for a means of connection to the empennage assembly. Large metal masses are added to the underside of the horizontal tails so their dynamic response are not confused with the vertical tails.

The structure of the empennage consists of nine pairs of aluminum rings to simulate fuselage frames, which support the engines and the vertical and horizontal tails. These rings are 0.5 inch long and 0.125 inch thick. The centers of the paired rings are spaced 3.25 inches apart and each pair is separated 1 inch from the adjacent pair. Composite strips above and below reinforce the rings and simulate the rib structure in the actual F/A-18. These rings are bolted inside two 13.5-inch C-channel longerons. A metal L-bracket is bolted to the top surface of the C-channel longerons. The composite vertical tails are bolted on to these L-brackets. A V-shaped plate is bolted to the assembly at about 70% of the C-channel longerons length and serves as one of the connections for the horizontal tail. The horizontal tail is mounted by means of a three-point connection using three rods. These three rods, parallel to the elastic axis, are installed in each horizontal tail during the lay-up of the lamina before curing in an autoclave. The free ends of these rods are threaded to allow installation through the vertical tail C-channel longeron and fastened by threaded nuts. The other two connections are to the C-channel longerons bolt holes which are shared by a pair of rings. One end of the C-channel longeron is bolted to a flat metal plate. This metal plate is bolted to the back end of the body stiffening structure discussed earlier. The empennage is installed to the back of the wing box with eight hex bolts. The fiberglass skin is cut into pieces and attached with threaded fasteners. This overall design allows the model to be disassembled and reassembled at any time and allows parts to be changed out.

Once the empennage has been assembled adjustments are made to the installation bolts to get the dynamic response of the vertical tails as close to calculated values as possible.

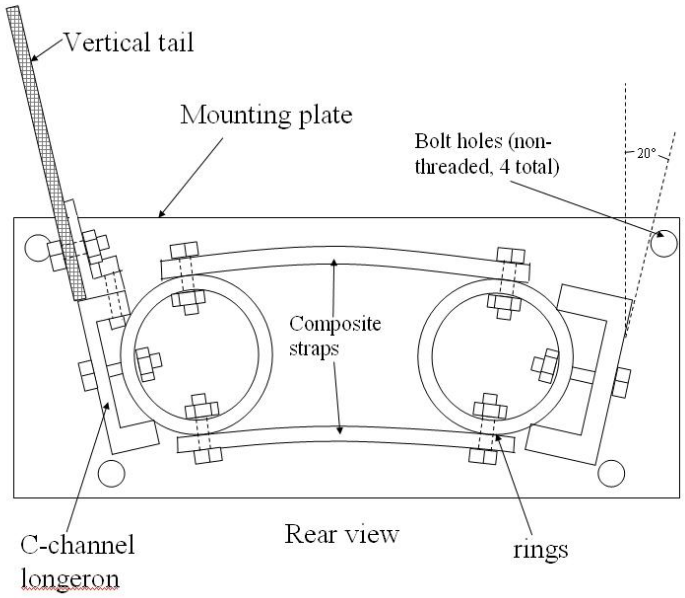

Figure 23: F/A-18 wind tunnel model empennage design rear view looking forward

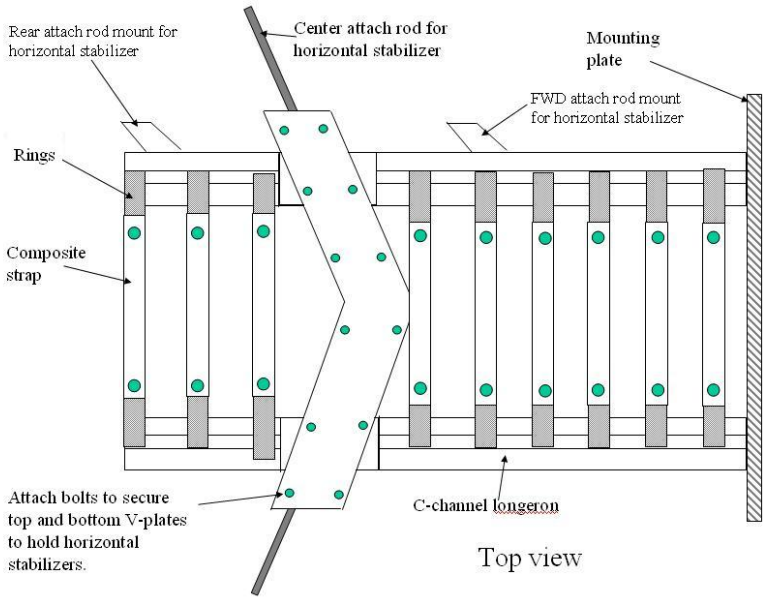

Figure 24: F/A-18 wind tunnel model empennage design top view

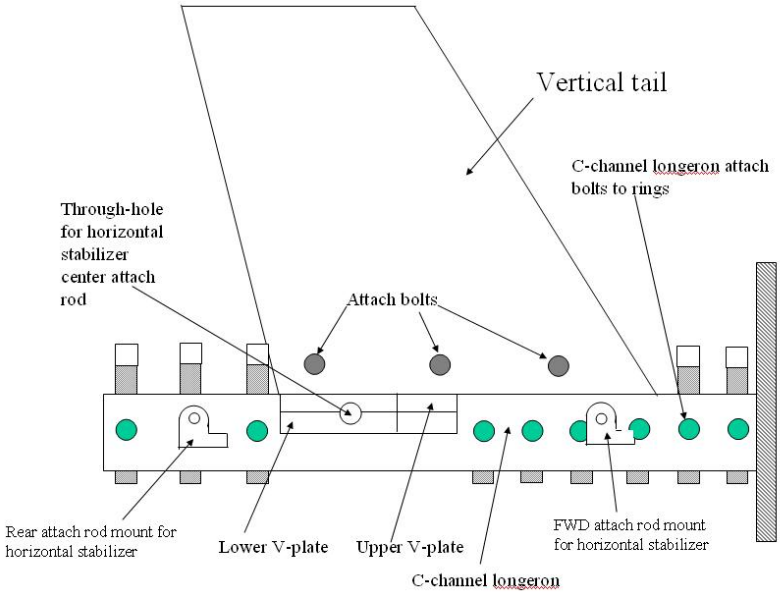

Figure 25: F/A-18 wind tunnel model empennage design side view

Figure 26: F/A-18 wind tunnel model empennage and testing fixture

Table 5: Frequencies of F/A-18 vertical tail

Mode number	Actual F/A-18 Frequency (Hz)	Model Frequency (Hz)	Calculated Model frequencies (Hz)
1st Bending	16.73	30.57	31.29
1st Torsion	46.77	85.46	87.46

Results are displayed in Table 5. Initial characterization testing uses a 100 mV/g accelerometer at the free end of the elastic axis on the starboard tail. An impact hammer is used to excite the tail and the voltage from the sensor is sampled by a DSpace 1003 DSP. This response data is processed in Matlab. The response of the empennage is compared with the scaled frequencies in Table (5) and is shown to be 2.28% lower than the calculated value. Because this is such a small percentage of error the empennage is judged acceptable. The empennage is then installed onto the fuselage.

Figure 27: F/A-18 wind tunnel model empennage installation

In the first open loop testing, composite tails made of eleven lamina are used. This thickness is determined by finite element modeling to obtain the required scaled frequencies for this model. Thinner tails are constructed as experiments show that the current OPSAs do not have sufficient control authority for thee thicker tails. The OPSA actuators used in

Figure 28: Final F/A-18 wind tunnel model without OPSAs

this work were originally made for a 1/16 scale F-15 wind tunnel model. The tails on the F-15 model are four lamina thick so new F-18 tails with four lamina are constructed. Even though the new tails are not aeroelastically scaled they still stay within the goal of this thesis which is to experimentally control F/A-18 vertical tails in the presence of uncertainties.

From previous research[33] it is well known that when a composite structure has a delamination the bending frequency is reduced when the delamination is open (reduced stiffness) and returns to its original frequency when the delamination closes. This is a nonlinear behavior. Therefore, two additional tails are constructed; one tail with no delaminations and a second tail with a 30% delamination of the span centered on the span on the elastic axis and goes 100% chord in length.

Once this new empennage is installed on the model, the response is characterized with the OPSAs installed. The overall experimental setup is illustrated in Figure 29. Six OPSAs are installed at the base of the tail (three on each side). Figure 30 shows an OPSA with a piezostack installed. For these experiments, six Polytec PI P-810.10 stacks are used. These stacks produce up to 50N of blocked force with a maximum voltage of 100 V. The accelerometer sensor (100 mV/g) on the elastic axis of the vertical tail is connected to

a signal conditioner. In turn, the output of the signal conditioner is connected to a low pass filter digital (A/D) channel of the Quanser system. The mode of interest in these experiments is the first bending mode which is 14.4 Hz. A low pass filter is used for anti-aliasing and is set to 50 Hz to allow observation of the modes adjacent to the first mode for spillover during the closed loop. A random excitation is generated by a Siglab 2042 device. The excitation signal is routed to a low pass filter before being connected to the DSP system and connected to the piezo-amplifier. In the characterization experiment, a sampling frequency of 1000Hz is used. Time domain data is taken for one minute. In the FFT analysis, a window width of 512 is used. The first natural frequency is found to be 13.834Hz (See Figure 31).

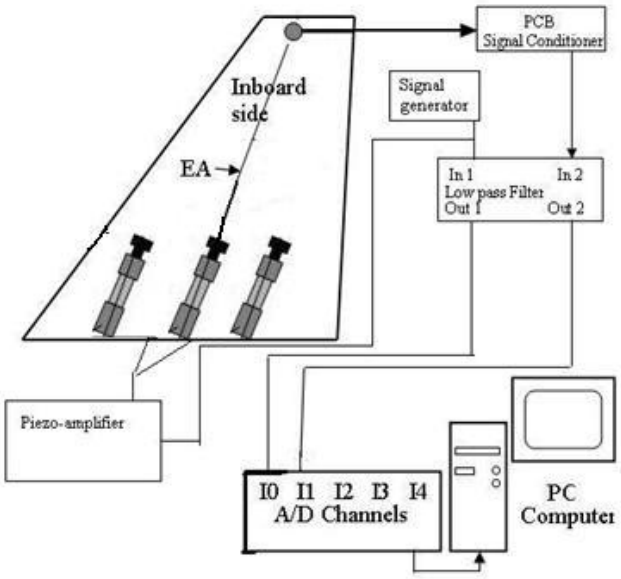

Figure 29: Experiment to characterize model tail

Once the fully bonded tail has been characterized, a plant model is synthesized. Even though the focus of this work is to control the first bending mode, a plant model with higher modes is obtained using the Frequency Domain System Identification Matlab Toolbox[1]. This is done to allow the observation of any spillover effect on the higher modes when controlling the first mode. Using this toolbox, a 10th order plant model is created which is used for simulation of the controllers before going to the wind tunnel.

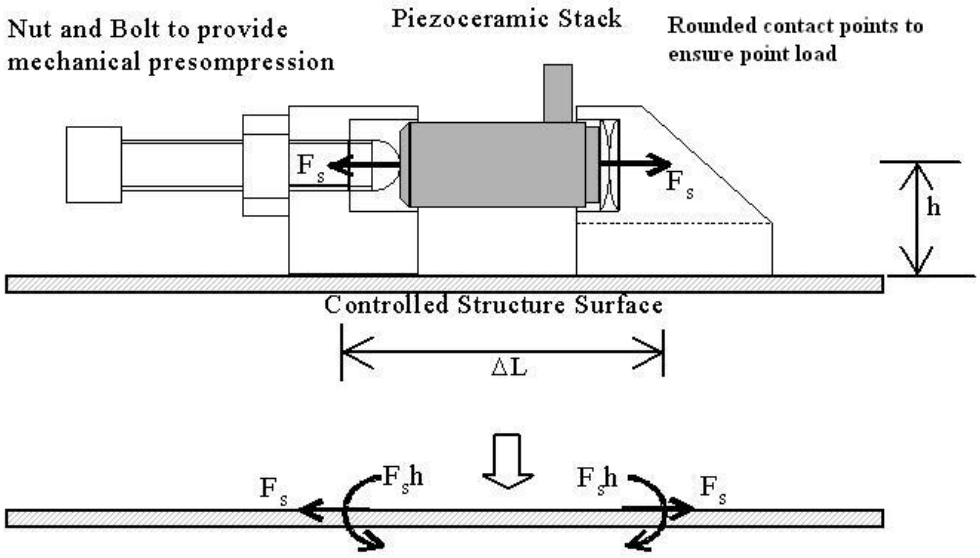

Figure 30: Offset piezoceramic stack actuator

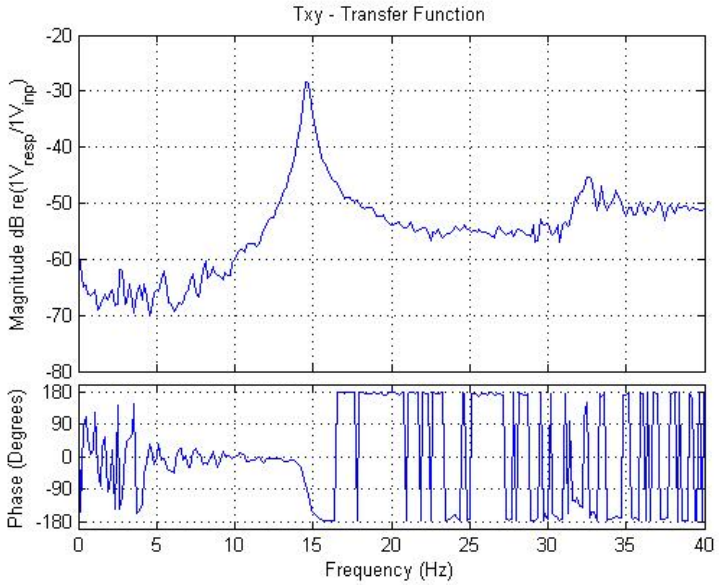

Figure 31: Frequency response function of F-18 thin, fully bonded tail

4.4.2 Test plan

The wind tunnel experiments were conducted in four phases as follows.

Phase I Model Validation

Phase II Open loop characterization of the plant in the wind tunnel

Phase III Closed loop control using the linear controller

Phase IV Closed loop control using the linear controller and augmented adaptive neural network

These are discussed in the following sections.

4.4.3 Phase I: Model validation

The wind tunnel model is validated to determine if it can produce the correct flow field at the different test conditions. Specifically, this test validates that the proper vortex is created from the LEX and as angle of attack and q is increased the vortex bursts and causes tail buffet. The model is mounted on the side of the tunnel as shown in Figures (32) through (34).

In order to obtain the required flow visualization two types of tufts are used.

- Two inch tufts mounted with tape along the port wing leading edge, along the fuselage at the port wing root, and on the fuselage between the vertical tails.
- A single tuft on a long metal rod which is moved to locations around the model. The tuft on this rod is approximately six inches long and has been marked with a red marker in a segmented fashion to help visualize the flow.

The test conditions are shown in Table (6). These values are set within the safe limits of the tunnel.

The testing clearly shows a well-defined vortex starting at the LEX at 20 degrees angle of attack and 5 psf. As the angle of attack increases, the vortex interaction with the vertical tails causes the vertical tails to vibrate and the burst point of the vortex moves forward and

Figure 32: F/A-18 wind tunnel model mounting structure, angle of attack 35 degrees

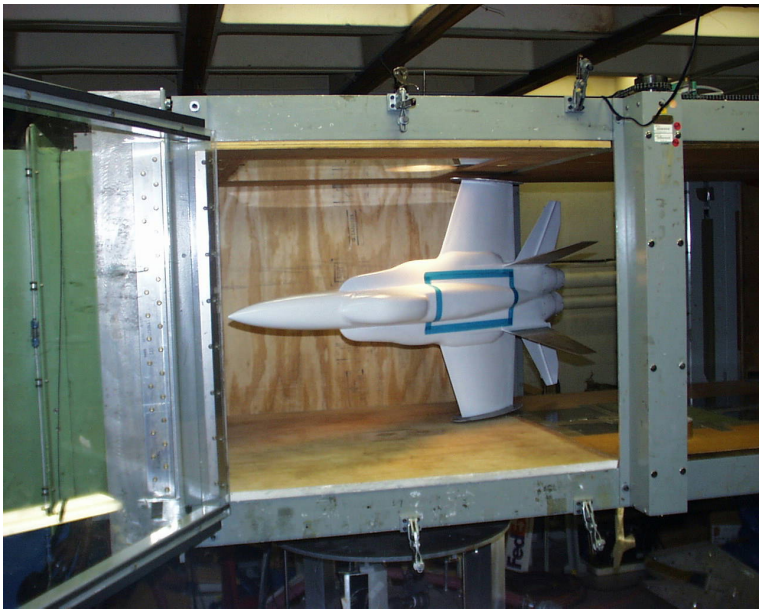

Figure 33: F/A-18 wind tunnel model mounted at 35 degrees angle of attack

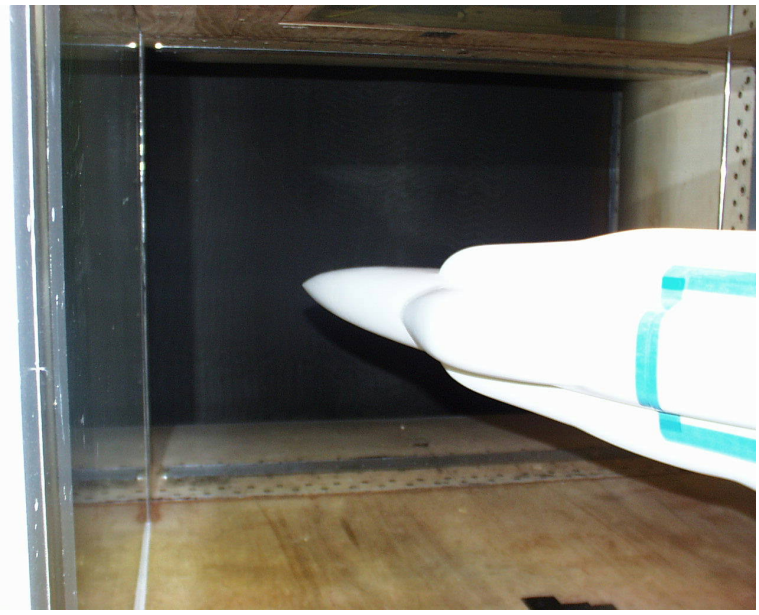

Figure 34: F/A-18 wind tunnel model mounted at 35 degrees angle of attack showing nose clearance

Table 6: Phase I testing configuration

Angle of attack (degrees)	Dynamic pressure (q) psf
0	5
0	12
20	5
20	12
25	12
30	5
30	9
30	12
30	15
32	12
35	12

ahead of the vertical tails. Movies of each test are made which includes narrative. These movies clearly show the vortex interaction with the fuselage and the vertical tails.

4.4.4 Phase II: Open loop first mode frequency characterization of the tail in the wind tunnel

In this phase, the worst case buffet conditions in the open loop configuration are identified. This confirms the worst-case buffet condition and helps to determine the amount of control authority the control scheme needs. This phase measures the open loop response of the vertical tail when the angle of attack is set to 0 degrees and the q is varied from 1 to 15 psf in increments of 2 psf. The frequency shift of the first bending mode as the airspeed is increases is characterized. The equipment that is used during the wind tunnel tests included:

- 1 PCB 352-A24 accelerometer with a PCB 480-D06 Signal Conditioners
- 1 Krohn-Hite Model 3343 Analog Filter Unit (anti-aliasing filter).
- 1 Pentium based PC for controller design and data post processing. The software used is Wincon 5.0 server/client and Quanser Q4 I/O board is used. This system uses Matlab 6 for control and processing.

Figure (37) shows the frequency shift as dynamic pressure increases. As the dynamic pressure begins to increase the first natural frequency shifts to 15.66 Hz at 3 psf, then 17.64 at 5 psf. However, at higher values of dynamic pressure the frequency shift levels off. To explain the probable cause of this anomaly tunnel blockage must be considered. Because this model is very large for this wind tunnel blockage could cause the local airspeed to stagnate at particular speed in the empennage area as it is aft of the fuselage. The wind tunnel pitot tube that measures dynamic pressure is forward of the model. The model is not instrumented with pressure ports to record the actual dynamic pressure on any of its surfaces. This phase is successful as it did show that the first natural frequency shifts as dynamic pressure increases. Figure(36) shows that this phase is successful in showing that the worst case buffet condition occurred at 32 degrees angle of attack.

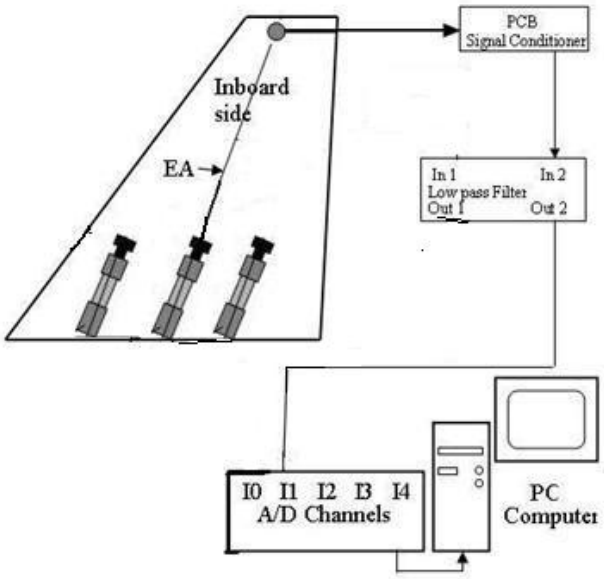

Figure 35: Experimental setup for open loop response in the GTRI wind tunnel

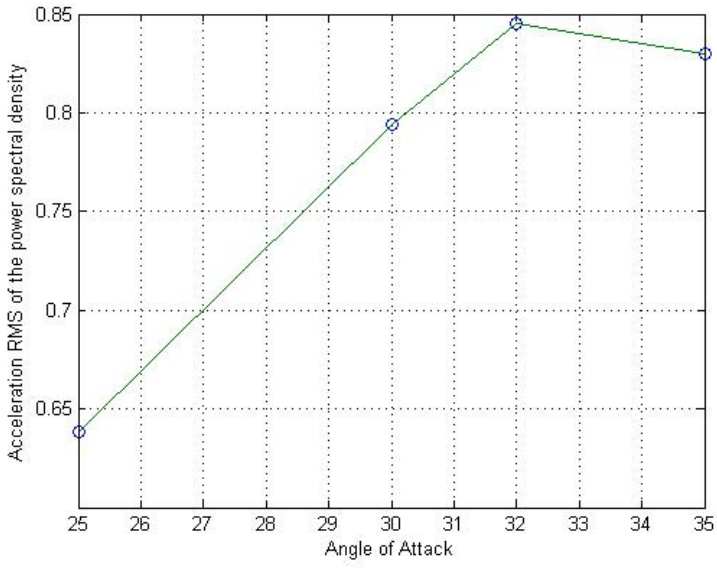

Figure 36: RMS acceleration as F-18 wind tunnel model angle of attack increases

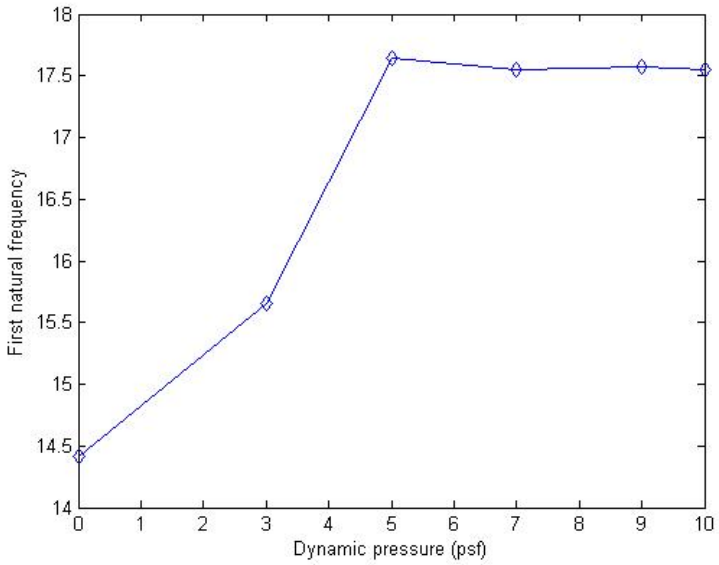

Figure 37: Frequency shift of F-18 vertical tail as wind tunnel dynamic pressure increases

Table 7: Plant parameters

Parameter	Value	Description
ω_p	16.73 - 25 Hz	The first bending frequency
ζ_p	1.5%	Damping ratio
ρ_{steel}	7850 $\frac{kg}{m^3}$	Density of the plant material

4.4.4.1 Modeling first mode of F-18 model tail using linear controller at worst case buffet condition

Because this phase acquires open loop data at the wind tunnel worst case buffet condition of 32 degrees AOA at 12 psf, a single degree of freedom model is used to demonstrate the effects of parameter shift. To demonstrate the effect of frequency shifts, equation (26) is used to model a single degree of freedom tail system and a linear acceleration feedback controller is designed to reduce the vibrations (Figure 38).

In this model, the control moment is induced from a set of six piezoceramic stacks. In the model the control force only produces a positive force. The linear acceleration feedback controller with a crossover design[31] gain γ is determined using equation (42). This model uses the parameters listed in Tables (7), (8), and (9).

The plant is excited with a harmonic force at the same natural frequency as the plant

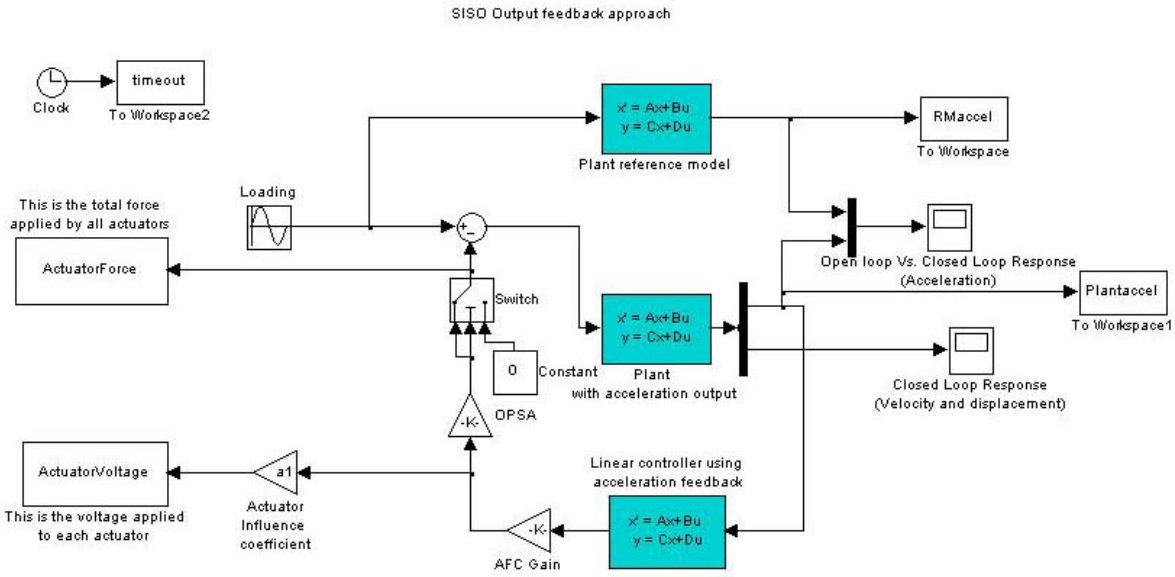

Figure 38: tail model using a linear acceleration feedback controller

Table 8: Linear control system parameters

Parameter	Value	Description
ω_c	16.73 Hz	Frequency of the linear controller
ζ_c	2.88%	Damping ratio of the linear controller
γ	0.1	Controller gain

Table 9: Actuator and sensor parameters

Parameter	Value	Description
a_1	$5.55 \times 10^{-5} m$	Influence coefficient of the actuator
b	0.387 m	Influence coefficient of the sensor
d_{33}	$6.35 \times 10^{-10} \frac{m}{V}$	Piezoelectric charge constant
t_{layer}	120×10^{-6} m	Thickness of each piezoceramic layer
Y_s^E	55.25×10^9 GPa	Modulus of elasticity
c	0.02 m	Stack length
A_s	$25 \times 10^{-6} m^2$	Cross sectional area of a stack

(16.73 Hz) with an amplitude of 0.003 V. This amplitude makes the plant acceleration response approximately the same amplitude as the open loop wind tunnel test at 32 degrees angle of attack, 12 psf. The model is run with plant first natural frequencies of 16.73, 19, 21, 23, and 25 Hz or frequency ratios of 1.0, 1.14, 1.21, 1.37, and 1.49. These values are chosen to ensure enough crossover divergence to clearly show the drop in control effectiveness of the linear controller. Figures (39) through (48) show the reduced control effectiveness of the linear controller in the time domain and power spectral density. Figures (39) through

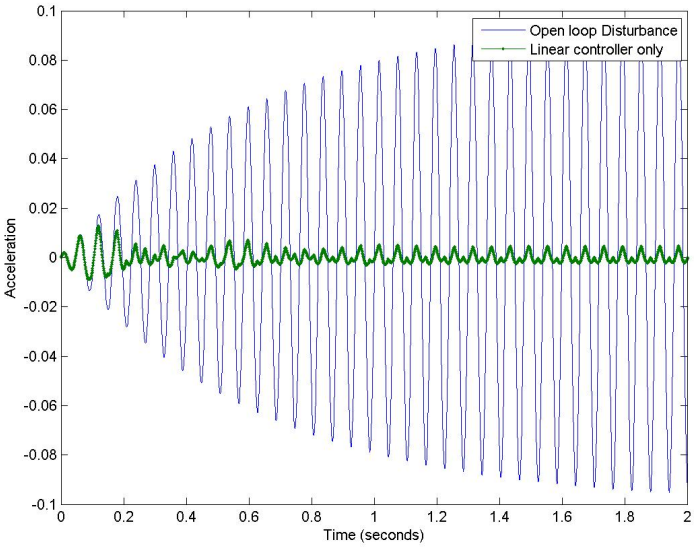

Figure 39: Simulation of measured acceleration of tail model using a linear acceleration feedback controller with a plant to controller frequency ratio of 1.0

(48) show that as the first natural bending frequency deviates from the crossover condition the control authority is reduced. The fact that the effectiveness of the linear controller is reduced as the shift increases is an expected condition, however, how ineffective the linear controller would be as the plant diverges from the crossover condition is not understood. If the first natural frequency shifts within 15% of the nominal condition the effectiveness of the linear controller decreases significantly. Shifting of more than 15% will produces a significant reduction in linear controller effectiveness. Figure (49) shows a steep decline in control authority as the frequency shift increases above 15%. At almost 50% shift the linear controller is less than 55% effective in controlling the first mode. This shows that for

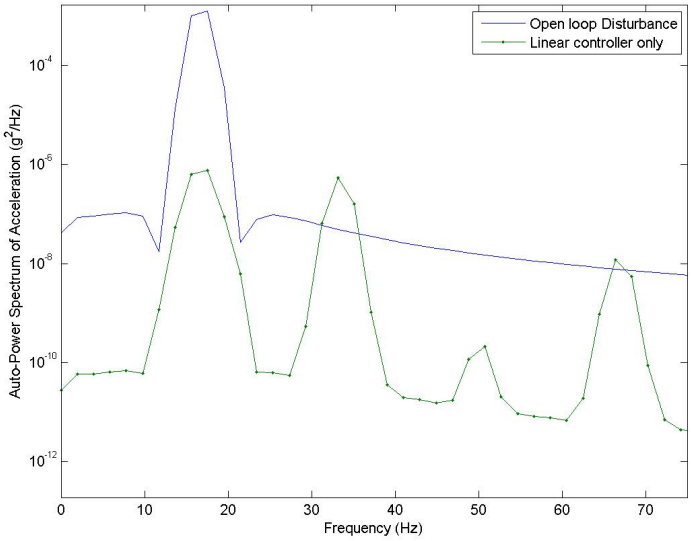

Figure 40: Simulated power spectral density of acceleration of tail model using a linear acceleration feedback controller with a plant to controller frequency ratio of 1.0

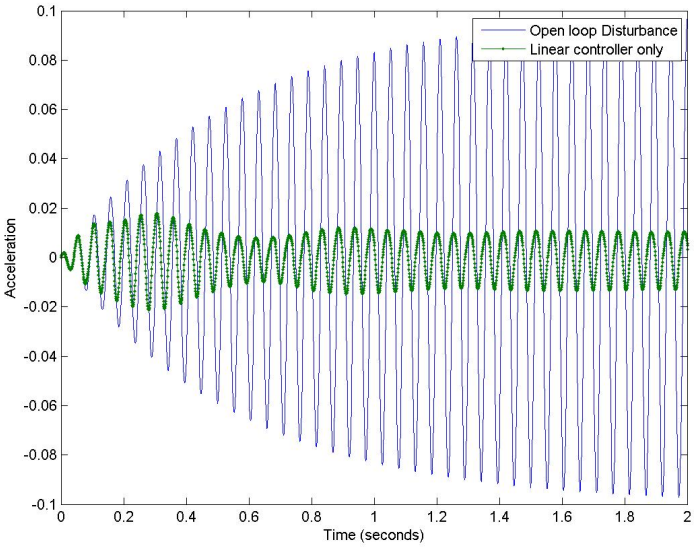

Figure 41: Simulation of measured acceleration of tail model using a linear acceleration feedback controller with a plant to controller frequency ratio of 1.14

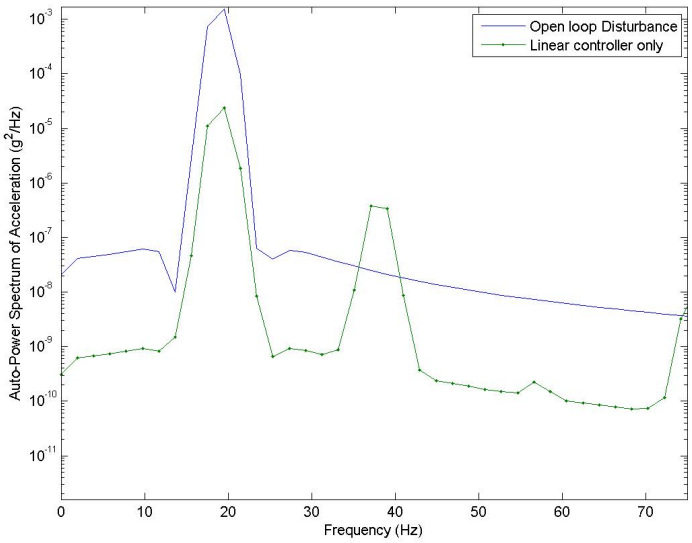

Figure 42: Simulated power spectral density of acceleration of tail model using a linear acceleration feedback controller with a plant to controller frequency ratio of 1.14

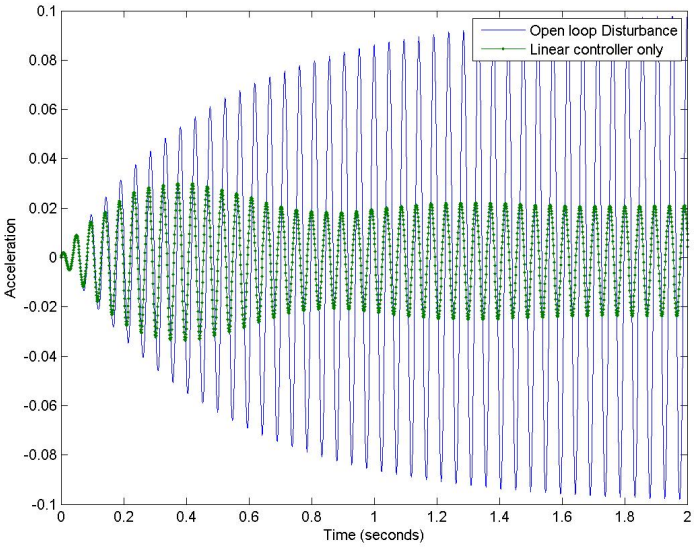

Figure 43: Simulation of measured acceleration of tail model using a linear acceleration feedback controller with a plant to controller frequency ratio of 1.21

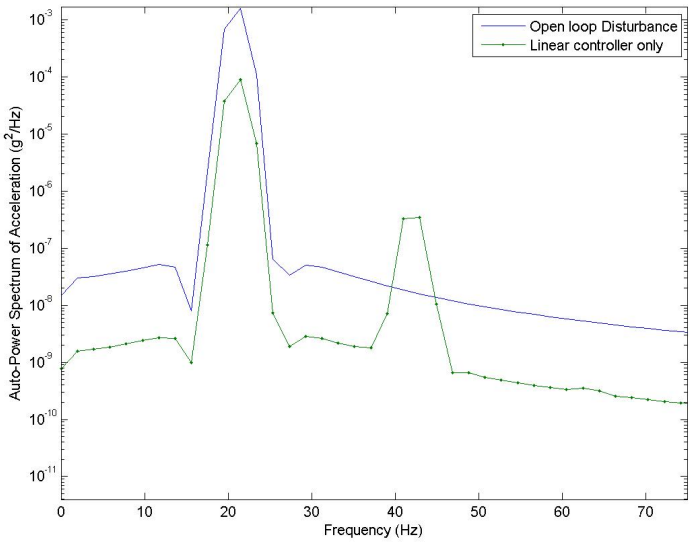

Figure 44: Simulated power spectral density of acceleration of tail model using a linear acceleration feedback controller with a plant to controller frequency ratio of 1.21

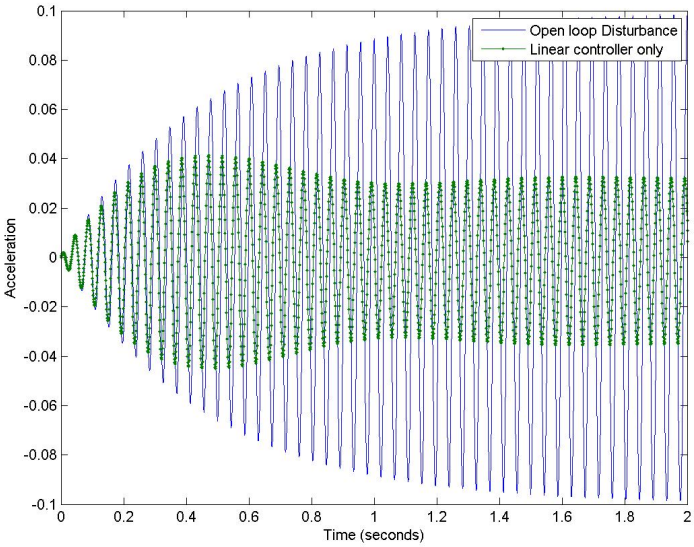

Figure 45: Simulation of measured acceleration of tail model using a linear acceleration feedback controller with a plant to controller frequency ratio of 1.37

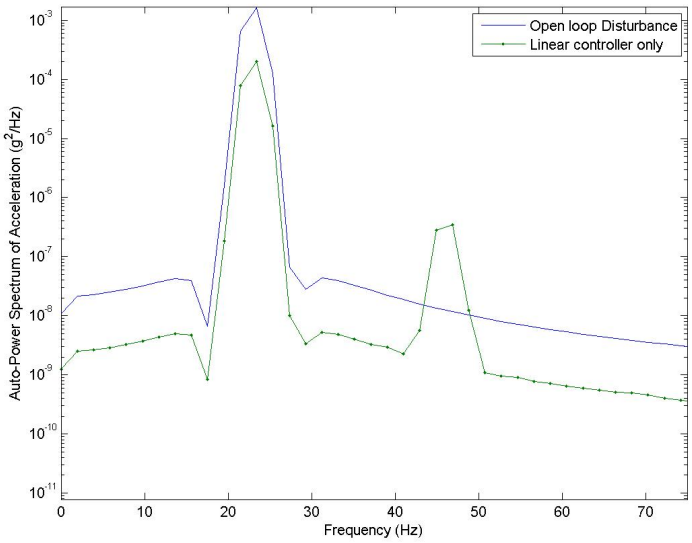

Figure 46: Simulated power spectral density of acceleration of tail model using a linear acceleration feedback controller with a plant to controller frequency ratio of 1.37

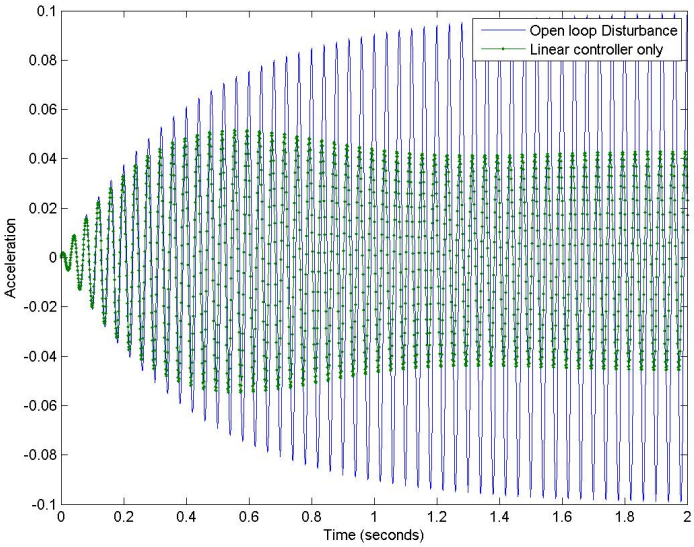

Figure 47: Simulation of measured acceleration of tail model using a linear acceleration feedback controller with a plant to controller frequency ratio of 1.49

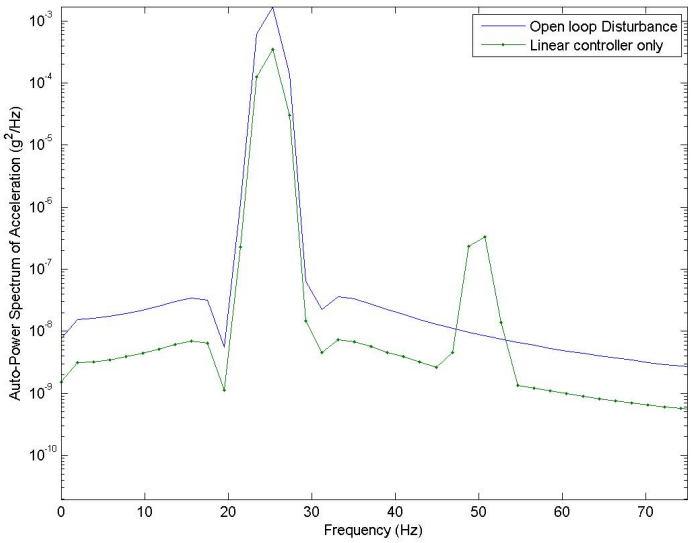

Figure 48: Simulated power spectral density of acceleration of tail model using a linear acceleration feedback controller with a plant to controller frequency ratio of 1.49

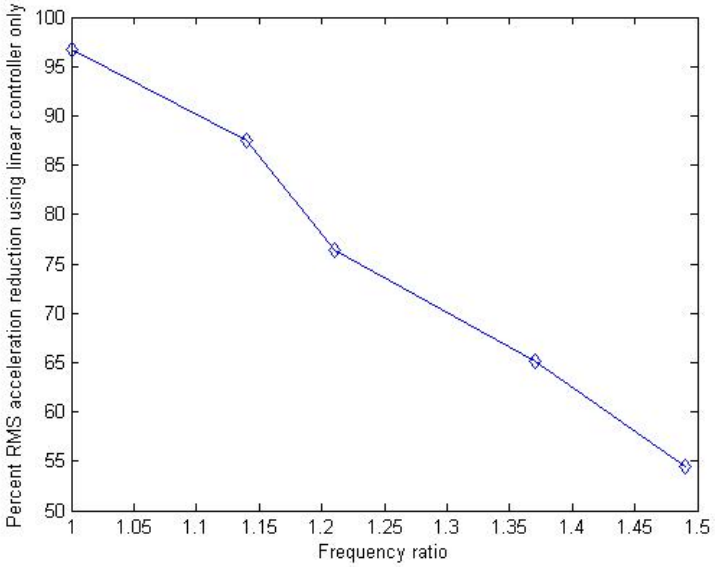

Figure 49: Percent of RMS acceleration reduction using linear control in tail model as frequency ratio increases

a SDOF problem the RMS reduction has an almost linear relationship with the frequency ratio. For structures that can be simplified to a SDOF system that experiences frequency shifts, a frequency ratio band could be determined that is within the fatigue life of the structure. Outside of this ratio band the linear controller would need to be augmented with an adaptive element to control the uncertainties. These results show that a frequency shift of more than 15% can possibly reduce the fatigue life of the vertical tail below the design life.

4.4.5 Phase III: Closed loop control using the linear controller

In this phase a linear controller is designed to control the first bending mode of the model F/A-18 vertical tail. The first step is to take the frequency response function from the plant characterization and create a plant model. The frequency response function is numerically fitted in a 10th order partial fraction expansion form. The single degree of freedom Nyquist circle fitting method is used to determine modal parameters for each mode.

The linear acceleration feedback controller is designed used crossover theory which means the controller frequency is the same as the mode that is controlled. The gain γ of the controller is the design parameter for this phase and is set to -750. This value is chosen to provide maximum structural damping while at the same time providing structural stability. Equation (42) is used to calculate the amount of controller damping. The total system damping is determined by adding the structural damping with the controller damping. With this value of gain, the damping is 90.3%. If much more gain is used in this design the closed loop poles would move to the right hand plane. The transfer function of the linear controller is

$$G_c = \frac{1.5737\text{x}10^7}{s^2 + 153.67\text{s} + 7868.5} \tag{108}$$

A graph showing the experimental frequency response function and the predicted damped first mode is shown in Figure (50).

To assess the stability of the linear controller with the experimentally determined 10th order plant derived earlier the SISO Tool in Matlab is used. A simple feedback loop is created in the Matlab SISO tool. The 10th order plant and the linear acceleration feedback

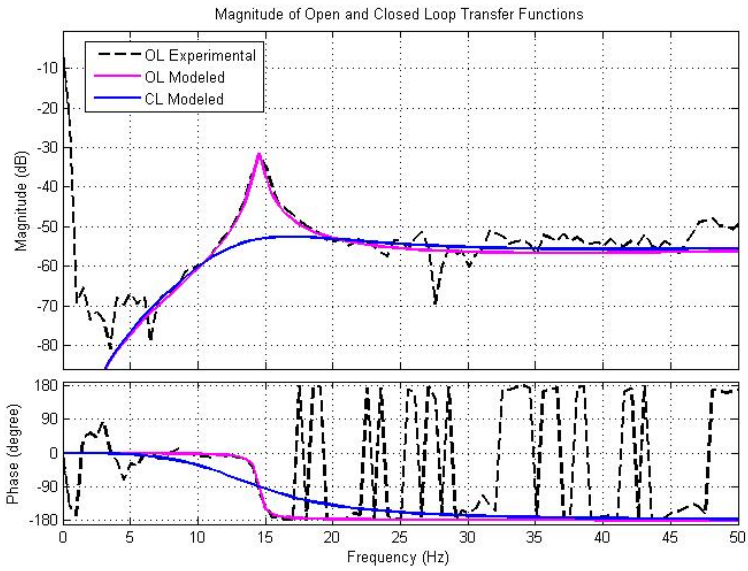

Figure 50: Experimental open loop and modeled closed loop system of the linear controller and thin bonded tail

controller transfer function are then imported into this feedback loop. The 10th order plant is placed in the plant block and the linear controller is placed in the feedback loop. The SISO Tool has a set of standard graphical tests (1) pole-zero map (2) step response (3)and impulse response. Figures 51 through 53 show the SISO tool tests which indicated that the linear controller/plant system will be stable when implemented. In Figure 51 all of the poles and zeros of the system are in the left hand plane. Figure 52 and 53 shows that when the system is disturbed by a step and impulse input respectively, the system dynamics will decay in a stable manner.

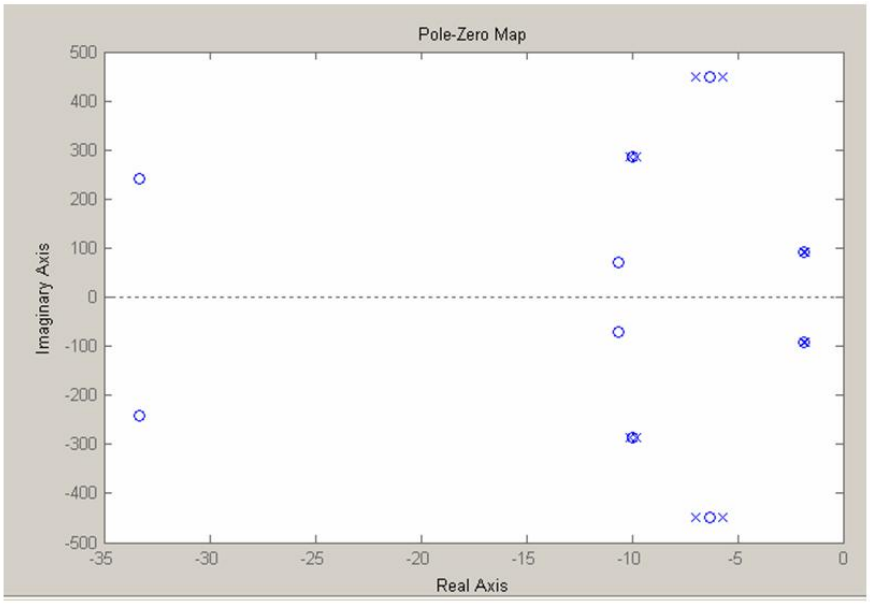

Figure 51: Pole-zero map of the closed loop system of the linear controller and thin bonded tail

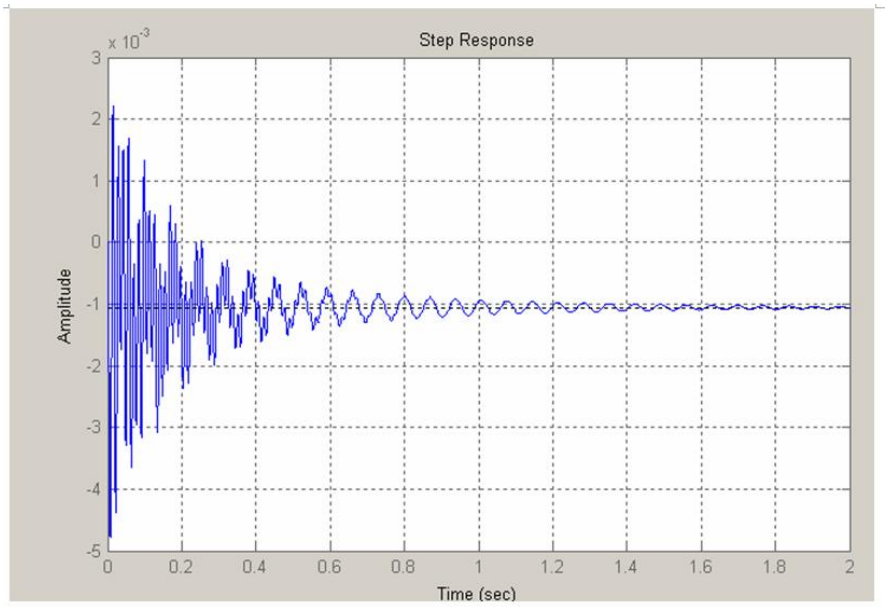

Figure 52: Step response of the closed loop system of the linear controller and bonded tail

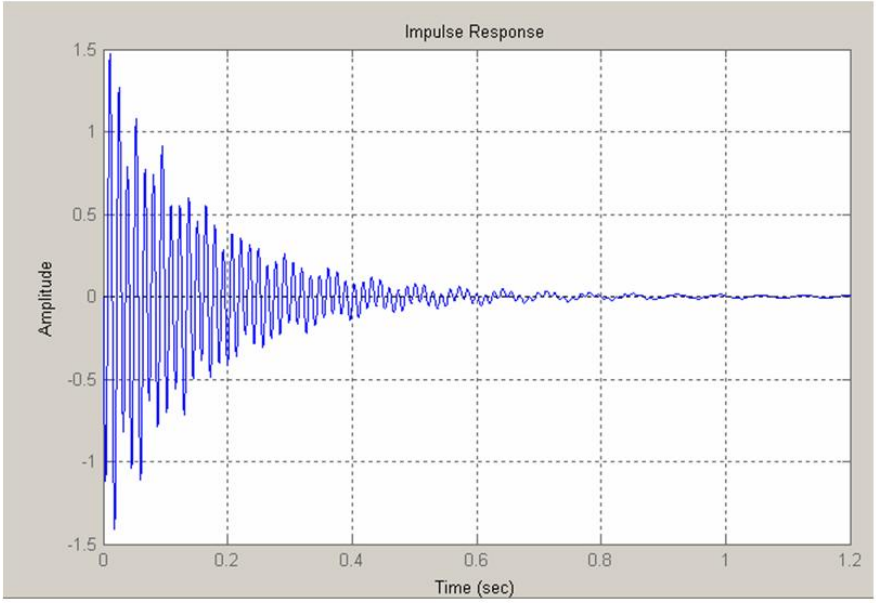

Figure 53: Impulse response of the closed loop system of the linear controller and bonded tail

4.4.6 Simulation of the linear controller

A Simulink simulation (Figure 54) is created to test reduction in RMS acceleration with this linear controller. Reduction of RMS acceleration is the key objective in all of these control experiments. In this simulation, a sinusoidal input at the same frequency as the controlled bending mode is used as the disturbance. The amplitude is adjusted until the open loop response amplitude is approximately the same as that observed in the open loop wind tunnel testing at the worst-case condition. The time domain response is recorded for one minute then the closed loop response is recorded for one minute. Upon comparing RMS acceleration between the open and closed loop it is observed that the linear controller had reduced the RMS acceleration by 26.23%.

A plant model with a shifted first mode is obtained by using the Matlab SISO Tool to modify the experimentally derived plant model by shifting the first mode up to 17.2 Hz. This is the same condition that is observed in the wind tunnel testing. When this modified plant is used in the closed loop system, the RMS acceleration is decreased by only 20.68%. Figure (55) shows the RMS acceleration reduction when comparing the open

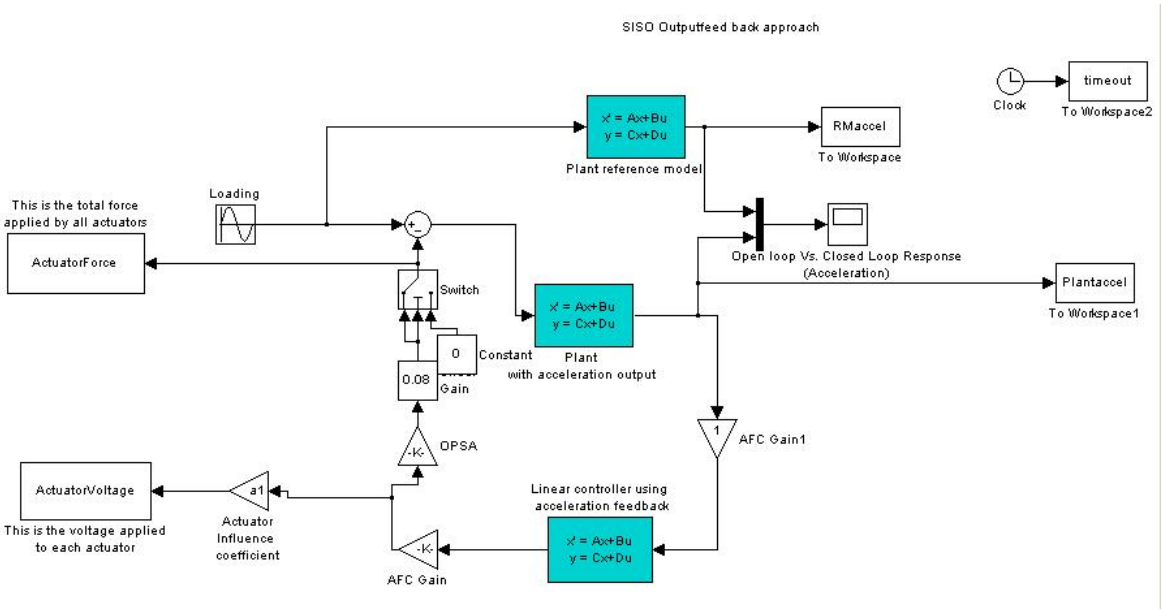

Figure 54: Simulation using linear controller only to control plant

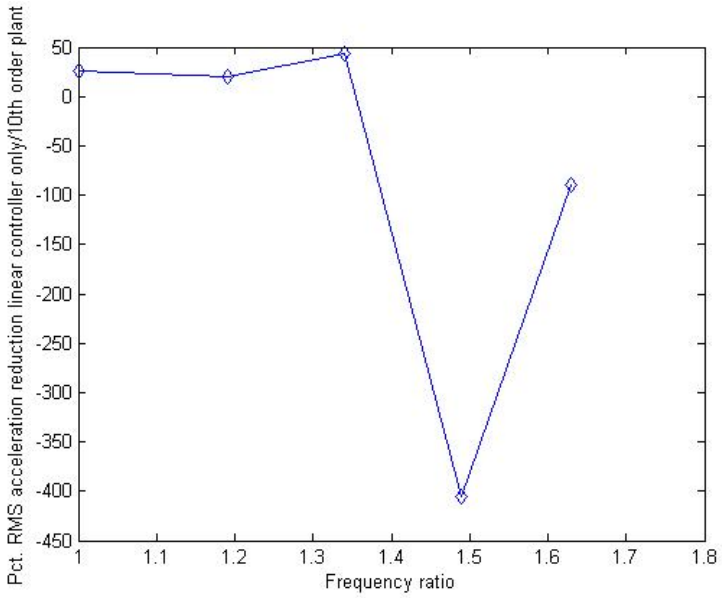

Figure 55: Percent of RMS acceleration reduction using linear control in 10th order tail model as frequency ratio increases

and closed loop using only the linear controller. This data does show a reduction in the linear controllers ability to reduce the RMS acceleration as the frequency shifts higher but does not show a almost linear relationship as is seen in Figure (49). The RMS acceleration reduction improves at a frequency ratio of 1.34. As this is not a harmonic and that the RMS acceleration reduction at frequency ratios of 1.49 and 1.63 vary substantially, the ability of the Matlab SISO tool to create an accurate modified plant model is suspect.

4.4.6.1 Air pulse testing of the linear controller

In this testing the vertical tail is attached to the empennage which, in turn, is attached to the F/A-18 model. One of the objectives of this test is to verify the controller can control the fist mode of the tail when mounted on a continuous system. This testing involves exciting the tail to the same amplitude of acceleration and displacement as observed in wind tunnel testing at the worst case buffet condition. Because the tail is a thin structure attaching a dynamic exciter would adversely alter the structural parameters of the tail. This leads to the second objective of this task which is to design and build a dynamic exciter that does not attach to the F/A-18 structure.

The first task is to design and fabricate the dynamic exciter. The dynamic exciter needed to excite the tail with as much similarity with the wind tunnel as can be manufactured. Because air in the wind tunnel excites the structure it is decided that the dynamic exciter should also use air to excite the tail. Acoustic exciters are hazardous and cannot excite the tail to wind tunnel levels. Fortunately, there is a shop air line in the lab. Shop air contains enough pressure to excite the tail at the wind tunnel levels and is a continuous flow of air. In order to pulse the air this air flow will have to pass through an oscillating valve. The concept of a wheel with drilled holes that the air can pass through and spinning at a prescribed rotational velocity will produce an air pulse device. The design shown in Figure (56) is the proposed device

During manufacture of this device it is determined the DC motor housing is not required. In order to vary the height of the device a car jack with a metal plate welded on top is used. The DC motor is driven by a linear DC amplifier and a voltmeter is installed to document

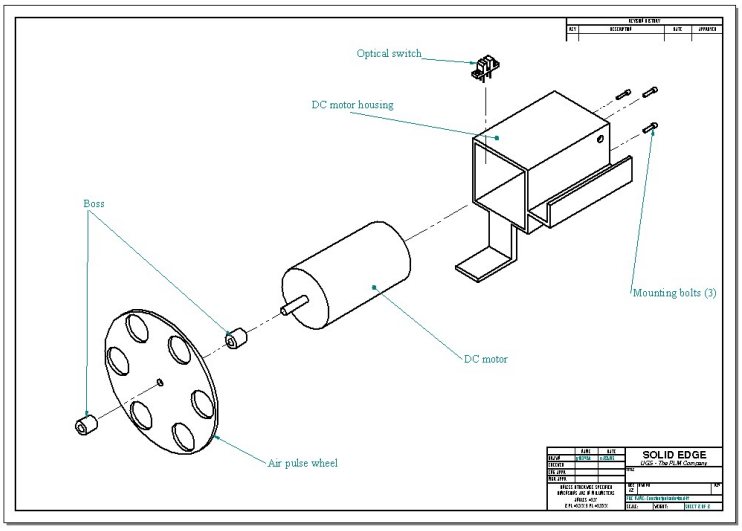

Figure 56: Air pulse device initial design

the exact voltage used to drive the system at a particular frequency (See Figures 57 and 58)

In the wind tunnel, tail buffet provides broadband energy into the tail. The air pulse is actually an air pulse generator and it is tuned to pulse at the first bending frequency. As a result, unlike buffeting, it puts a large amount of energy into a narrow band. The amplitude is adjusted until the level of response at this frequency is the same as that observed in the wind tunnel. With the second objective completed the first objective of controlling the tail can be accomplished.

The programming of the overall control experiment is achieved using Simulink (See Figure 59). The Quanser system installs additional Simulink blocks into Matlab for analog input and output. The linear and adaptive neural network controller blocks are taken from the Simulink models in the previous sections and are placed into this Simulink control system. The algorithm chosen for the time integration is a Runge-Kutta algorithm of order five. There is a manual switch block used to turn the neural network on or off. For the inboard and outboard OPSAs there is a manual switch for those as well. There is a constant block which is added to the input from the sensor to add any DC offset. Every branch in

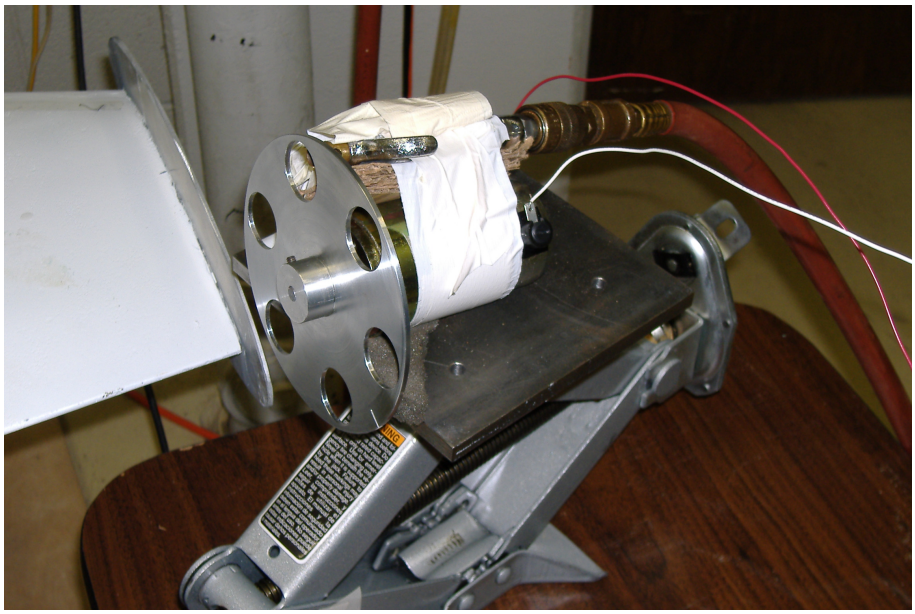

Figure 57: Air pulse device positioned next to F-18

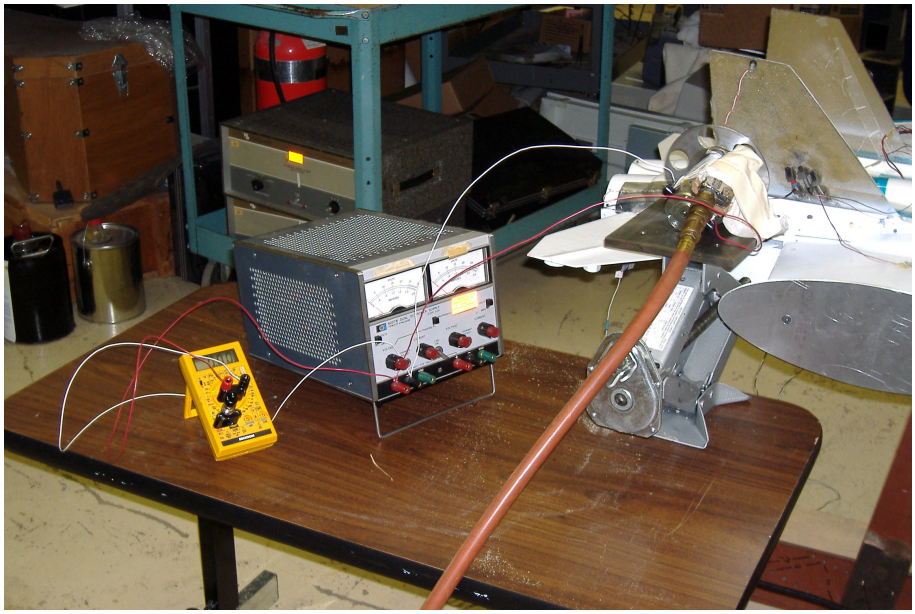

Figure 58: Air pulse system positioned next to F-18

Table 10: Phase III results of closed loop control of F-18 model vertical tail excited by air pulse device

Tail	Percent RMS acceleration reduction
Fully bonded	66.3%
Debonded	35.5%

this block set is monitored. Once the system starts, the controllers are engaged. Neural network weights were always monitored to verify convergence and stability. For testing of the linear controller only the manual switch for the neural network is turned off.

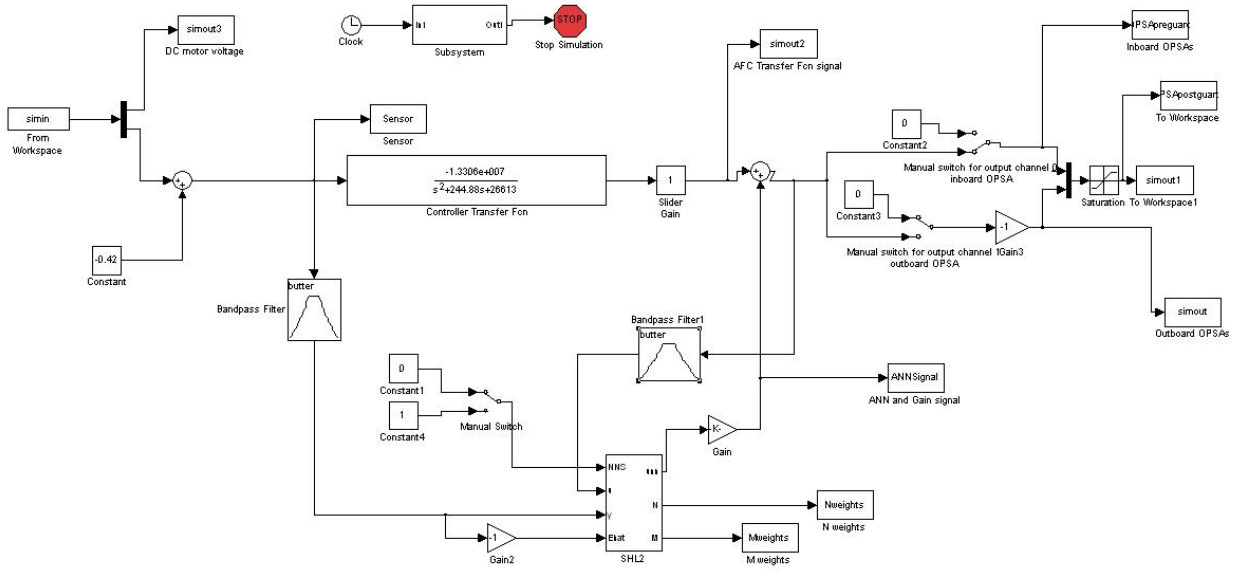

Figure 59: Simulink blockset to run control experiments

Results of the closed loop experiment with the fully bonded and debonded tail are shown in Table (10). As expected, when the frequency of the tail shifts because of the reduced stiffness due to the open delamination the system is no longer at the crossover condition the control effectiveness of the linear controller is reduced.

To ensure there is no voltage saturation anywhere in the system each electrical connection is monitored individually using an oscilloscope. The output of the control signal never exceeds 5V and the voltage to the other devices in the experiment never exceeds their design voltage of $\pm 10V$. In addition, the voltage to the stacks are always monitored and never exceed $50 \pm 50V$ which is within their 0-100V design voltage.

4.4.7 Phase IV: Active control of the vertical tails with an linear controller and augmented neural network

4.4.7.1 Closed loop simulation using the linear controller/adaptive neural network

To test the adaptive neural network a numerical analysis is first performed using the same model that is demonstrated in Phase II of this chapter. In this case the adaptive neural network is added. Figure 60 shows the constructed Simulink model. This particular adaptive controller design varies significantly from the one developed by Yang in that it does not use a reference model so the controller tracks $y_c^{(r)} = 0$. In addition, because of the higher frequency of the mode to be controlled the number of hidden layer nodes is increased to eight and additional time delays are added. Figure 60 shows that the inputs to the neural network are the control signal, the output, and the error dynamics which also comes from the output. The feedback loop involving the neural network has a gain of 15000. A reference open loop model is added in order to compare the effect of the linear controller augmented by the neural network with the open loop plant. The open loop model is not used in the control scheme. A harmonic load is applied to the plant with the same frequency as the first natural frequency of the plant.

The neural network uses the following learning gains.

- Γ_M: 0.5
- Γ_N: 0.5

The values of Γ_M and Γ_N are found by iteration until the best performance of the adaptive neural network is established.

Figures (61) through (75) clearly show that the adaptive neural network can suppress the first bending mode when the first natural frequency shifts. When the adaptive neural network is used to augment the linear controller the vibrations are immediately suppressed with very little settling time throughout the entire range of frequency ratios. Figure (76) shows that the RMS Neural Network Signal decreases as the frequency ratio increases. However, the PSD amplitude of the first mode in the closed loop is increasing as frequency ratio increases (Figure (77) though the closed loop amplitude is still very small compared

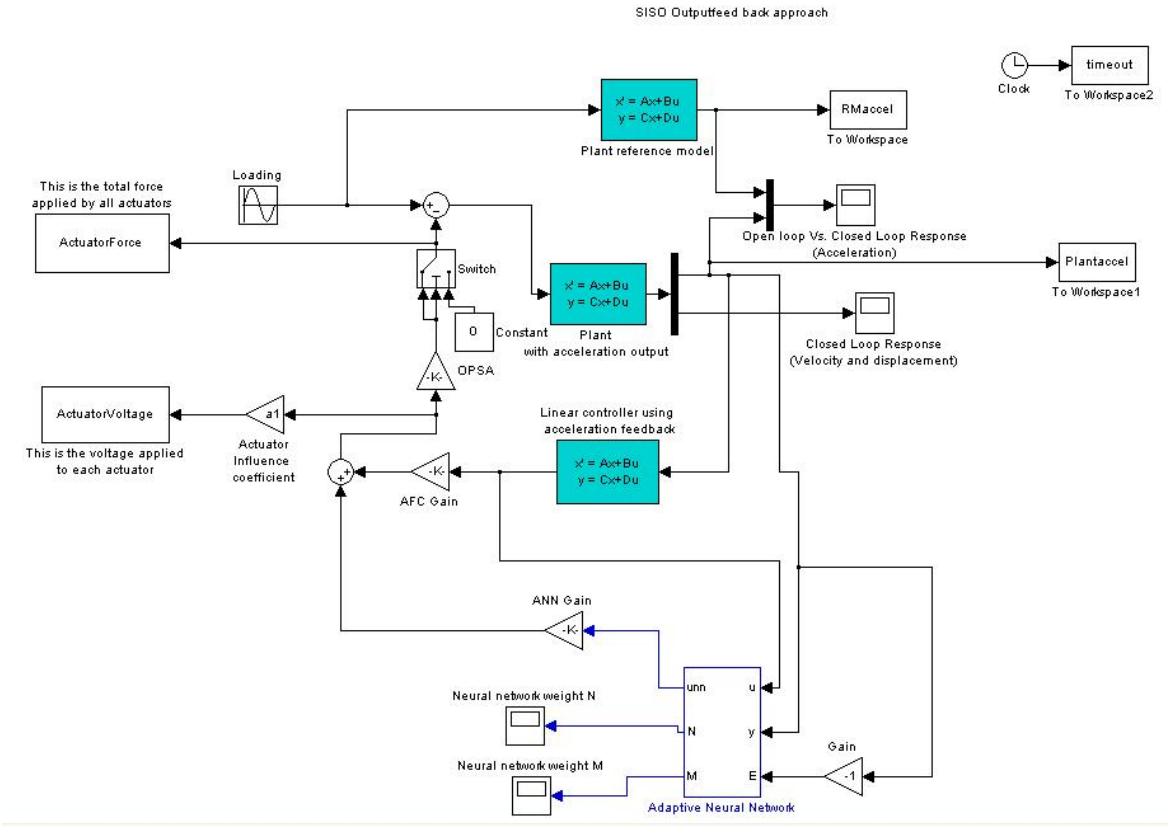

Figure 60: Numerical model of a linear acceleration feedback controller augmented by adaptive neural network

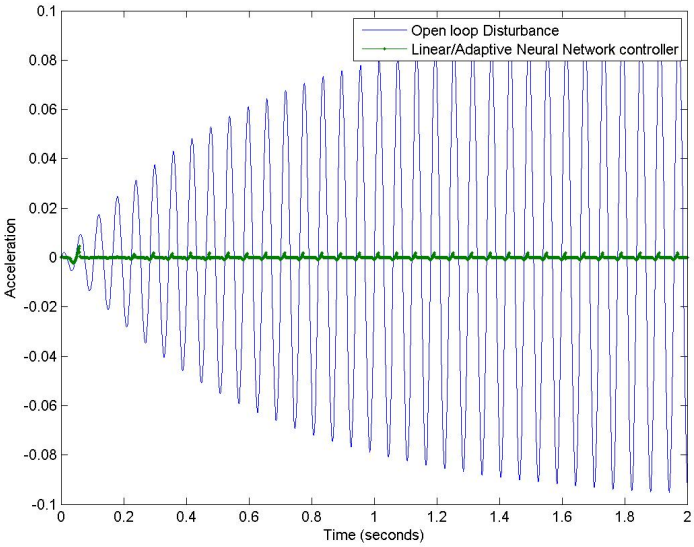

Figure 61: Simulation of measured acceleration of tail model using a linear acceleration feedback controller/augmented adaptive neural network with a plant to controller frequency ratio of 1.0

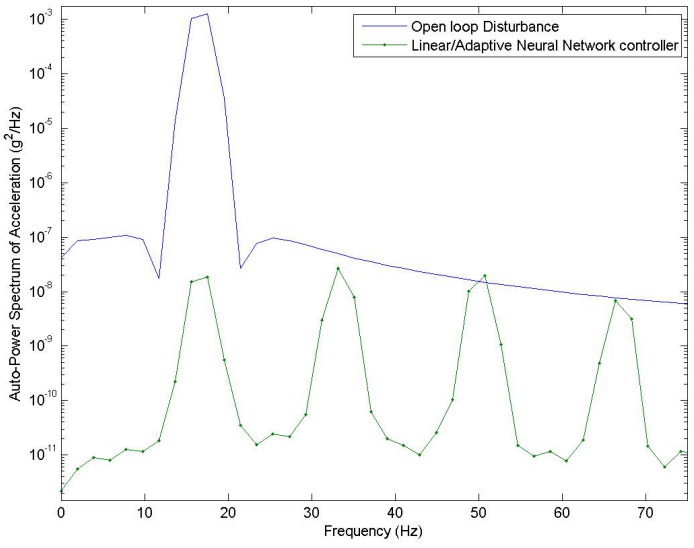

Figure 62: Simulated power spectral density of acceleration of tail model using a linear acceleration feedback controller/augmented adaptive neural network with a plant to controller frequency ratio of 1.0

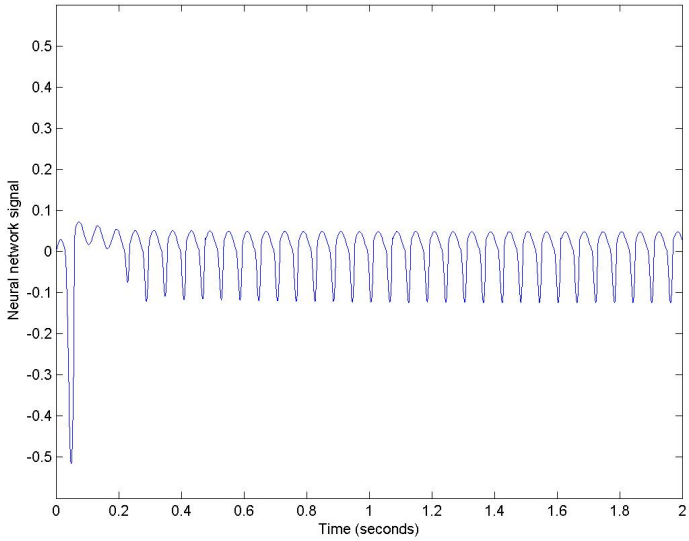

Figure 63: Simulation of measured adaptive neural network control signal u_{ad} of tail model using a linear acceleration feedback controller/augmented adaptive neural network with a plant to controller frequency ratio of 1.0

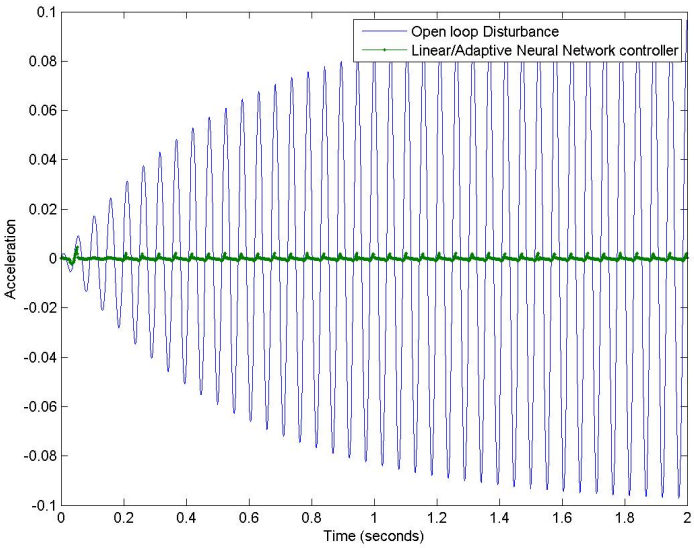

Figure 64: Simulation of measured acceleration of tail model using a linear acceleration feedback controller/augmented adaptive neural network with a plant to controller frequency ratio of 1.14

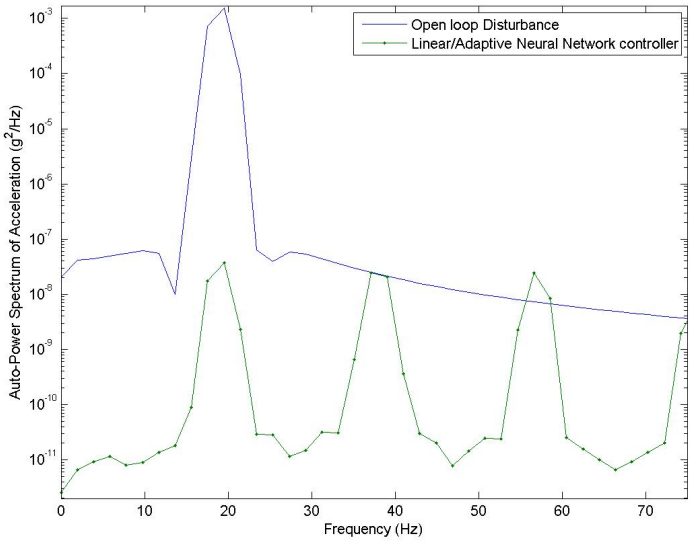

Figure 65: Simulated power spectral density of acceleration of tail model using a linear acceleration feedback controller/augmented adaptive neural network with a plant to controller frequency ratio of 1.14

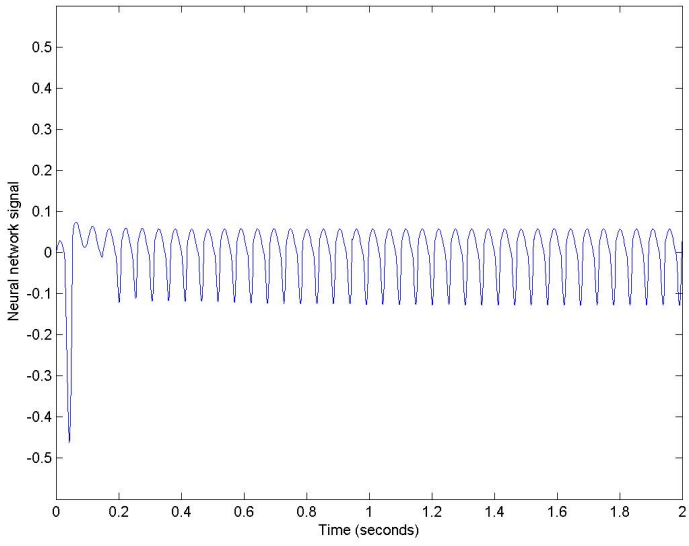

Figure 66: Simulation of measured adaptive neural network control signal u_{ad} of tail model using a linear acceleration feedback controller/augmented adaptive neural network with a plant to controller frequency ratio of 1.14

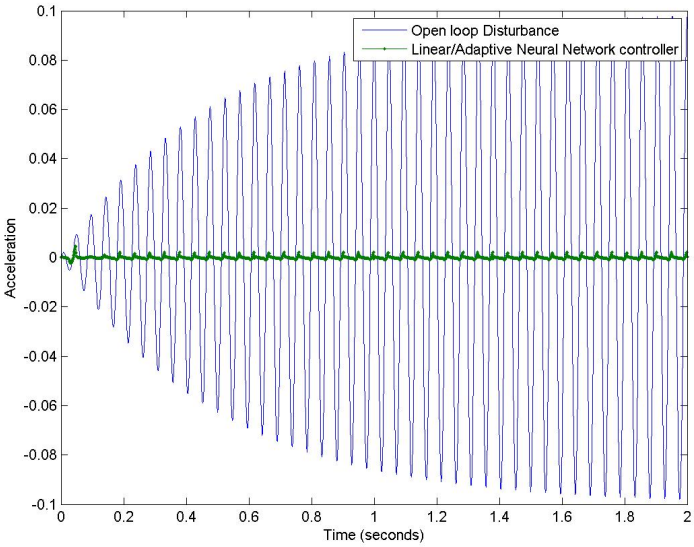

Figure 67: Simulation of measured acceleration of tail model using a linear acceleration feedback controller/augmented adaptive neural network with a plant to controller frequency ratio of 1.21

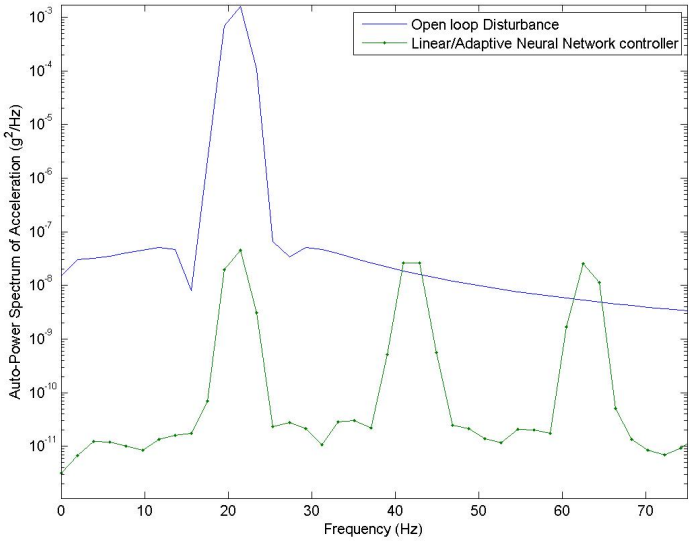

Figure 68: Simulated power spectral density of acceleration of tail model using a linear acceleration feedback controller/augmented adaptive neural network with a plant to controller frequency ratio of 1.21

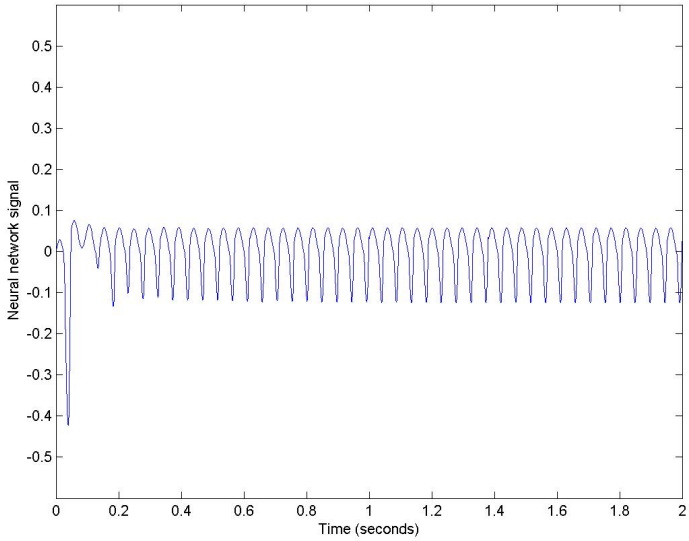

Figure 69: Simulation of measured adaptive neural network control signal u_{ad} of tail model using a linear acceleration feedback controller/augmented adaptive neural network with a plant to controller frequency ratio of 1.21

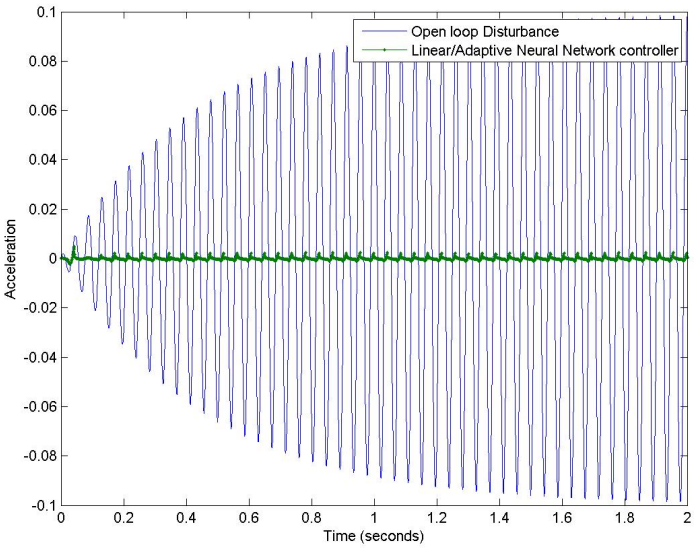

Figure 70: Simulation of measured acceleration of tail model using a linear acceleration feedback controller/augmented adaptive neural network with a plant to controller frequency ratio of 1.37

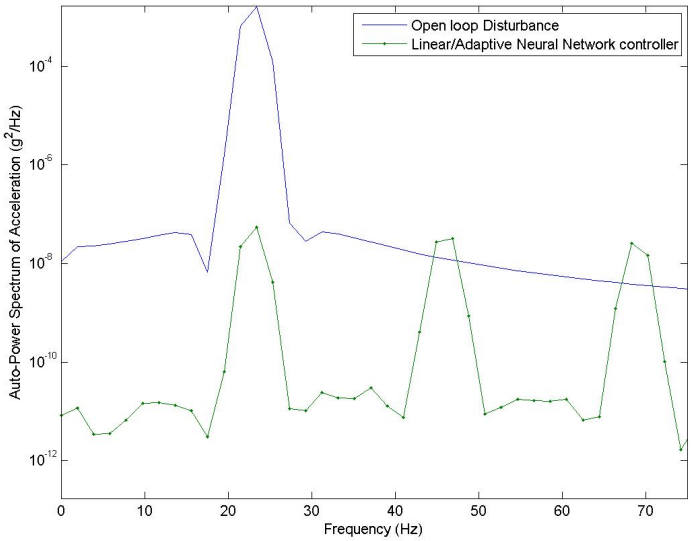

Figure 71: Simulated power spectral density of acceleration of tail model using a linear acceleration feedback controller/augmented adaptive neural network with a plant to controller frequency ratio of 1.37

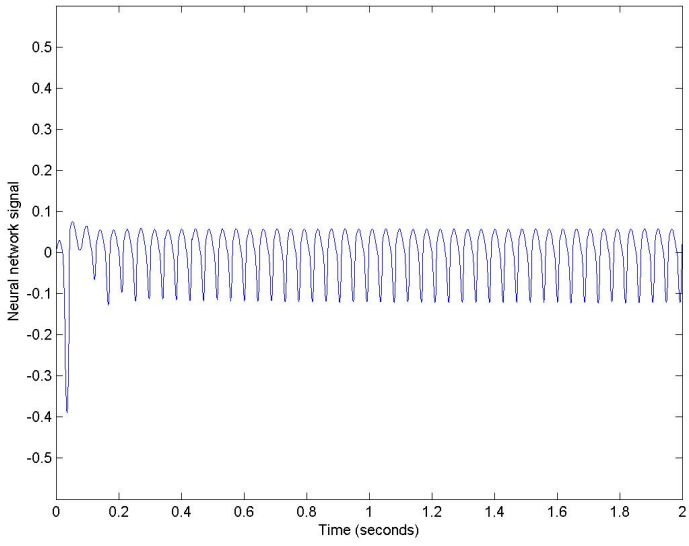

Figure 72: Simulation of measured adaptive neural network control signal u_{ad} of tail model using a linear acceleration feedback controller/augmented adaptive neural network with a plant to controller frequency ratio of 1.37

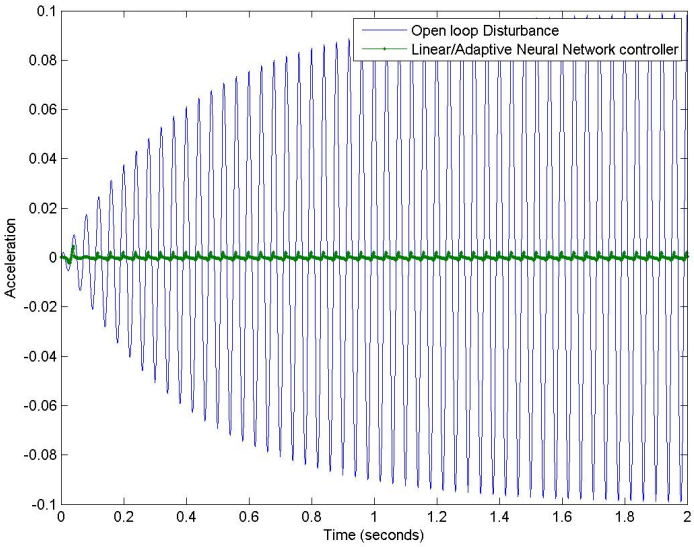

Figure 73: Simulation of measured acceleration of tail model using a linear acceleration feedback controller/augmented adaptive neural network with a plant to controller frequency ratio of 1.49

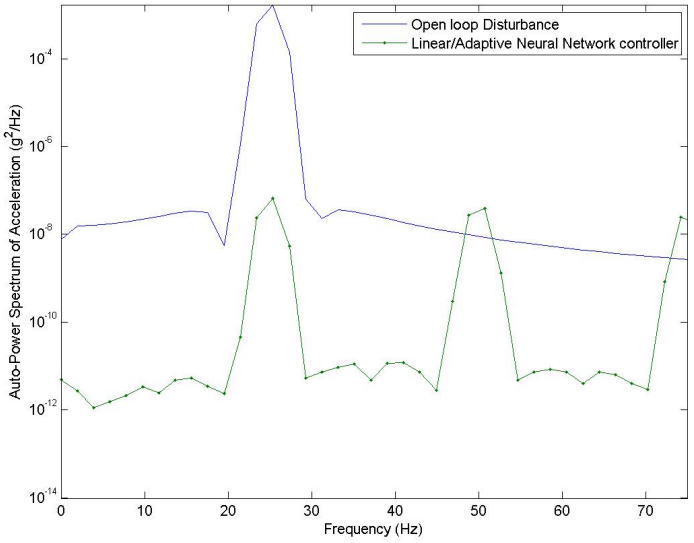

Figure 74: Simulated power spectral density of acceleration of tail model using a linear acceleration feedback controller/augmented adaptive neural network with a plant to controller frequency ratio of 1.49

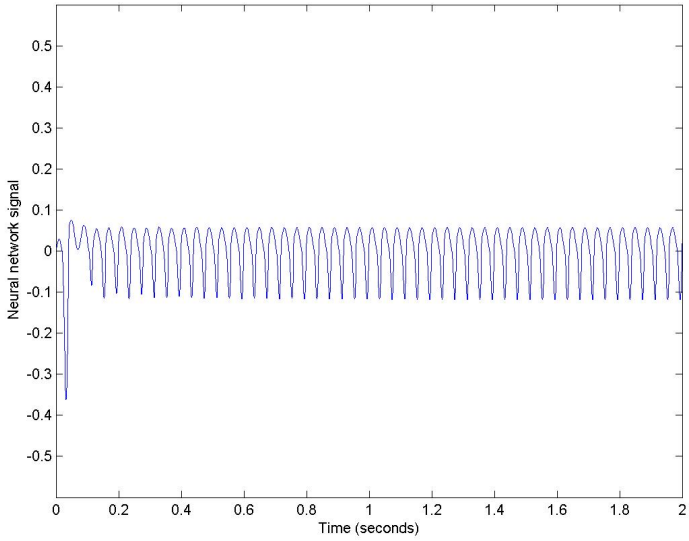

Figure 75: Simulation of measured adaptive neural network control signal u_{ad} of tail model using a linear acceleration feedback controller/augmented adaptive neural network with a plant to controller frequency ratio of 1.49

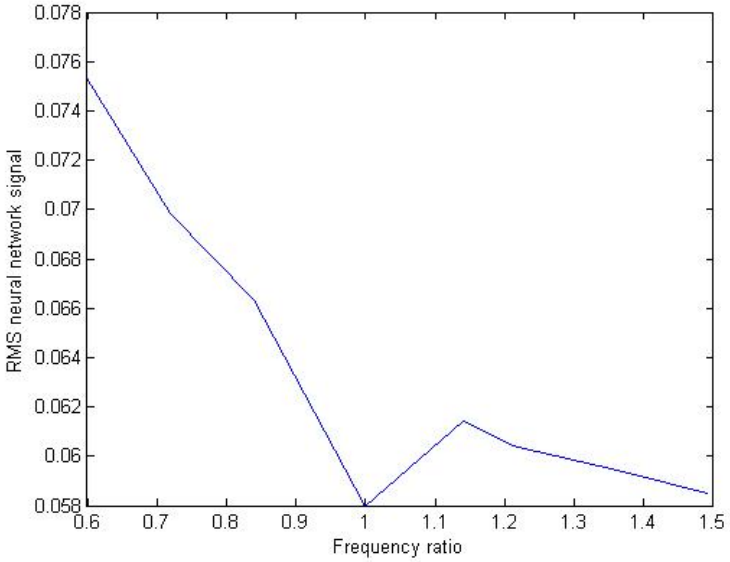

Figure 76: RMS Neural Network Signal as frequency ratio increases in simulation

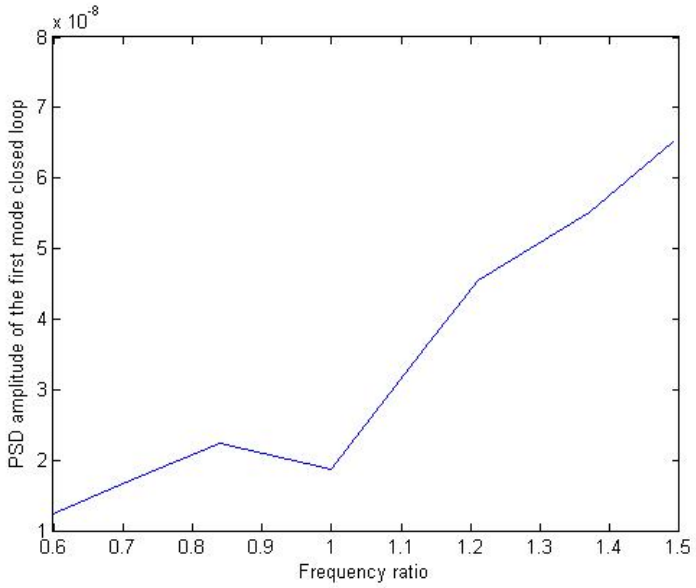

Figure 77: PSD amplitude of first mode closed loop linear/adaptive neural network controller as frequency ratio increases in simulation

to the open loop. As the frequency increases the neural network is observing the system with more information, thus, enabling the neural network to estimate the uncertainty with better accuracy. However, the control authority of the control system is still limited. This is observed as the frequency of the plant diverges from the nominal the control effectiveness decreases.

In the Simulink blockset that controls the experiments, the manual switch for the neural network is turned on. Because the neural network tries to reduce all the frequencies it observes a band pass filter is placed in the model. The filter also ensures the plant output to the neural network is relative degree 1. The range of this filter is 5 - 20 Hz. This range is set within the predicted value of the first mode as dynamic pressure increased. Neural network learning gain is set low (1) and the scaling of the input and output learning weights is set high (30). From trial and error with these values, the neural network is able to learn very quickly and learning weights are stable. A simulation is run using the original unmodified plant and the linear controller with the adaptive neural network. The RMS acceleration is now reduced by 32.16%. The modified plant is then placed in the simulation. The RMS acceleration reduction in this test is 26.9%.

Table 11: Comparison of simulated RMS reduction for linear controller only and augmented with a neural network

	Linear controller	Linear controller and neural network
Fully bonded tail	26.23%	32.16%
Debonded tail	20.68%	26.9%

As is shown in Table (11), there is additional reduction in RMS when the neural network is turned on especially when controlling the debonded tail. The debonded tail shifts between two states of stiffness. When the debond is open the stiffness of the tail is reduced along with the natural frequency. When the debond closes the stiffness rises as well as the natural frequency. The results in Table (11) clearly show that the linear controller has less control authority than the full bonded tail.

Now that the frequency shift in the wind tunnel has been characterized an additional numerical study is performed to observe the response of the adaptive neural network when the linear controller is using only half is designed gain (375). This study uses the same Simulink model as discussed earlier in this section with the 10th order plant.

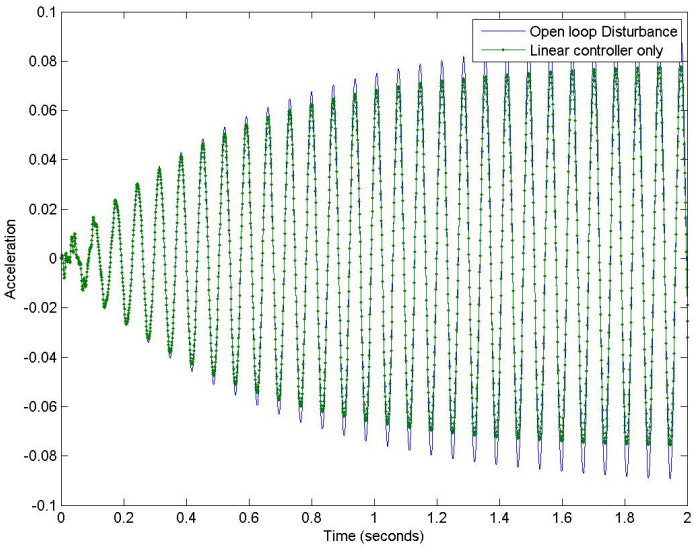

Figure 78: Simulated measured acceleration if tail model when controlled with the linear controller only at the crossover condition using half gain (375) at 32 degrees AOA, 12 psf

Figures (78) through (85) show in the time domain that as the frequency shifts the linear

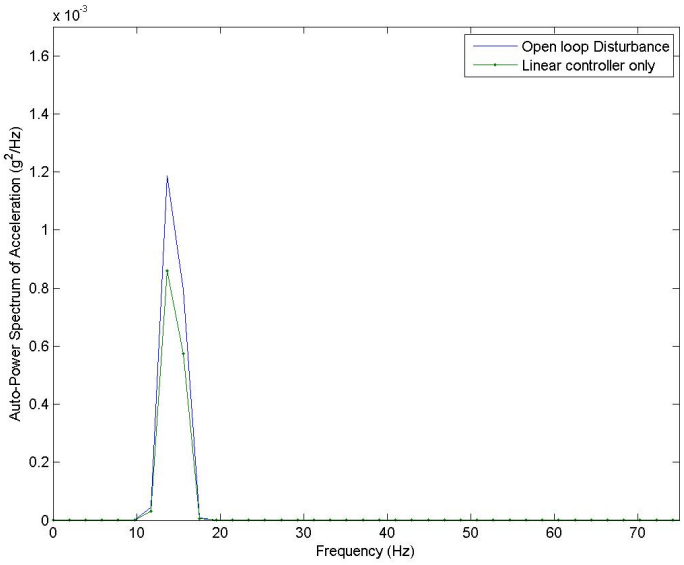

Figure 79: Simulated PSD acceleration if tail model when controlled with the linear controller only at the crossover condition using half gain (375) at 32 degrees AOA, 12 psf

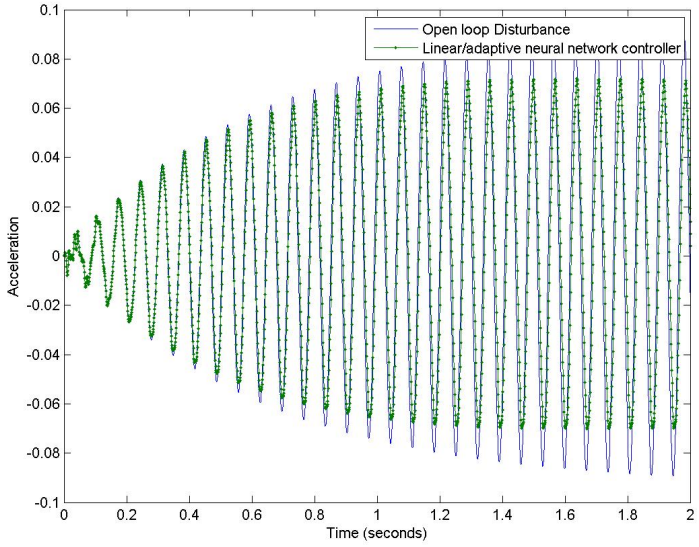

Figure 80: Simulated measured acceleration if tail model when controlled with the linear/adaptive neural network controller at the crossover condition using half gain (375) at 32 degrees AOA, 12 psf

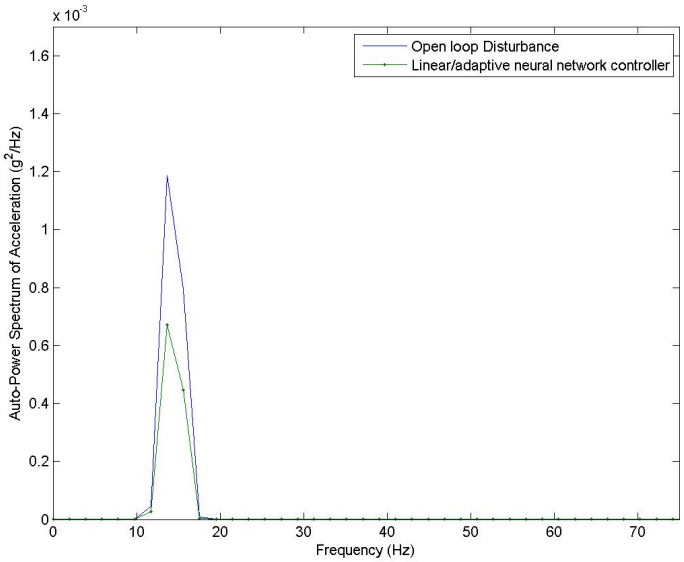

Figure 81: Simulated PSD acceleration if tail model when controlled with the linear/adaptive neural network controller at the crossover condition using half gain (375) at 32 degrees AOA, 12 psf

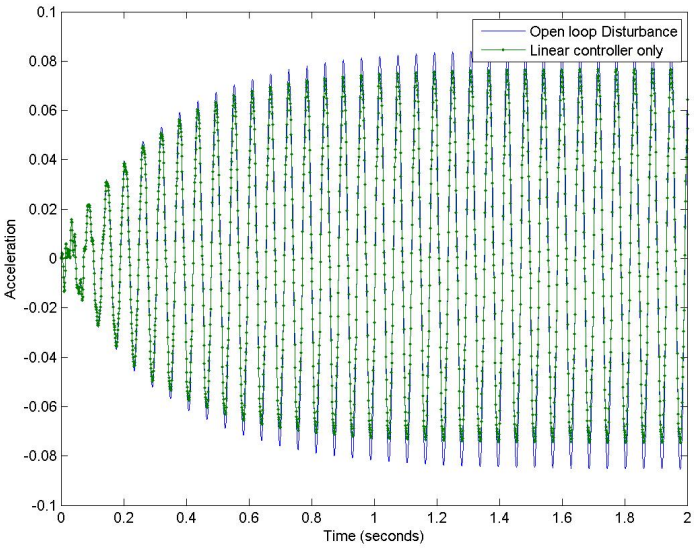

Figure 82: Simulated measured acceleration if tail model when controlled with the linear controller only with tail shifted frequency of 17.2 Hz using half gain (375) at 32 degrees AOA, 12 psf

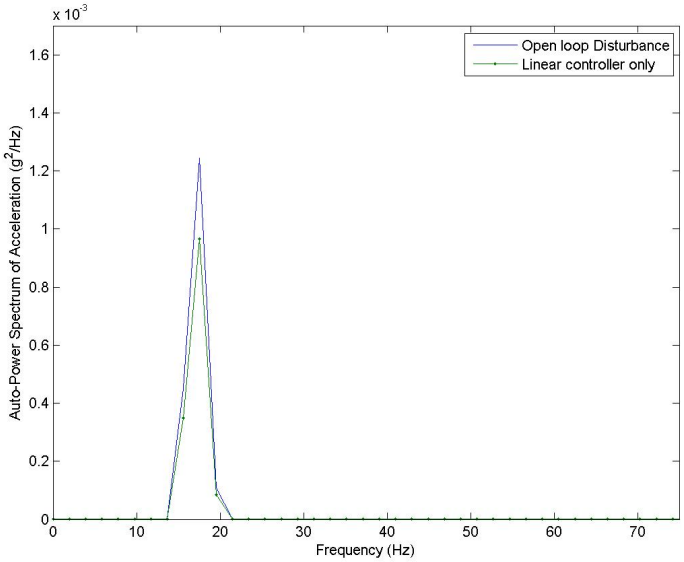

Figure 83: Simulated PSD acceleration if tail model when controlled with the linear controller only with tail shifted frequency of 17.2 Hz using half gain (375) at 32 degrees AOA, 12 psf

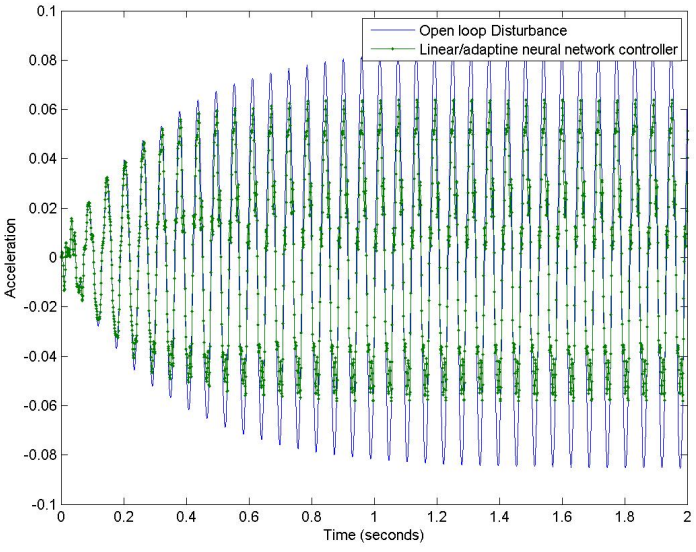

Figure 84: Simulated measured acceleration if tail model when controlled with the linear/adaptive neural network controller with tail shifted frequency of 17.2 Hz using half gain (375) at 32 degrees AOA, 12 psf

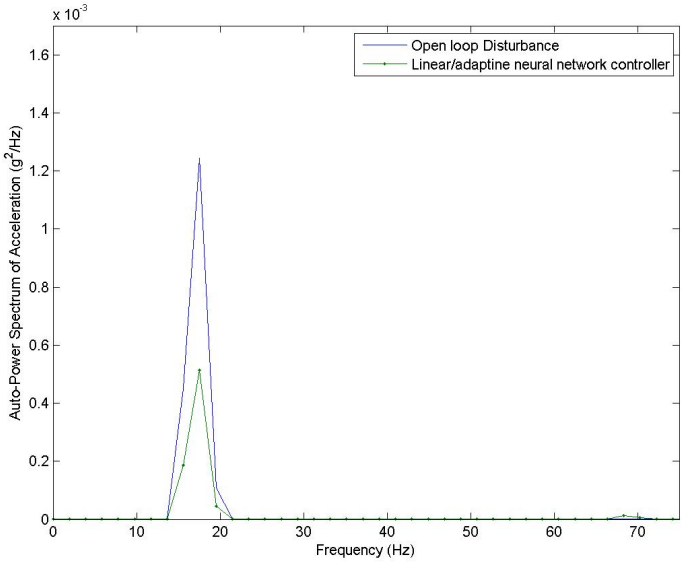

Figure 85: Simulated PSD acceleration if tail model when controlled with the linear/adaptive neural network controller with tail shifted frequency of 17.2 Hz using half gain (375) at 32 degrees AOA, 12 psf

Table 12: Comparison of simulated RMS reduction for linear controller only and augmented with a neural network when linear controller has only half of its design gain (375)

Plant frequency	Linear controller	Linear controller and neural network
14.41 Hz	14.94%	24.87%
17.2 Hz	11.69%	33.57%

controller becomes less effective. In Table (12) the RMS acceleration reduction decreases when the frequency shifts from the 14.42Hz of the undisturbed plant to 17.2 Hz which is approximately the frequency shift seen in the Phase II wind tunnel experiments. This is expected when using only the linear controller. The PSD acceleration at the first mode shows only a slight decrease and there are spillover effects. When the neural network is included in the closed loop the RMS reduction increases by as much as a factor of three.

When compared to the results in Table (11) where the gain of the linear controller is at 100% of design (750), the results in Table (12) show less RMS reduction when the gain of the linear controller is decreased. This is expected except for the condition where the plant frequency is 17.2 Hz and both the linear and neural network controller are in the closed loop. In this case the RMS reduction is improved when the linear controller gain is half of

the design gain. As the neural network adapts to changing conditions it is more efficient at controlling a non-crossover condition than the linear controller even if the frequency shift is a few Hz.

A second numerical study is performed to observe the response of the adaptive neural network when the linear controller is using twice its designed gain (1500). This study used the same Simulink model as discussed earlier in this section with the 10th order plant.

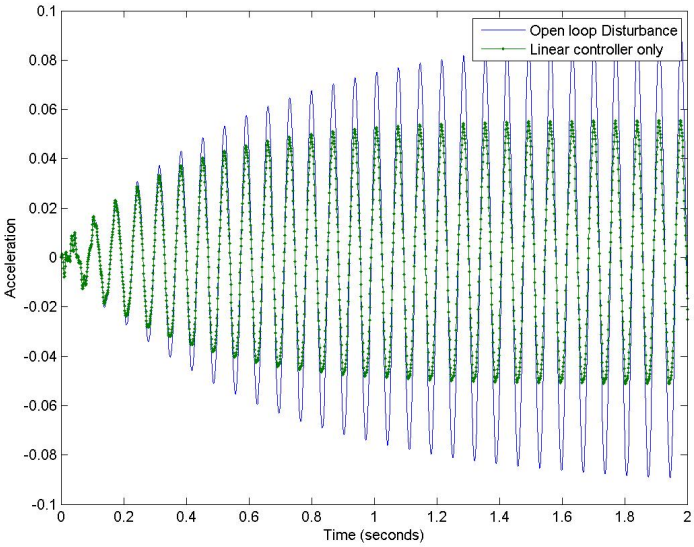

Figure 86: Simulated measured acceleration if tail model when controlled with the linear controller only at the crossover condition using twice the design gain (1500) at 32 degrees AOA, 12 psf

Figures (86) through (93) show that as the frequency shifts the linear controller becomes less effective. In Table (13) the RMS acceleration reduction decreases when the frequency shifts from the 14.42Hz of the undisturbed plant to 17.2 Hz which is approximately the frequency shift seen in the Phase II wind tunnel experiments. This is expected when using only the linear controller.

When compared to the results in Table (11) where the gain of the linear controller is at 100% of design (750) the results in Table (13) show more RMS reduction when the gain of the linear controller is increased. This is expected but it should be noted that the increase in RMS reduction is not twice as much as the design case. The cause of this could be plant

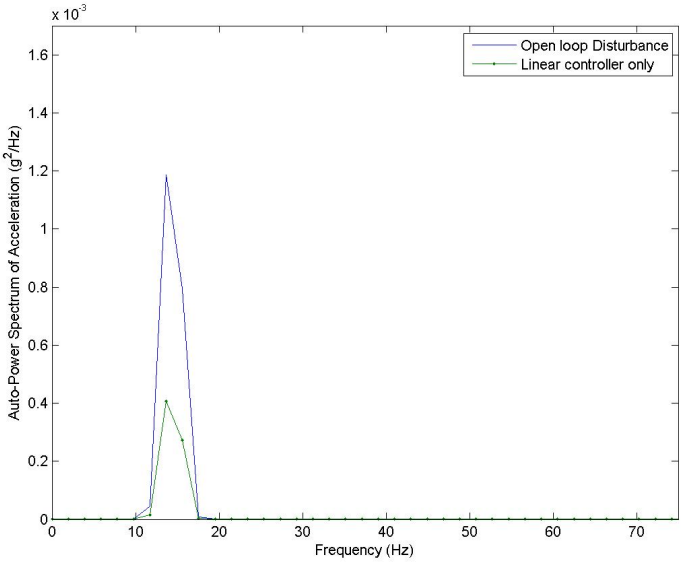

Figure 87: Simulated PSD acceleration if tail model when controlled with the linear controller only at the crossover condition using twice the design gain (1500) at 32 degrees AOA, 12 psf

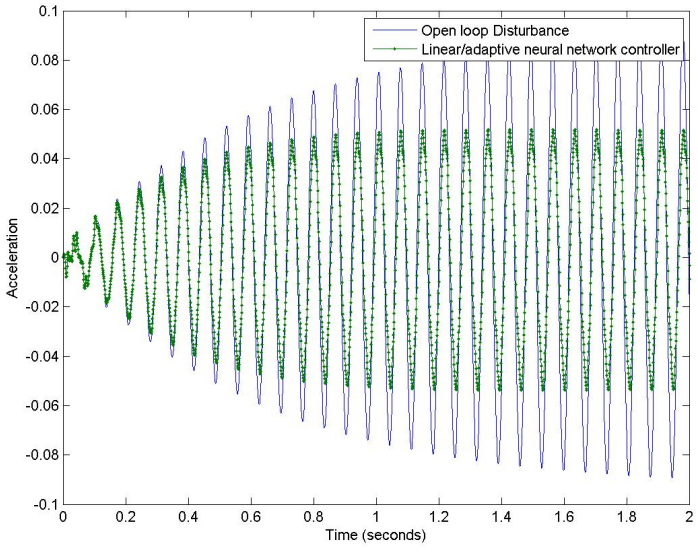

Figure 88: Simulated measured acceleration if tail model when controlled with the linear/adaptive neural network controller at the crossover condition using twice the design gain (1500) at 32 degrees AOA, 12 psf

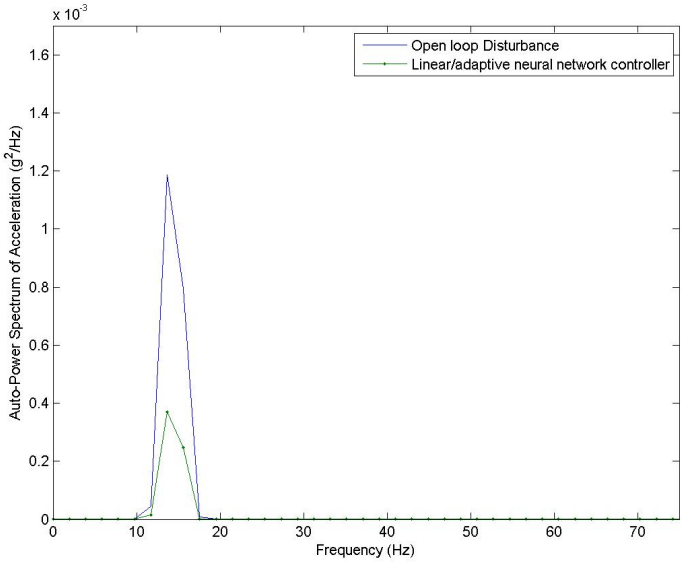

Figure 89: Simulated PSD acceleration if tail model when controlled with the linear/adaptive neural network controller at the crossover condition using twice the design gain (1500) at 32 degrees AOA, 12 psf

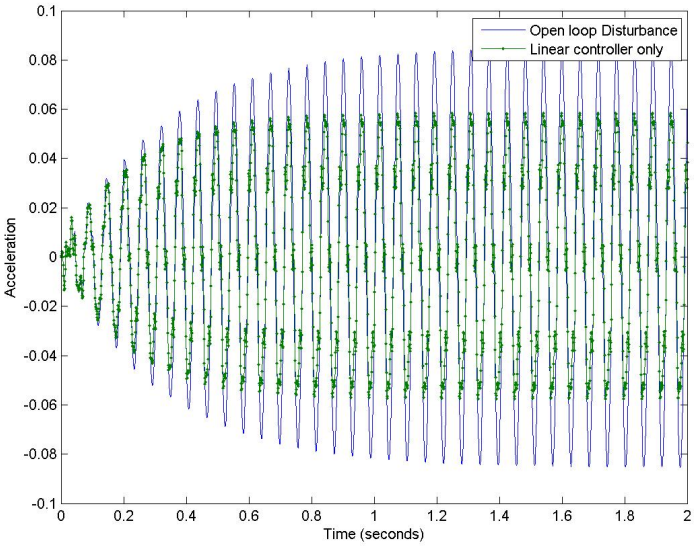

Figure 90: Simulated measured acceleration if tail model when controlled with the linear controller only with tail shifted frequency of 17.2 Hz using twice the design gain (1500) at 32 degrees AOA, 12 psf

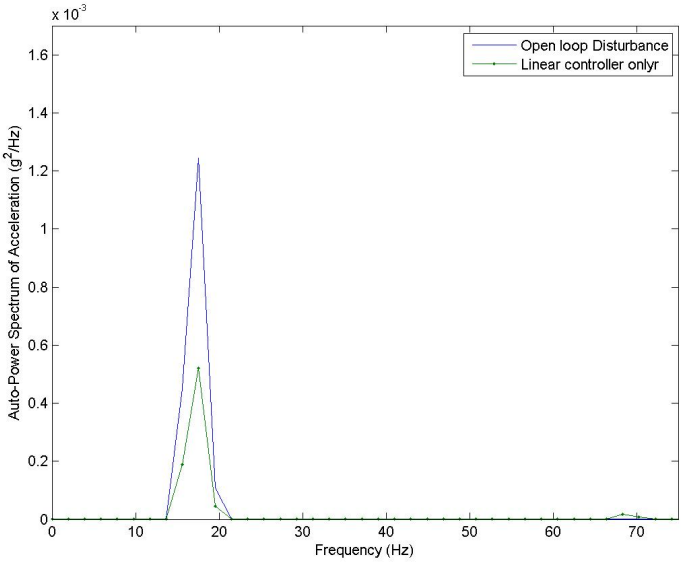

Figure 91: Simulated PSD acceleration if tail model when controlled with the linear controller only with tail shifted frequency of 17.2 Hz using twice the design gain (1500) at 32 degrees AOA, 12 psf

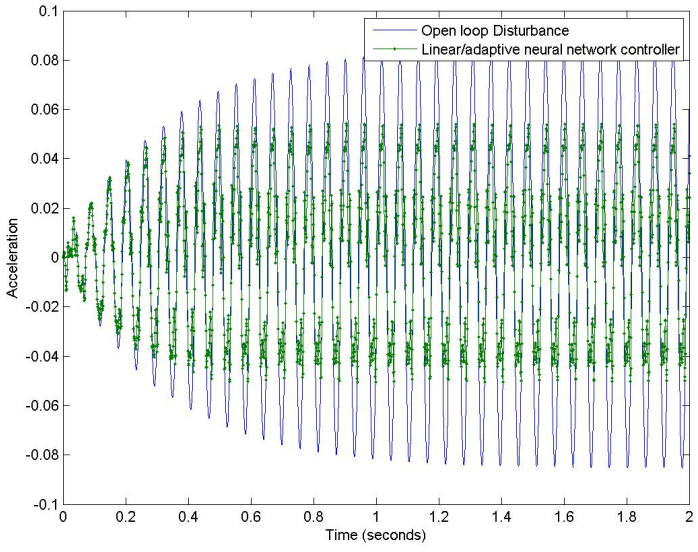

Figure 92: Simulated measured acceleration if tail model when controlled with the linear/adaptive neural network controller with tail shifted frequency of 17.2 Hz using twice the design gain (1500) at 32 degrees AOA, 12 psf

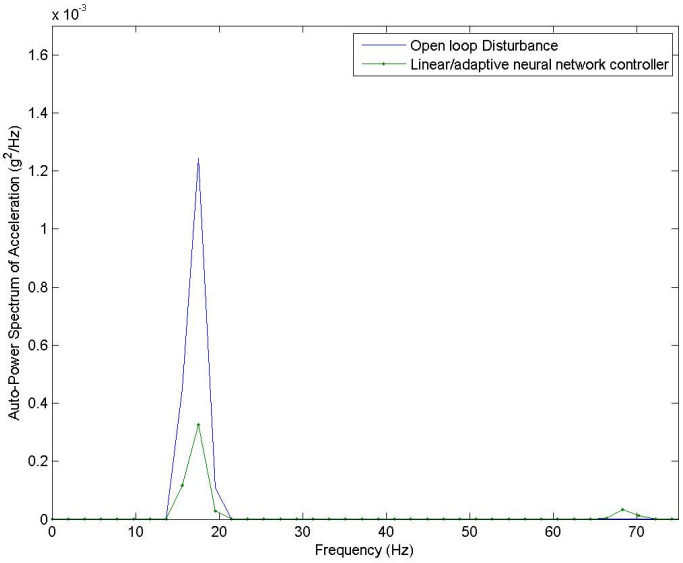

Figure 93: Simulated PSD acceleration if tail model when controlled with the linear/adaptive neural network controller with tail shifted frequency of 17.2 Hz using twice the design gain (1500) at 32 degrees AOA, 12 psf

Table 13: Comparison of simulated RMS reduction for linear controller only and augmented with a neural network when linear controller has twice the design gain (1500)

Plant frequency	Linear controller	Linear controller and neural network
14.41 Hz	41.41%	44.23%
17.2 Hz	33.15%	44.16%

Table 14: Comparison of RMS acceleration reduction on bonded and debonded vertical tails between linear controller and augmented neural network

Tail	Linear controller	augmented neural network
Fully bonded	66.3%	76.4%
Debonded	35.5%	43.9%

modeling error which is incorporated into the controller design.

4.4.7.2 Air pulse testing of the linear controller/adaptive neural network

The experiment is set up to use the neural network with the linear controller. As before, the air pulse is tuned to the first natural frequency of the tail. The results of this experiment are shown in Table (14). These results clearly show that when the adaptive neural network is used with the linear controller the RMS acceleration reduction is greater than with just the linear controller. This shows that the adaptive neural network can reduce vibrations in a continuous system with nonlinearities caused by a delamination. As shown in Table (14), the linear controller loses control authority whenever the structural parameters change as with a debond in this experiment. When the neural network is used it can substantially help reduce RMS acceleration. With these experiments, it has been clearly shown that the adaptive neural network can provide additional reductions in RMS acceleration than what the optimized linear controller can provide. Even with parameter changes, the neural network continues to provide additional reductions in RMS acceleration. The same voltage assessment is performed in this experiment as is performed for the linear controller experiment.

4.5 Summary

There have been many proposed solutions for tail buffet alleviation over the years with only limited results. With numerical simulation and experiments with a 1/12th scale F/A-18 model it has been shown that augmenting a linear controller with an adaptive neural network can provide additional reductions in RMS acceleration for tail buffet alleviation than what the optimized linear controller can provide. Even with parameter changes, the neural

network continued to provide additional reductions in RMS acceleration in numerical simulation and air pulse tests. In the absence of uncertainties the adaptive controller response should be identical or slightly better when compared to the linear controller only response. This has also been validated in the wind tunnel tests by a low angle of attack test with no debond. The angle of attack is low and the airspeed is low to avoid any parameter shifts.

In comparing the results of a single degree of freedom model and air pulse testing, the reduction in RMS acceleration reduction improves when the starboard tail is the only structure that is excited. The empennage body, port vertical tail, and horizontal tails created for this study were not rigid enough to show clear reductions in vibration in all conditions. In hindsight, a rigid empennage body of hard wood or other hard solid material should have been constructed and only the starboard vertical tail should be attached to the empennage body. The port vertical tail and horizontal tails should not have been added. This would isolate the flexible starboard tails vibration. Dynamics from the fuselage, wings, and stinger would have been observed but small enough as to not effect the starboard vertical tail vibration control results. As the linear/adaptive neural network design matures to address additional flexible bodies the flexible vertical and horizontal tails could be added. In addition to a new empennage, further wind tunnel tests should be performed in a wind tunnel that is larger for this size wind tunnel model to ensure there are no issues with tunnel blockage.

Chapter V

STRESS REDISTRIBUTION AND DISPLACEMENT AMPLIFICATION ISSUES WITH THE OFFSET PIEZOCERAMIC STACK ACTUATOR

5.1 Finite element modeling of a beam

One of the key questions raised about using bonded actuators is the stress re-distribution because of active control and stress concentration around the actuator in the controlled structure. Does the OPSA reduce the amount of vibration in a structure at the cost of higher stresses around the actuator? Higher stresses could invalidate the use of the OPSA for vibration reduction if the stresses are too high. To answer this question a finite element model was constructed using the ABAQUS version 5.8 simulation package. The beam portion of the model had the same dimensions as the experimental specimen of reference[71]. In the model, the elastic beam is divided into 384, 20-node quadratic, second-order, isoparametric 3-D brick elements, which use reduced integration. This type of element was chosen because it gives the best results in bending[38]. The elements which make up the beam were assembled in two layers with each element measuring 0.0127 m x 0.0127 m x 6.35×10^{-3} m, aligned in forty eight rows with each row consisting of four elements. The beam is constrained at the base along the beam edges. The material properties of the beam are given in Table 16 and are based on ASTM-A36 steel. The model used Rayleigh damping based on a 1.5% modal damping ratio for the first two modes. For Rayleigh damping, the damping matrix, [C], is a linear combination of the mass, [M], and stiffness, [K], matrices.

$$[C] = \tilde{\alpha}[M] + \tilde{\beta}[K] \tag{109}$$

Table 15: Cantilever beam dimensions

Length	24 inches	0.610 m
Thickness	0.5 inches	0.0127 m
Width	2 inches	0.05 m

Table 16: Beam Material Properties

Youngs modulus	$29.0x10^6 \frac{lbf}{in^2}$	200 GPa
Poissons ration	0.3	0.3
Density	$7.355x10^{-4} \frac{lbfsec^2}{in^4}$	$7860 \frac{kg}{m^3}$

The values of $\tilde{\alpha}$ and $\tilde{\beta}$ are evaluated using the following equation (110).

$$\zeta_i = \frac{\tilde{\alpha}}{2\omega_i} + \frac{\tilde{\beta}\omega_i}{2} \tag{110}$$

In this equation, ω_i and ζ_i are the natural frequency and damping ratio of the $i$the bending mode. In this study, two different models are constructed. The first model is the steel cantilever beam, without the actuator, as a reference. The second model is the closed loop model, with the actuator and controller, as illustrated in Figure 94. For both cases, the first three bending modes in the 2-3 plane and associated natural frequencies are computed for the system.

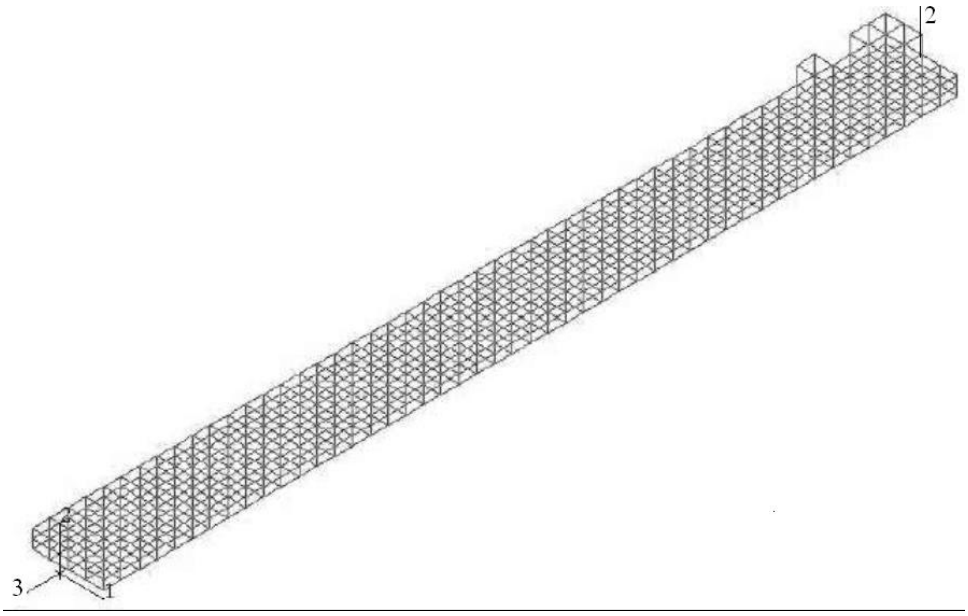

Figure 94: Wire Frame of the finite element model of the beam with OPSA

5.1.1 Beam FEM model without actuator

The first three natural frequencies of the beam without an OPSA are listed in Table 17 and the calculated Rayleigh damping coefficients are in Table 18.

Table 17: First three natural frequencies of the FEM cantilever beam without an OPSA (bending in 2-3 plane)

Mode 1	27.808 Hz
Mode 2	174.01 Hz
Mode 3	486.07 Hz

Table 18: Rayleigh damping values for the cantilever beam without the OPSA for 1.5% damping

Coefficient	Value
$\tilde{\alpha}$	4.5194
$\tilde{\beta}$	2.365810^{-5}

To study the stress distribution, the beam was driven by a harmonic tip load at the calculated natural frequency of the first bending mode of the beam. This tip load is collocated with the node where the sensor is placed. The amplitude of the transverse disturbance force is chosen to be 0.9 lbf (4 N) to insure that the small displacement assumptions of the analysis are satisfied while generating stresses that are larger than 10% of the ultimate strength. The resulting tip displacements are illustrated in Figure 95. The amplitude of the steady state displacement is 0.217 in. (5.51 mm).

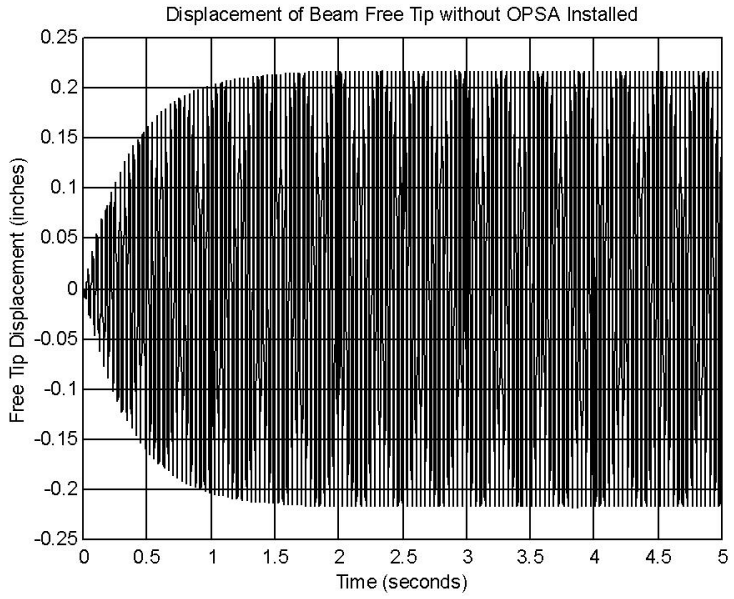

Figure 95: Displacement of the free tip of the cantilever beam without OPSA

5.1.2 Model for OPSA

A typical offset piezoceramic stack actuator (OPSA) assembly, proposed by Bayon de Noyer and Hanagud[32], is shown in Figure 3. A piezoceramic stack is placed parallel to the structural surface. The stack is attached to the surface using a relatively rigid mount. The longitudinal motion of piezoceramic stack is constrained to generate axial forces. Due to the offset from contact points to the structural surface, these axial forces result in forces and moments at the tail structure as illustrated in Figure 2.

Piezoceramic stacks use the direct d_{33} piezoelectric coefficient instead of the transverse d_{31} coefficient that is used in PZT wafers-actuators[80]. A piezoelectric ceramic stack consists of a stack of PZT layers. The displacements of each layer are added together to produce the total displacement of the stack. The design of the OPSA is such that the piezoceramic stack is easily removable and replaceable while the mount is attached to the structure. Thus, the maintainability of the offset piezoceramic stack actuator is far superior to PZT wafers, which, once bonded, cannot be easily removed from the controlled structure. For the purpose of modeling the piezoceramic stack, the transverse effects are neglected because the stresses and input electric fields in the transverse directions are zero. As a result, the strain distribution in the longitudinal direction, x, is obtained as a function of the longitudinal stress distribution and the longitudinal applied electric field distribution. For this unidirectional model, the two constitutive equations governing the behavior of the piezoelectric material in its longitudinal direction are[71]:

$$\epsilon_x = \frac{\sigma}{Y_s^E} + d_{33}E \tag{111}$$

$$D = \epsilon_{33}E + d_{33}\sigma \tag{112}$$

In these equations, the longitudinal strain in the piezoceramic stack is denoted as ϵ_x, σ the longitudinal stress, Y_s^E is the longitudinal Youngs modulus of the stack (The sub index "s", here and later on, stands for the piezoceramic stack), d_{33} is longitudinal piezoelectric charge constant, E the electric field in the stack, D the electric displacement field and ϵ_{33} is the dielectric constant. Rewriting Equation (111), to obtain the stress field as a function

of strain and electric field it is shown that

$$\sigma = Y_s^E \epsilon_x - d_{33} Y_s^E E = \frac{F_s}{A_s} \tag{113}$$

where A_s is the cross sectional area of the stack.

Since the thickness of the electrodes are small compared to the thickness of the piezoceramic layers, it is assumed that the Youngs modulus, Y_s^E, is independent of the longitudinal coordinate, x. The product $d_{33}E$ is also assumed to be independent of the longitudinal coordinate, x. This is because the sign of the product of the piezoelectric charge constant and the electric field, $d_{33}E$, has to be the same over the entire stack to produce maximum actuation. The thickness of each piezoceramic layer is small enough to assume that the d_{33} coefficient is homogeneous and that the electric field is constant within each layer. This results in the assumption of a piezoceramic rod model for the stack. Then, the axial force F_s exerted by the stack is equal to the product of the axial stress σ and the cross-section area of piezoceramic stack A_s, i.e. F_s=σA_s.

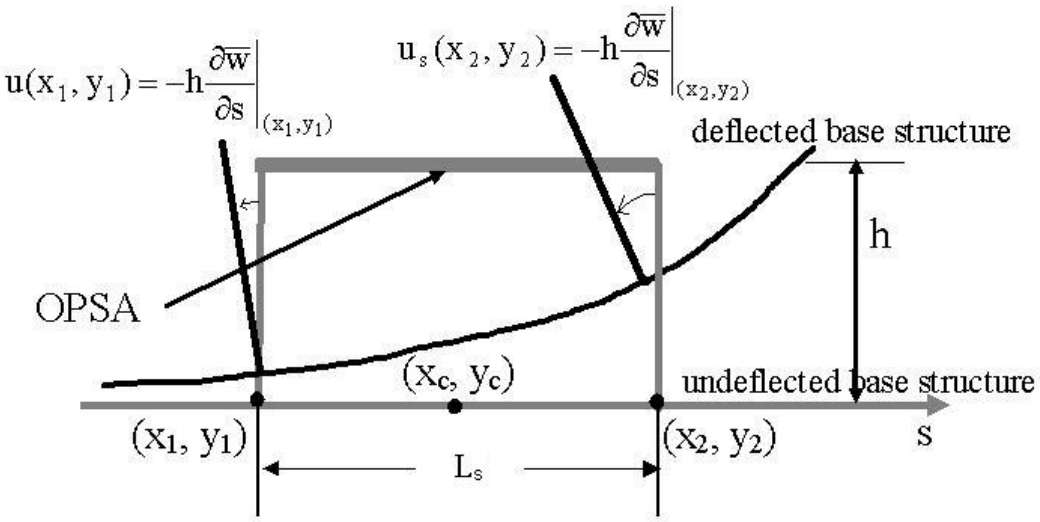

Figure 96: The axial deformation of OPSA by the deflection of base structure

The span length of the stack is assumed to be given by L_s=$n_{layer} \times t_{layer}$. The OPSA is designed with a rounded surface such that the piezoceramic stack can rotate but does not bend or twist during the deformation of the structure. This means that the stack can only extend or contract, during the deformation of the structure. The contact with the structure

is assumed to be through a pre-compression of the piezoceramic stack in OPSA by use of a compression bolt. Because all individual layers in a piezoceramic stack are subjected to the same voltage, a uniform axial strain is assumed. The axial deformation of piezoceramic stack is associated with the deformation of the structural surface (see Figure 96). If the undeflected tail structure is in the xy-plane and OPSA is placed in an arbitrary direction in the xy-plane. The center of the stack is located at (x_c, y_c) (See Figure 97). The uniform strain in the stack is assumed to be the difference in position of the ends of the stack divided by the stack length. The height of each OPSA mount is h. The position of the top of each OPSA mount when the tail is deformed along $\overrightarrow{s}$ is given by

$$u_s(x_i, y_i) = -h\frac{\partial \overline{w}(x_i, y_i)}{\partial s} \tag{114}$$

If it is assumed that the ends of the OPSA mounts are in constant contact with the ends of the stack, the axial strain in stack is

$$\epsilon = \frac{u_s(x_2, y_2) - u_s(x_1, y_1)}{L_s} = -\frac{h}{L_s}\frac{\partial \overline{w}}{\partial s} \tag{115}$$

If it is assumed that the spontaneous electric field is negligible, i.e. the internal electric

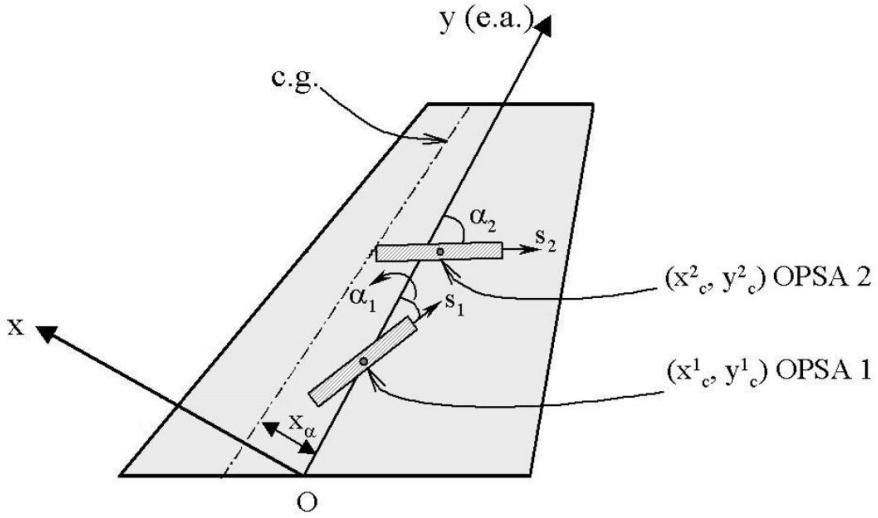

Figure 97: FA-18 vertical tail with OPSAs installed

field of stack is equal to the external acting electric field, and assume that electric field is

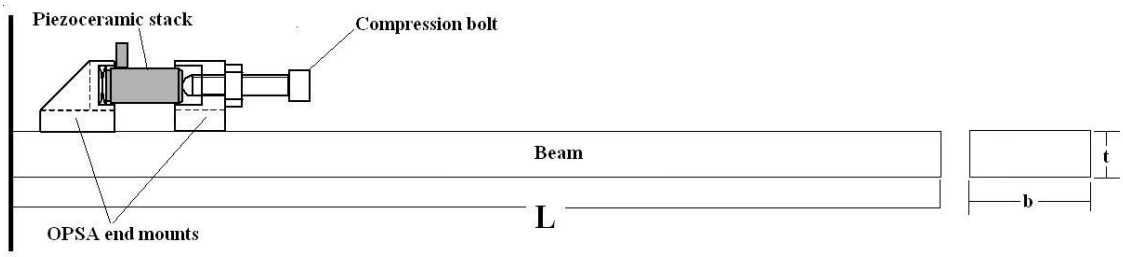

Figure 98: Offset Piezoceramic Stack Actuator Mounted on a Cantilever Beam

uniform through the span, the axial force F_s is approximated by

$$F_s = A_s Y_s^E d_{33} E(t) + k_s^\epsilon h \left(\frac{\partial w(x_2, y_2, t)}{\partial s} - \frac{\partial w(x_1, y_1, t)}{\partial s} \right) = -k_s^E V(t) - k_s^\epsilon h \left(\frac{\partial \overline{w}}{\partial s} \Big|_{(x_1, y_1)}^{(x_2, y_2)} \right) \tag{116}$$

where

$$k_s^\epsilon = \frac{A_s Y_s^E}{L_s} \tag{117}$$

$$k_s^E = \frac{A_s d_{33} Y_s^E}{t_{layer}} \tag{118}$$

(x_1, y_1) and (x_2, y_2) are the coordinates of the two mounting points of OPSA.

5.1.3 Closed Loop FEM models

For the closed loop model, the OPSA is incorporated in the finite element model. The end mount closest to the root of the beam is made of two layers of four brick elements similar to those used for the beam, each measuring 0.0127 m x 0.0127 m x 0.0127 m while the other end mount contains two layers of two brick elements. The model used spring elements to simulate the piezoelectric stack. The distributed load is calculated in each time interval by using the ABAQUS DLOAD subroutine. The calculation of the control forces is made in this subroutine, at each time step. Four tetrahedral elements were placed on each opposing face of each mount. These elements each have one node outward from the base mount in which they are installed. Then an 8-node brick element with a surface area for the distributed load of 5 mm x 5 mm is placed at each free node of the four tetrahedral set per mount. This area corresponds to the cross-section area of the actual piezoelectric stack. The offset piezoceramic stack is simulated by four linear spring elements in parallel mounted between

Table 19: Properties of the Piezoceramic Stack (PI-830.10)

Length, ΔL	18 mm
Cross Sectional Area, A_s	$2510^{-6}m^2$
Youngs Modulus, Y_s^E	55.25 GPa
Piezoelectric Constant, d_{33}	$635 \times 10^{-12} \frac{m}{V}$
Density, ρ_s	$8000 \frac{kg}{m^3}$
Number of Layers, n_s	200

Table 20: First three natural frequencies of the FEM cantilever Beam with OPSA

Mode 1	29.823 Hz
Mode 2	181.48 Hz
Mode 3	495.21 Hz

the opposing faces of the two mounts. The equivalent spring stiffness of the four springs is calculated using Equation 117. The four spring elements were connected between the two opposing 8-node brick elements. The stack forces were simulated by applying distributed loads on the opposing faces of the 8-node brick elements. The first three natural frequencies and Rayleigh damping coefficients are listed in Table 20 and Table 21.

The active vibration control is achieved using acceleration feedback control (AFC). The equations of motion of a system with AFC are as follows[15].

$$[M]\{\ddot{x}\} + [C]\{\dot{x}\} + [K]\{x\} = -[\Gamma_{act}][G][\Omega_c]\{\eta\} + \{f\} \tag{119}$$

$$\{\ddot{\eta}\} + [\mathrm{A}_c]\{\dot{\eta}\} + [\Omega_c]\{\eta\} = [1_p][\Gamma_{sensor}]\{\ddot{x}\} \tag{120}$$

In these equations, {x} is the vector of degrees of freedom of the finite element model ($x \rightarrow \Re^3$), $\{\eta\}$ is the vector of the p compensator coordinate($\eta \rightarrow \Re^3$), $[\Gamma_{act}]$ is influence matrix of the actuator, $[\Gamma_{sensor}]$ is influence matrix of the accelerometer, $[\Lambda_c]$ is the compensator modal damping ratios and $[\Omega_c]$ is the compensator frequencies, [G] is the feedback gain matrix and 1_p is a vector of length p, with one for each entry, to account for the fact that all compensators are placed in parallel.

Table 21: Rayleigh Damping Values for the FEM cantilever beam with OPSA

Coefficient	Value
$\tilde{\alpha}$	4.8280
$\tilde{\beta}$	2.2596×10^{-5}

Table 22: Modal Influence Coefficients of the OPSA and sensor

Coefficient	Value
a	-2.175×10^{-3}
b	15.27

For the cantilever beam with the OPSA, the influence vector of the actuator is zero everywhere but at the eight nodes where the control forces are applied. At each node, the magnitude of the influence is $A_s/8$. The influence vector of the accelerometer is zero everywhere but for the node at which the sensor is placed where the influence is unity in the transverse direction 2. In this study, the system was driven at the first bending frequency. When observing a single mode of the system equations (119) and (120) is reduced to the following system:

$$\begin{aligned} \ddot{q} + 2\xi_s\omega_s\dot{q} + \omega_s^2 q &= -a\gamma\omega_c^2\eta + f(t) \\ \ddot{\eta} + 2\xi_c\omega_c\dot{\eta} + \omega_s^2\eta &= b\ddot{q} \end{aligned} \tag{121}$$

where q and η are the modal coordinates of the first bending mode of the structure and of the compensator, respectively, ω_s, ω_c, ξ_s and ξ_c are the natural frequencies and the damping ratios of the structure and the compensator, respectively, γ is the scalar gain applied to the feedback signal, and a and b are the modal influence parameters of the actuator and sensor, respectively. To compute the compensator parameters, the modal influence parameters are computed. Using the mass normalized mode shape of the first mode, ϕ_1, the influence coefficients a and b are given by:

$$a = \lfloor\phi\rfloor \{\Gamma_{act}\} \tag{122}$$

$$b = \lfloor\Gamma_{sensor}\rfloor \{\phi\} \tag{123}$$

The computed influence coefficients are given in Table 22.

It should be noted that the finite element model is not a single mode model as it has many nodes with translational and rotational degrees of freedom. The objective of the controller in this study is to minimize the displacement response of the beam due to the harmonic transverse load. Hence, the design of the acceleration feedback controller was based on the minimization of the H_2 norm of the closed loop receptance for a given control gain[14]. For such a design, the gain of the controller is a design parameter and the frequency

Table 23: Controller Parameters for controlling the FEM cantilever beam

Parameter	Value
ω_c	$187.38\frac{rad}{s}$
ξ_c	14.408%
γ	-2.5

and damping ratio of the controller are given by[16]:

$$\omega_c = \omega_s \tag{124}$$

$$\xi_c = \frac{1}{2}\sqrt{ab\gamma} \tag{125}$$

The feedback gain, γ, is chosen to be -2.5 to produce the largest amount of force (1kN) from the piezoceramic stack mounted on the beam. The piezoceramic stack used on the beam is a Polytec PI-810.10. This value of the gain satisfies the first condition. This value provides an order of magnitude displacement reduction and is selected to generate the maximum control forces that are actually obtained. The controller parameters are given in Table 23.

To implement the controller within the simulation package (See Appendix B), the following procedure for the computation of the control force is employed:

1. The tip acceleration at a node on the free end in the 2-direction is read at the end of each time increment.

2. At the beginning of the next increment, the acceleration from the end of the previous increment is read into USRFIL subroutine, which is imbedded into the ABAQUS input file.

3. This acceleration is passed from the USRFIL subroutine to the DLOAD subroutine, which uses a sixth order Runge-Kutta numerical integration to solve the second equation in (121) to find the value of η.

4. This value of η is used to compute the distributed control force per the equation (121)

5. This distributed control force is then passed back to the model where it is implemented at the end of the time increment.

$$Fc = -\gamma\omega_c^2\eta \tag{126}$$

This process is iterated every time increment of 0.001 seconds. The time interval of the simulation is chosen to be five seconds in order to end the simulation well into the steady state regime. The time domain results of this analysis are illustrated by Figure 99. Compared with the open loop beam (Figure 95), the displacements are significantly reduced and steady state is reached in approximately 1 second. The amplitude of the steady state vibration is 1.89×10^{-2} in (0.48 mm) which is more than an order of magnitude smaller than the amplitude of the open loop beam.

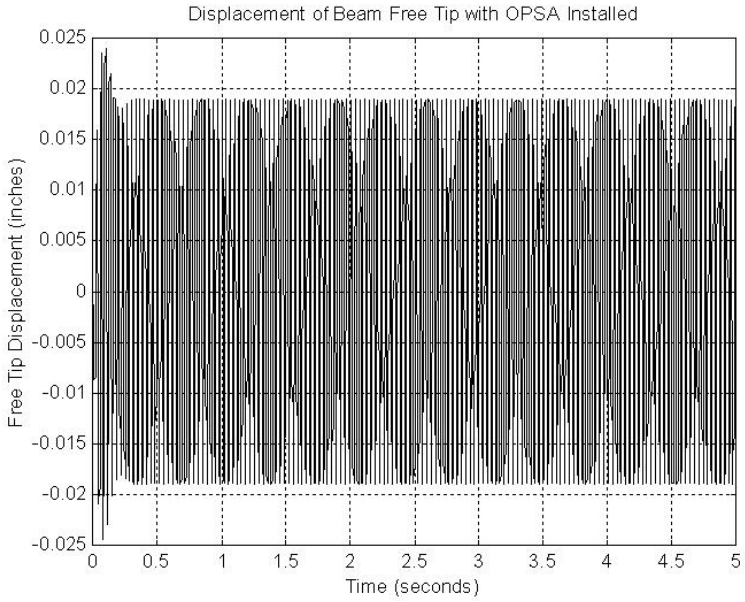

Figure 99: Closed loop displacement of the free tip of the cantilever beam with OPSA and acceleration feedback control

5.1.4 Stress study

The stress fields are obtained at two beam positions (1) maximum positive displacement of the free tip of the beam and (2) zero displacement of the free tip of the beam. This choice is motivated by the fact that bending stresses are the largest at maximum displacement and, for comparison with the closed loop beam, actuator induced stresses are maximum at zero displacement of the free tip of the beam. The longitudinal stresses, σ_{33}, for the beam

without an OPSA are illustrated in Figure 100 while the shear stresses, τ_{23}, are illustrated in Figure 101.

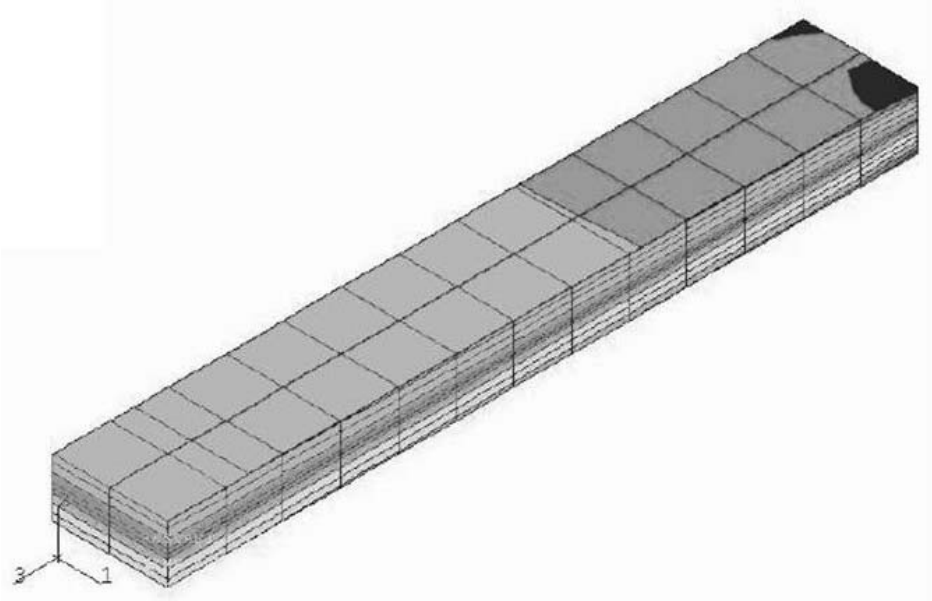

Figure 100: Central cross section of the longitudinal stress, σ_{33}, for the cantilever beam without OPSA

The maximum longitudinal stresses are located on the upper surface of the root of the beam and have a magnitude of 12 ksi (82.74 MPa), which is more than 10% of the ultimate strength of the material of the beam. Similarly, the maximum shear stresses are located in the same area and have a magnitude of 4.3 ksi (29.65 MPa). For the closed loop stress study, two different times are considered. As for the case of the beam without active control, the stresses at maximum displacement are studied. However, since the control force has a 90 degree phase difference with respect to displacement, the large control forces are exerted when the tip displacement is zero.

Figures 102 and 103 illustrate the longitudinal and shear stresses, respectively, for the case where beam tip displacement is maximum. The maximum longitudinal stresses are located on the upper and lower surface of the root of the beam with a magnitude of 1.25 ksi (8.6 MPa) which is an order of magnitude less than the beam open loop shown in Figure 100. The maximum shear stress magnitude of the closed loop beam is 0.55 ksi (3.8 MPa) on the upper surface of the root of the beam. These closed loop stresses are approximately an

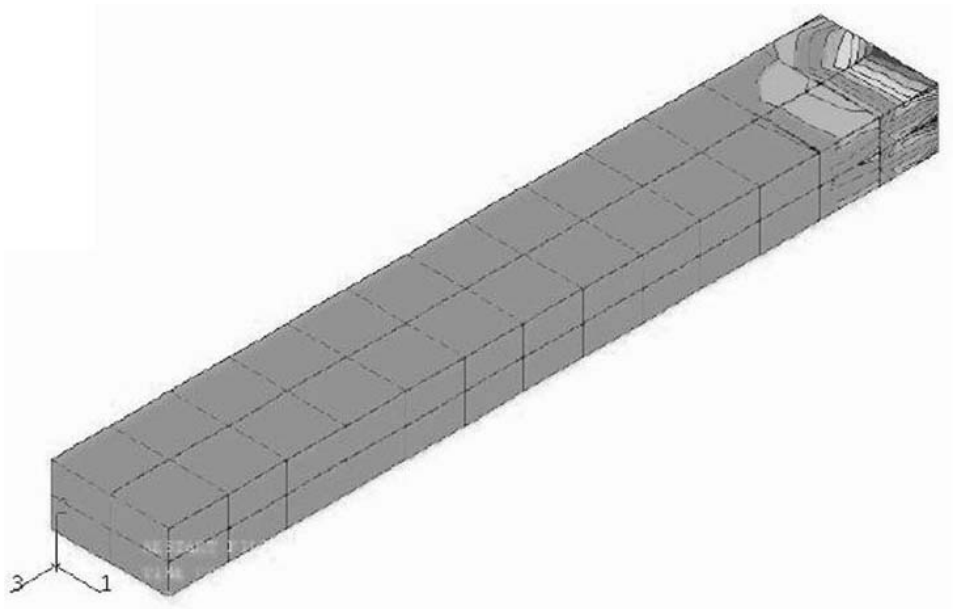

Figure 101: Central cross section of the shear stress, τ_{23}, for the cantilever beam without OPSA

order of magnitude lower than the ones (4.3 ksi) of the beam without active control in the same location (See Figure 101).

During the steady state motion, the maximum distributed control load calculated by the ABAQUS DLOAD subroutine is obtained when the beam displacement is zero. The maximum value at this position was 5.8 ksi (40 MPa), which for the area of the stack is equivalent to a control force of 1 kN. This result validated the choice for the controller gain since it was designed to generate the maximum control force that is delivered by the stack in the beam that was 1kN. When the control forces are maximum, the location of the largest longitudinal stress at the position in between the two mounts, as illustrated by Figure 104. The amplitude of this maximum stresses was 1.5 ksi (10.3 MPa) which is six times smaller than the open loop stress of 12 ksi at the same location.

5.2 Finite element modeling of a plate

In actual practice, the OPSA would be installed on the skin of the vertical tail that is typically much thinner than the beam of the previous section. It has yet to be determined if the active control with OPSA will cause higher stress concentrations in a thin plate

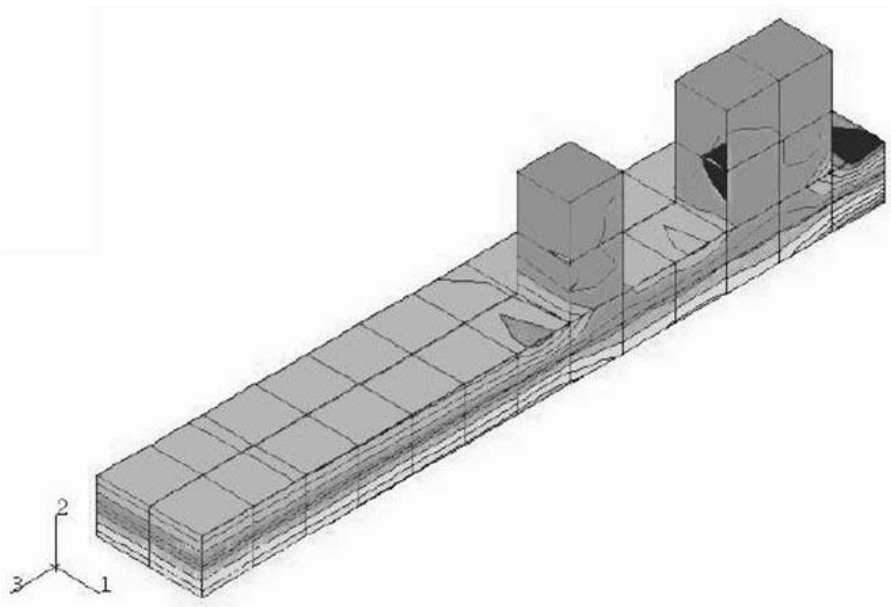

Figure 102: Central cross section of the longitudinal stress, σ_{33}, in the cantilever beam for the closed loop system at maximum displacement

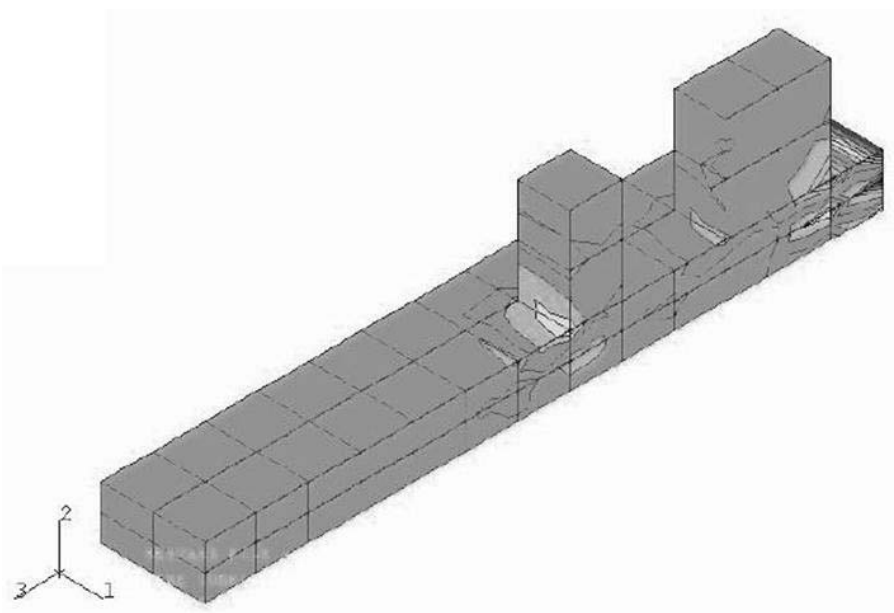

Figure 103: Central cross section of the shear stresses, τ_{23}, in the cantilever beam for the closed loop system at maximum displacement

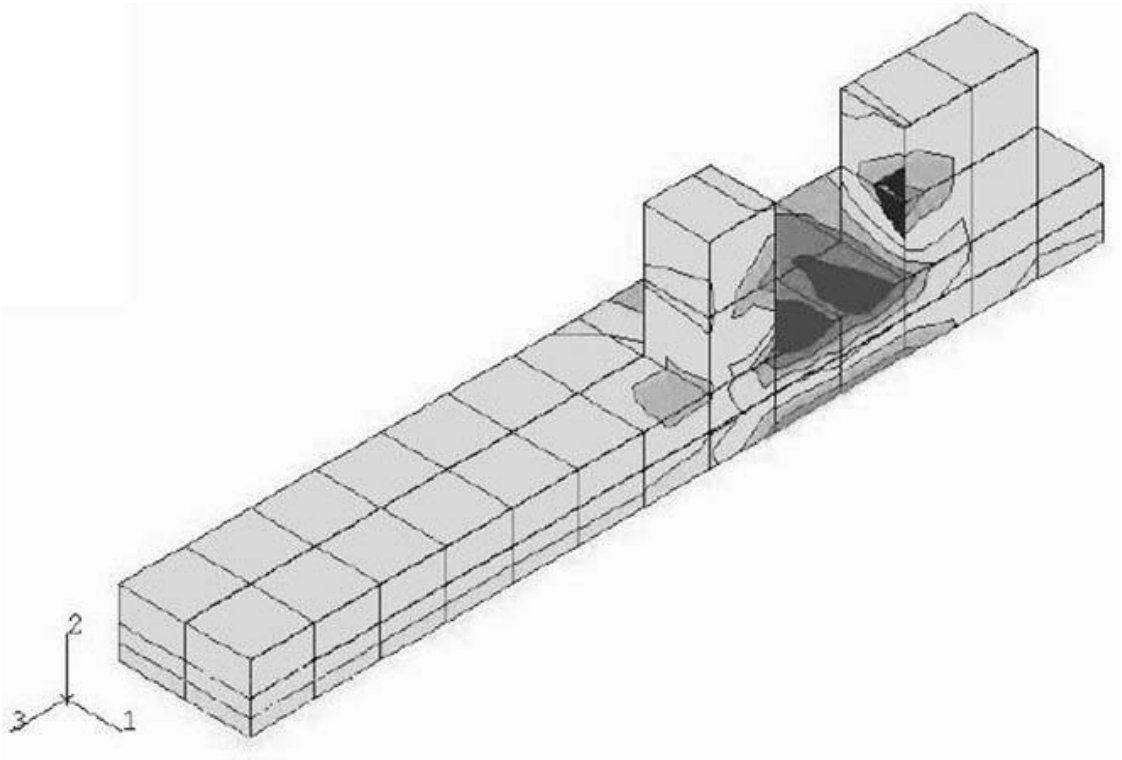

Figure 104: Central cross section of the longitudinal stress, σ_{33}, in the cantilever beam for the closed loop system at maximum control force

Table 24: FEM cantilever plate dimensions

Length	24 inches
Width	8 inches
Thickness	0.125 inches

type structure. Model based studies of closed loop control of a plate structure using an offset piezoceramic stack based actuator and have not been reported. This investigation studied how effective the OPSA actuator is when applied to a plate. Local stresses in the structure resulting from a moment inducing externally mounted piezoceramic stack actuator are also studied. The concern in plate structures and use of OPSA actuators was that the control forces would produce high local stresses thus eliminating the OPSA as a candidate to reducing vibrations in these thin-walled type structures.

5.2.1 Plate FEM model without actuator

The case study performed is of a plate with a length to width aspect ratio of 3 to 1. Finite element models are used to compare stresses in the plate with the actuator installed with stresses in the open loop and closed loop system. The dimensions of the plate are given in Table 24.

As in the case of the beam, the finite element models are constructed in the ABAQUS version 5.8 simulation package. In the models, the plate and OPSA mount portions are composed of 20-node quadratic, second-order, isoparametric 3-D brick elements, which use reduced integration. The plate is fully constrained at the base along the root edges. The material properties of the plate and OPSA mounts are the same as the beam and are given in Table 16. The models used Rayleigh damping based on a 1.5% modal damping ratio for the first two bending modes. This damping ratio is chosen as it simulates a typical aircraft wing. For Rayleigh damping, the damping matrix, [C], is a linear combination of the mass, [M], and stiffness, [K], matrices and are used in equation (109) and the values of $\tilde{\alpha}$ and $\tilde{\beta}$ are evaluated using the equation (110). This same procedure is used for the cantilever beam. For this study, two models are constructed. The first model is the steel cantilever plate with OPSAs installed but not activated (open loop).

Table 25: First three natural frequencies of the FEM cantilever plate without an OPSA

Mode 1	7.0943 Hz
Mode 2	43.674 Hz
Mode 3	44.320 Hz

Table 26: Rayleigh damping values for the cantilever plate without the OPSA

Coefficient	Value
$\tilde{\alpha}$	1.265
$\tilde{\beta}$	3.629×10^{-5}

5.2.2 Closed loop FEM models

The second model is the closed loop model. For both cases, the first three modes in the 1-3 plane and associated natural frequencies are computed for the system. The plate is driven by a harmonic tip load at the center of the free end of the plate. The frequency of this harmonic load corresponds to the natural frequency of the first bending mode of the plate/OPSA assembly. This tip load is collocated with the sensor node. The amplitude of the transverse disturbance force is chosen to be 0.5 lbf to insure that the small displacement assumptions of the analysis were satisfied. Figure 105 and 106 display the plate with the OPSA installed.

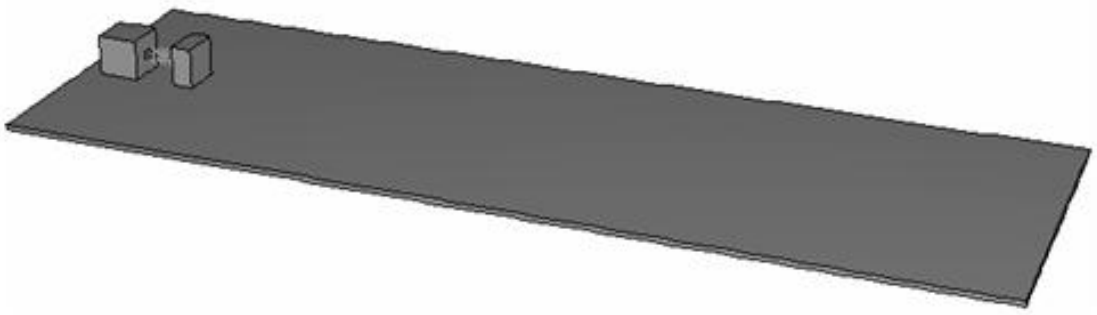

Figure 105: Plate with OPSA

For the closed loop models, the OPSA is activated in the finite element model using the same ABAQUS subroutine (DLOAD) as used with the beam. The OPSA mounts are simulated by using the same OPSA FEM actuators that are used on the beam in the previous section.

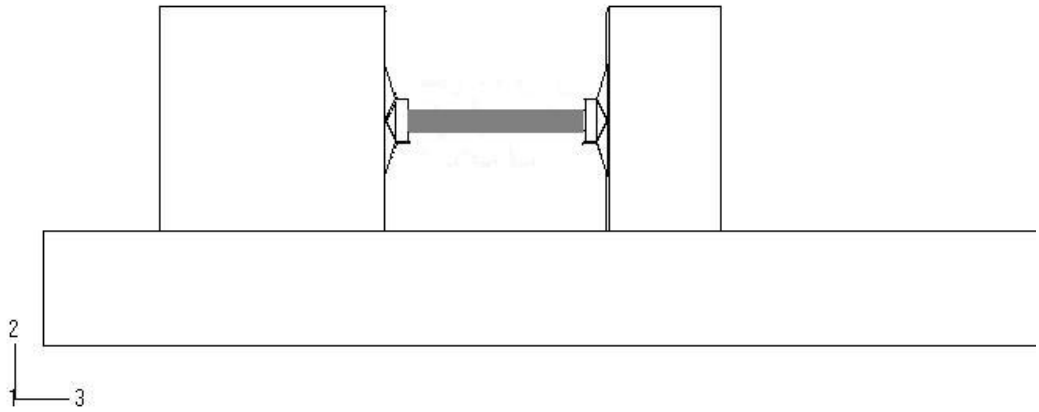

Figure 106: Closeup of plate with OPSA

Table 27: First three natural frequencies of the FEM cantilever plate with OPSAs installed

Mode 1	7.7736 Hz
Mode 2	44.450 Hz
Mode 3	46.842 Hz

Table 28: Rayleigh damping values for the cantilever plate with OPSAs installed

Coefficient	Value
$\tilde{\alpha}$	1.257
$\tilde{\beta}$	8.742×10^{-5}

Table 29: Modal Influence Coefficients of the OPSA and accelerometer

Coefficient	Value
a_1	-6.095×10^{-4}
a_2	15.40

Table 30: Cantilever plate controller parameters

Parameter	Value
ω_c	$48.843 \frac{rad}{s}$
xi_c	15.32%
γ	-2.5

The results of this analysis are illustrated by Figure 107. This figure shows how effective the active control system is in reducing the vibrations in the plate. The amplitude of the steady state vibration is 0.2 in.

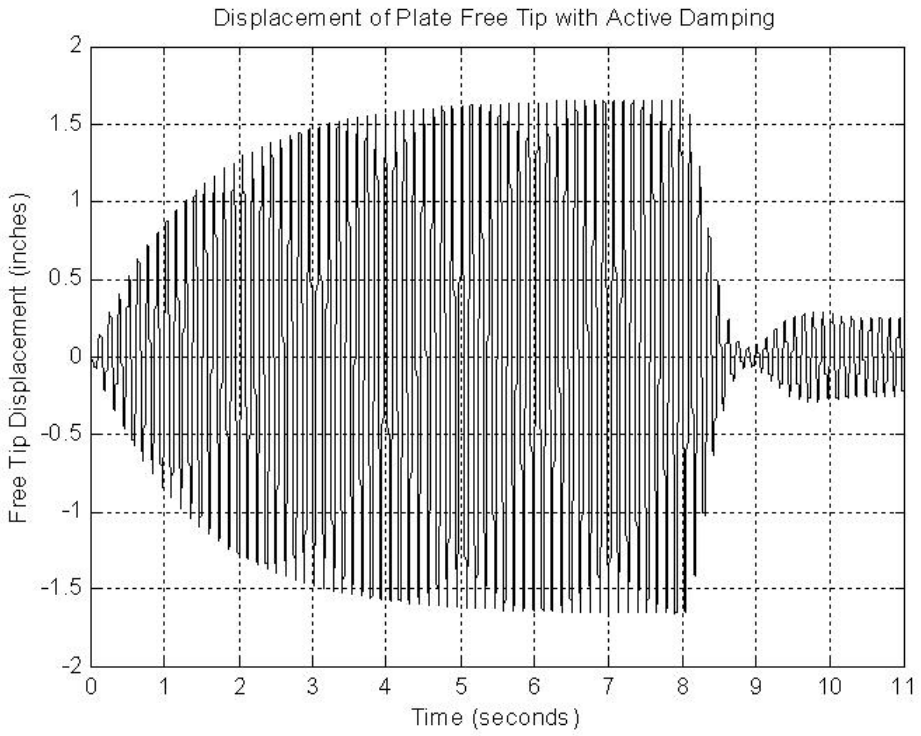

Figure 107: Open loop then closed loop displacement of the free tip of the plate with OPSA and acceleration feedback control

The feedback gain, γ, is selected to be -2.5.

5.2.3 Stress study

For the case of a plate with OPSAs installed but not activated (open loop), the stress fields are obtained at a maximum positive displacement of the free tip of the plate. This choice is motivated by the fact that ending stresses are the largest at the root when the tip displacement is maximum. The figures in this section only show the first 25% of the plate that has been sectioned longitudinally so as to easily observe the stress distributions. The maximum longitudinal stress, σ_{11}, has a magnitude of 58 ksi (400 MPa), which is equal to the ultimate strength of the material of the plate, and is located on the upper surface of the plate. The maximum lateral stress, σ_{22}, has a magnitude of 50 ksi (345 Mpa). The

maximum shear stress in the 1-2 plane is 2.85 ksi (19.65 Mpa).

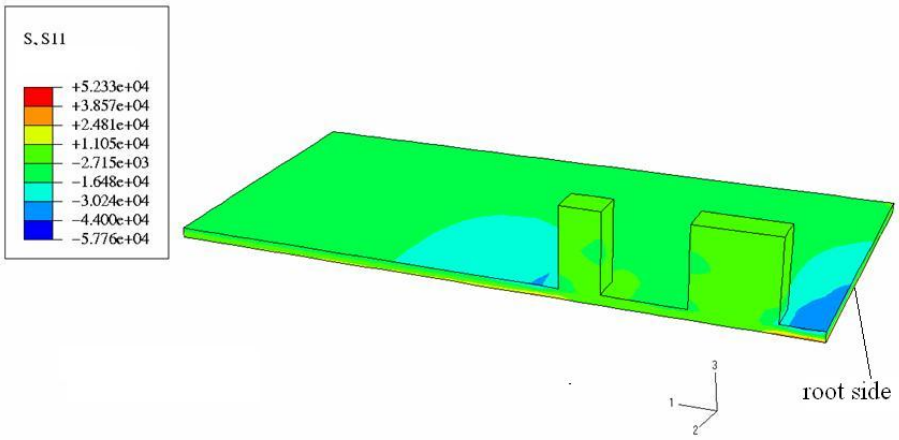

Figure 108: Zoom of central cross section of the longitudinal stress, σ_{11}, open loop

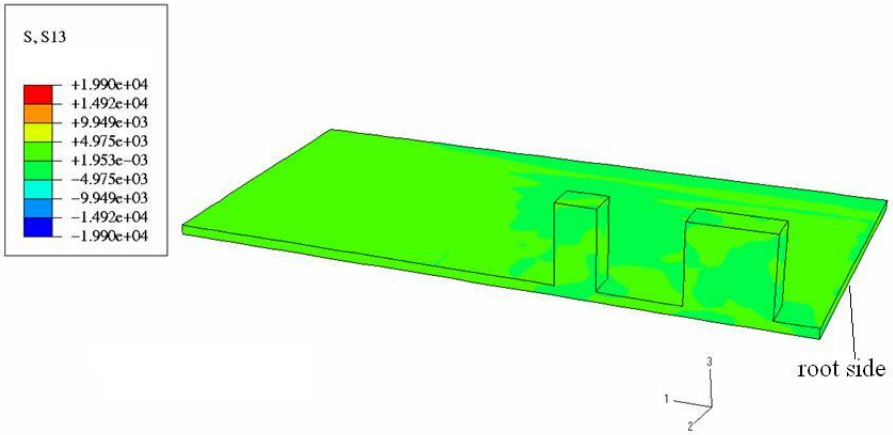

Figure 109: Zoom of central cross section of the shear stresses, τ_{13}, open loop

For the closed loop stress study, two different intervals were considered (1) maximum tip displacement and (2) zero tip displacement. However, since the control force has a 90 degree phase difference with respect to displacement, the largest control force is exerted when the tip displacement is zero. Figure 110 and 111 illustrates the longitudinal and shear stress fields, respectively, for the maximum tip displacement case. At this position, the maximum longitudinal stresses, σ_{11}, has a magnitude of 8.6 ksi (59.3 MPa) which is an 85% reduction in stress. The normal stress in the 2-direction, σ_{22}, is 3.3 ksi (22.7 Mpa) which is a 93.4% reduction from the open loop. Further, the longitudinal stresses near the OPSA

are much smaller than the stresses in the same area for the open loop case. Similarly, the maximum shear stress magnitude is 1.3 ksi (9 MPa) which is 54% reduction in shear stress from the open loop.

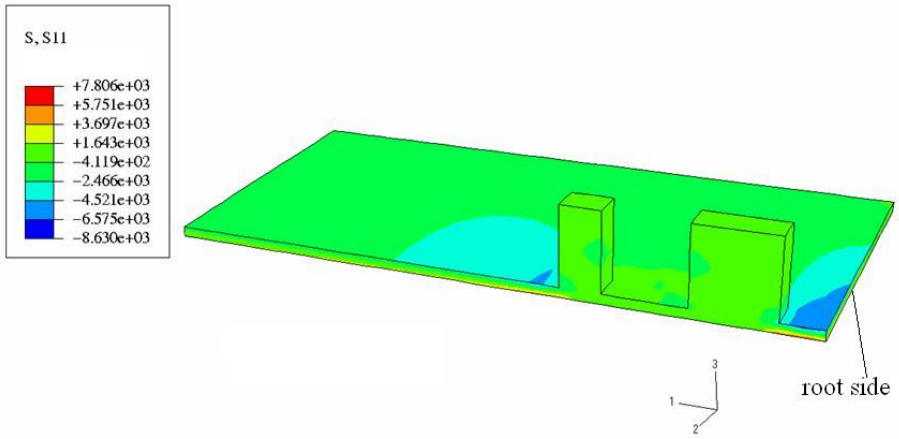

Figure 110: Zoom of central cross section of the longitudinal stress, σ_{11}, for the closed loop system at maximum displacement

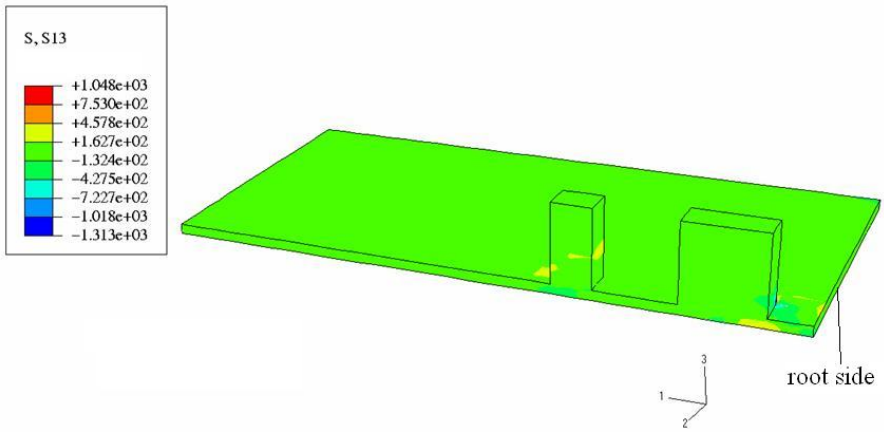

Figure 111: Zoom of central cross section of the longitudinal stress, τ_{13}, for the closed loop system at maximum displacement

During the steady state, the maximum distributed control forces are obtained when the plate displacement is zero. When, the control forces are maximum, the highest longitudinal stresses, σ_{11}, within the plate are centered in between the two OPSA mounts, is shown in Figure 112. The amplitude of the maximum stress is 2.25 ksi (15.5 MPa). The maximum

normal stress in the 2-direction, σ_{22}, is 11.1 ksi (76.5 Mpa). This shows that the maximum control force does not increase the amount of stress from the open loop case in thin walled structures. In observing the shear stress, τ_{12}, during the interval of maximum control force the maximum shear stress is 8.6 ksi (59.3 MPa). This study clearly shows that the maximum control force does not increase the amount of stress from the open loop case in thin shell structures.

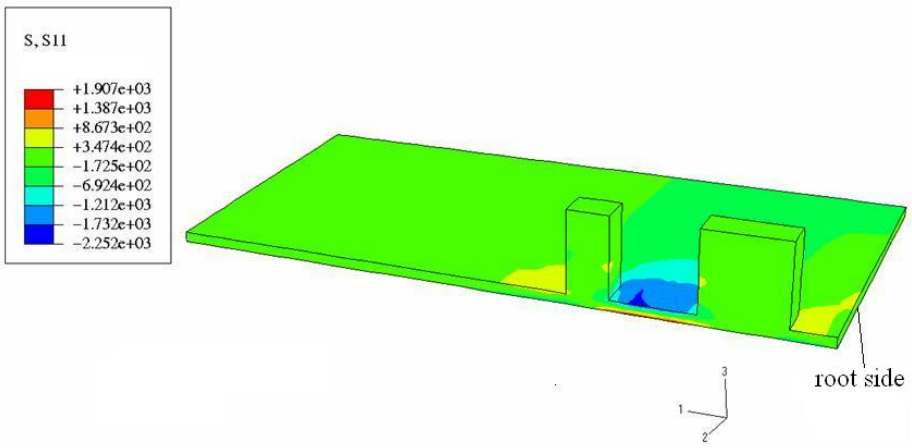

Figure 112: Zoom of central cross section of the longitudinal stress, σ_{11}, for the closed loop system at maximum control force

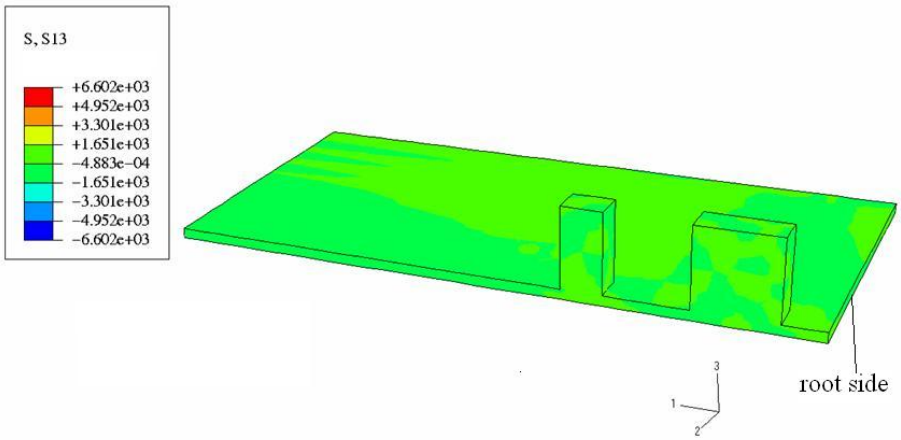

Figure 113: Zoom of central cross section of the longitudinal stress, τ_{13}, for the closed loop system at maximum control force

5.3 Summary

A 3-D finite element model is used in combination with a numerical modeling of acceleration feedback control to simulate active damping in a cantilever beam and a plate structure by the use of active control using OPSA. This confirmed the OPSA design as an excellent candidate for vibration reduction solutions for thin-walled structures. This simulation also indicates that a control system based on OPSA actuators and acceleration feedback control is a feasible solution for fatigue life enhancement of thin walled structures. Further, with

this study of the stress re-distribution due to OPSA, the optimization of such an actuator design should be greatly enhanced.

Chapter VI

CONCLUSIONS AND RECOMMENDATIONS

The contributions made in this thesis are

- The development of a design procedure to enhance the fatigue life of structures by using active control due to buffet induced vibrations. This procedure also produces methods to determine the number and type of offset piezoceramic stack actuators required for a desired amount of control authority using an acceleration feedback controller.

- The development of an acceleration feedback controller augmented with an adaptive neural network (without a reference model) that, in simulation, can reduce vibrations in a scale model F/A-18 vertical tail with varying unmodeled dynamics.

- Testing and simulation of an acceleration feedback controller augmented with an adaptive neural network (without a reference model) that can reduce vibrations in a scale model F/A-18 vertical tail with large debonds.

- A stress distribution model around vibration controlling actuators that shows actuators can reduce local stress.

In this thesis procedures are developed that the acceleration feed back controllers are designed, with sufficient control authority, by using smart structures-based offset piezoceramic stack actuators (OPSA), to control buffet-induced vibrations. The OPSA actuators are designed to provide sufficient control authority to control the buffet induced vibrations in an F/A-18 aircraft. A procedure for optimum placement of these actuators, optimum design of the controllers and minimum number of needed actuators are formulated. With this procedure, a 94% reduction of F/A-18 tail root bending moment at 32 degrees angle of attack and 300psf aerodynamic pressure is demonstrated.

There are many proposed solutions for tail buffet alleviation over the years with only limited results. Linear controllers tuned to control of single or multiple modes in a structure perform very well as long as those modes do not shift. If the modes shift then the required crossover condition is no longer met and the linear controller is less efficient, thus, the reduction is vibration is less. In this thesis, numerical simulation and experiments have clearly shown that a controller with an adaptive neural network has the potential to provide additional reductions in RMS acceleration for tail buffet alleviation. A procedure is developed to augment a linear controller with an adaptive neural network. The adaptive neural network is required in this control scheme to help control vibrations from unmodeled dynamics due to natural frequency shift and delaminations. In this work numerical modeling of a SDOF F/A-18 tail demonstrated that as the first natural frequency shifts from 16.73 Hz to 23 Hz the reduction of measured acceleration is over 95%.

A 1/12th scale F/A-18 wind tunnel model is constructed which included an aeroelastically scaled empennage. An air pulse device is used to dynamically excite the starboard vertical tail which had six OPSA actuators installed at the root of the tail parallel to the elastic axis to control the first bending mode. Two vertical tails are constructed; (1) fully bonded and (2) 30% delamination at the center of the elastic axis. When the tail with the delamination vibrates the delamination can open during each vibration cycle, thus, causing a frequency shift. With the acceleration feedback controller tuned to the first mode root mean square of the measured acceleration is reduced by 66.3%. When the delaminated tail is used the reduction is only 35.5%. When the adaptive neural network is added the RMS reduction of the fully bonded tail is 76.4% and the delaminated tail is 43.9%.

In comparing the results of a single degree of freedom model, air pulse testing, and wind tunnel testing, the reduction in RMS acceleration reduction is much better when the starboard tail is the only structure that is excited. Dynamics from the fuselage, wings, and stinger would have been observed but small enough as to not effect the starboard vertical tail vibration control results. In addition to a new empennage, further wind tunnel tests should be performed in a wind tunnel that is larger for this size wind tunnel model to ensure there are no issues with tunnel blockage. Modified numerical modeling is necessary to

predict the response of any aircraft vertical tail when using OPSAs and the linear/adaptive neural network control scheme. This clearly shows that augmenting a linear controller with an adaptive neural network can significantly help reduce vibrations when structural parameters shift.

In this investigation, a 3-D finite element model is used in combination with a numerical modeling of acceleration feedback control to simulate active damping in a cantilever beam and plate. The simulated beam measured 24 in. $\times$ 0.5 in. $\times$ 2 in. and the plate measured 24 in. $\times$ 0.125 in. $\times$ 8 in.. The issue is whether a bonded vibration control actuator like the OPSA will add stress to the structure it is trying to control. For the beam the longitudinal open loop stress in the area of the actuator was 12 ksi. In the closed loop this stress is reduced to 1.5 ksi. Shear stress in the same area is reduced from 4.3 ksi to 0.55 ksi. For the plate, active control reduces the longitudinal stress in the area of the OPSA from 58 ksi to 8.6 ksi. The shear stress is reduced from 2.85 ksi to 1.3 ksi. This simulation has shown that the stresses within the system are reduced by the use of OPSA based active damping. The control forces and moments induced by the OPSA reduces the local stresses and thus, confirmed the OPSA design as a excellent candidate for stress and vibration reduction solutions for thin-walled structures. This simulation also indicates that a control system based on OPSA actuators and acceleration feedback control is a feasible solution for fatigue life enhancement of thin walled structures.

Future work should include

- Stress reductions in beams and plates when controlling multiple modes. In this case a single mode may not be dominate. Multiple dominate modes would have to be controlled and the corresponding stress around the actuator may become an issue.

- Stress in the area of OPSAs installed on the vertical tail of an F-15 and F/A-18 should be studied. This should include a time history of stress to understand the maximum stress re-distribution when the control force is at maximum.

- Different types of aircraft vertical tails using OPSAs should be used to validate the procedures developed in this research. The vertical tails of high performance aircraft

can very dramatically from aircraft to aircraft (e.g., F-35, F-22, etc..) Each vertical tail should be evaluated as to the effectiveness of the OPSA and associated acceleration feedback/adaptive neural network control can have on the dominate modes.

- Further research is necessary to optimize the geometry of the OPSA mounts to maximize the amount of control moments and reduce any adverse in-plane loads that could shift the frequency of the structure. The geometry of the OPSA end mounts should maximize control moments into the controlled structure and minimize in-plane loading.

- Materials other than the one used in this work such as composites, aluminum, and titanium need to be evaluated to validate these actuators on a wide variety of aerospace applications. Some materials may not be able to withstand local control moments of the OPSAs.

- Wind tunnel testing of the F/A-18 vertical tail using a linear controller augmented by an adaptive neural network should follow. This testing should address the linear controller and neural network gains to be used in all airspeeds and angles of attack where tail buffet occurs. Gain scheduling or hedging may be required so as not to saturate the control scheme but still be effective in controlling tail buffet at all speeds and angles of attack.

- The procedures and adaptive control schemes developed in this work should be extended to multi-mode control in an F/A-18 vertical tail including coupled modes. As mentioned above, multiple modes may dominate vibrations of a vertical tail. To control multiple modes the adaptive neural network will have to be modified to recognize the modes to be controlled.

- Vertical tails with damage such as multiple delaminations should be tested with the linear controller augmented by an adaptive neural network. Damage from combat, maintenance, and environment can cause a variety of damage to the vertical tail. The adaptive neural network should be tested and modified to handle all types of

structural parameter shifts the vertical tail would undergo.

- Finally, aerospace vehicle structures such as wings and other control surfaces that can vibrate should be considered when using a linear controller augmented by an adaptive neural network. Any aerospace structure that does not live out its designed fatigue life can be very expensive to replace and may cause loss of life. The OPSA and associate control scheme is compact and can be used in a variety of locations on an aircraft.

Appendix A

SYSTEM MODEL

A.1 System Model

The free vibration governing equations for a bending-torsion-coupled cantilevered beam are,

$$m(y)\frac{\partial^2 w}{\partial t^2} - mx_\alpha(y)\frac{\partial^2 \theta}{\partial t^2} + \frac{\partial^2}{\partial y^2}(EI(y)\frac{\partial^2 w}{\partial y^2}) = 0 \tag{127}$$

$$-I_\alpha\frac{\partial^2 \theta}{\partial t^2} + mx_\alpha(y)\frac{\partial^2 w}{\partial t^2} + \frac{\partial}{\partial y}(GJ(y)\frac{\partial \theta}{\partial y}) = 0 \tag{128}$$

with boundary conditions

$$at\ y = 0, \qquad w = \frac{\partial w}{\partial y} = \theta = 0 \tag{129}$$

$$at\ y = L, \qquad \frac{\partial^2 w}{\partial y^2} = \frac{\partial^3 w}{\partial y^3} = \frac{\partial \theta}{\partial y} = 0 \tag{130}$$

To study free vibrations, particular solutions in the following forms are used

$$w(y,t) = g_w(y)e^{i\omega t}; \theta(y,t) = g_\theta(y)e^{i\omega t} \tag{131}$$

Equation (131) is substituted into equations (127) and (128), which gives

$$\Big(\frac{d^2}{dy^2}\Big[EI\frac{d^2}{dy^2}\Big] - m\omega^2\Big)g_w(y) + mx_\alpha\omega^2 g_\theta(y) = 0 \tag{132}$$

$$mx_\alpha\omega^2 g_w(y) + \Big(\frac{d}{dy}\Big[GJ\frac{d}{dy}\Big] + I_\alpha\omega^2\Big)g_\theta(y) = 0 \tag{133}$$

To solve equations (132) and (133), $g_w(y)$ and $g_\theta(y)$ are expanded in terms of the corresponding bending and torsion modes to satisfy the boundary conditions in (129) and (130), i.e.,

$$g_w(y) = \sum_{k=1}^{M_1}\Phi_k\alpha_k(y) = \{\boldsymbol{\alpha}(y)\}^T\{\boldsymbol{\Phi}\}, g_\theta(y) = \sum_{k=1}^{M_2}\Theta_k\beta_k(y) = \{\boldsymbol{\beta}(y)\}^T\{\boldsymbol{\Theta}\} \tag{134}$$

where

$$\begin{aligned}
\{\boldsymbol{\Phi}\} &= \{\Phi_1, \cdots, \Phi_{M_1}\}^T \\
\{\boldsymbol{\Theta}\} &= \{\Theta_1, \cdots, \Theta_{M_2}\}^T \\
\{\boldsymbol{\alpha(y)}\} &= \{\alpha_1(y), \cdots, \alpha_{M_1(y)}\}^T \\
\{\boldsymbol{\beta(y)}\} &= \{\beta_1(y), \cdots, \beta_{M_1(y)}\}^T
\end{aligned} \tag{135}$$

where $\alpha_k(y)$ and $\beta_k(y)$ are the k^{th} fundamental modes of uncoupled bending and torsion oscillations of a uniform cantilever beam, respectively. They are given by

$$\beta_k(y) = sin(\frac{2k+1}{2}\frac{\pi}{L}y) \tag{136}$$

$$\alpha_k(y) = -\frac{(sin(\varrho_k)+sinh(\varrho_k))}{(cos(\varrho_k)+cosh(\varrho_k))}\Big(cos(\varrho_k\frac{y}{L})-cosh(\varrho_k\frac{y}{L})\Big)+\Big(sin(\varrho_k\frac{y}{L})-sinh(\varrho_k\frac{y}{L})\Big) \tag{137}$$

where

$$\varrho_k = 1.875, 4.694, ...$$

Equations (134) is substituted into (132) and (133), multiplying (132) and (133) by $\alpha(y)$ and $\beta(y)$ respectively, then integrated with respect to y from 0 to L, gives

$$\begin{bmatrix} \boldsymbol{A}_{11}-\boldsymbol{C}_{11}\omega^2 & \boldsymbol{C}_{12}\omega^2 \\ \boldsymbol{C}_{21}\omega^2 & \boldsymbol{A}_{22}-\boldsymbol{C}_{22}\omega^2 \end{bmatrix}\begin{Bmatrix} \boldsymbol{\Phi} \\ \boldsymbol{\Theta} \end{Bmatrix} = 0 \tag{138}$$

where $\boldsymbol{A}_{11}$ and $\boldsymbol{C}_{11}$ are $M_1 \times M_1$ matrix, $\boldsymbol{C}_{12}$ is a $M_1 \times M_2$ matrix, $\boldsymbol{C}_{21}$ is a $M_2 \times M_1$ matrix, and $\boldsymbol{A}_{22}$ and $\boldsymbol{C}_{22}$ are $M_2 \times M_2$ matrix.

$$A_{11} = \int_0^L \Big(\frac{d^2}{dy^2}\Big[EI\frac{d^2}{dy^2}\{\boldsymbol{\alpha}(y)\}\Big]\{\boldsymbol{\alpha}(y)\}^T dy \qquad [lbs\cdot in] \tag{139}$$

$$A_{22} = -\int_0^L \Big(\frac{d}{dy}\Big[GJ\frac{d}{dy}\{\boldsymbol{\beta}(y)\}\Big]\{\boldsymbol{\beta}(y)\}^T dy \qquad [lbs\cdot in] \tag{140}$$

$$C_{11} = \int_0^L m(y)\{\boldsymbol{\alpha}(y)\}\{\boldsymbol{\alpha}(y)\}^T dy \qquad [slugs\cdot in^2] \tag{141}$$

$$C_{12} = \int_0^L m(y)x_\alpha(y)\{\boldsymbol{\alpha}(y)\}\{\boldsymbol{\beta}(y)\}^T dy \qquad [slugs\cdot in^2] \tag{142}$$

$$C_{22} = \int_0^L I_\alpha(y)\{\boldsymbol{\beta}(y)\}\{\boldsymbol{\beta}(y)\}^T dy \qquad [slugs\cdot in^2] \tag{143}$$

From linear algebra, for a significant solution to exist, the determinant of the coefficient matrix of equation (138) must be zero as shown

$$det\begin{bmatrix} \boldsymbol{A}_{11}-\boldsymbol{C}_{11}\omega^2 & \boldsymbol{C}_{12}\omega^2 \\ \boldsymbol{C}_{21}\omega^2 & \boldsymbol{A}_{22}-\boldsymbol{C}_{22}\omega^2 \end{bmatrix} = 0 \tag{144}$$

this gives a 2M-order characteristic equation as follows.

$$p_M\omega^{2M} + p_{M-1}\omega^{2(M-1)} + \cdots + p_1\omega^2 + p_0 = 0 \tag{145}$$

Table 31: Analytical solutions for the first two modes)

No.	Mode	Frequency	$Eigenvector\{\Phi_1, \Phi_2, \Theta_1, \Theta_2\}^T$
1	$1^{st}bending$	15.01 Hz	{0.9913, -0.0110, 0.1312, 0.0067}
2	$1^{st}torsion$	47.40 Hz	{-0.0612, 0.0009, -0.9980, 0.0161}

where M=$M_1 + M_2$

From equation (145), M real roots for ω^2 are determined. Listing ω^2 in the order starting from the smallest one, the j^{th} positive ω^2 corresponds to the natural frequency of the j^{th} coupled flexure-torsion mode. The corresponding eigenvector is written as $\left\{ \begin{array}{c} \boldsymbol{\Phi} \\ \\ \boldsymbol{\Theta} \end{array} \right\}$ (j=1, 2,..., M), can also be determined from equation (138).

If only the first N coupled modes ($N \leq M$) are of interest, the corresponding mode information, including the natural frequency matrix and eigenvector matrix, is written as follows.

$$\begin{aligned} [\boldsymbol{\omega}^2] &= diag\left[\omega_1^2, \omega_2^2, \ldots, \omega_N^2\right]_{N\times N} \\ [\boldsymbol{\Phi}] &= [\Phi^1 \cdots \Phi^N]_{1\times N}^T \\ [\boldsymbol{\Theta}] &= [\Theta^1 \cdots \Theta^N]_{1\times N}^T \end{aligned} \tag{146}$$

They satisfy the following relations as,

$$\left(\begin{array}{c} [\boldsymbol{A}_{11}][\boldsymbol{\Phi}] \\ [\boldsymbol{A}_{22}][\boldsymbol{\Theta}] \end{array} \right) = \left(\begin{array}{c} [\boldsymbol{C}_{11}][\boldsymbol{\Phi}] - [\boldsymbol{C}_{12}][\boldsymbol{\Theta}] \\ -[\boldsymbol{C}_{21}][\boldsymbol{\Phi}] - [\boldsymbol{C}_{22}][\boldsymbol{\Theta}] \end{array} \right) [\boldsymbol{\omega}^2] \tag{147}$$

The j^{th} coupled flexural-torsional mode shape of the tail, $g^j(x, y)$, is written as

$$g^j(x, y) = g_w^j(y) + x g_\theta^j(y) = \{\boldsymbol{\alpha}(y)\}^T\{\boldsymbol{\Phi}^j\} + x\{\boldsymbol{\beta}(y)\}^T\{\boldsymbol{\Theta}^j\} \tag{148}$$

For a F/A-18 vertical tail, average x_α is small, therefore the 1^{st} flexure-torsion mode varies little from the 1st bending mode, and the 2^{nd} flexure-torsion mode varies little from the 1st torsion mode. By choosing M=2, and using the distributions of mass, bending stiffness, and torsional stiffness for a F/A-18 vertical tail from reference[47], the first two natural frequencies are calculated and shown in Table 31.

A.1.1 Generalized Aerodynamic Modal Loads[47]

If the distribution of differential pressure $\Delta p(x, y, t)$ is measured, the generalized aerodynamic modal loads for the i^{th} mode is obtained as

$$\Xi_i(t) = \int_A \int \Delta p(x, y, t) g^i(x, y) dx dy \qquad i = 1, 2, 3, \ldots \tag{149}$$

If the acceleration at a point is measured, the generalized aerodynamic modal loads for the i^{th} mode is obtained as

$$\Xi_i(t) = \int_A \int \frac{m}{A} \frac{\partial^2 \overline{w}(x, y, t)}{\partial t^2} \delta(x - x_a) \delta(y - y_a) g^i(x, y) dx dy \qquad i = 1, 2, 3, \ldots \tag{150}$$

The auto-correlation of the i^{th} modal load is calculated as

$$R_{ii}(t) = \int_{-\infty}^{t} \Xi_i(t - \tau) \Xi_i(\tau) d\tau \qquad i = 1, 2, 3, \ldots \tag{151}$$

If 100% spatially correlation is assumed, then the correlation between any two locations (x,y) and $(\hat{x}, \hat{y})$ is the same. For measured pressure differential this is

$$\boldsymbol{R}_{(x,y)(\hat{x},\hat{y})}(t) = \int_{-\infty}^{t} \Delta p(x, y, t - \tau) \Delta p(\hat{x}, \hat{y}, \tau) d\tau = \boldsymbol{R}(t) \tag{152}$$

For measured acceleration at a point this is

$$\begin{aligned} &\boldsymbol{R}_{(x,y)(\hat{x},\hat{y})}(t) \\ &= \textstyle\int_{-\infty}^{t} \frac{m}{A} \left[\frac{\partial^2 \overline{w}(x,y,t-\tau)}{\partial \tau^2} \delta(x - x_a) \delta(y - y_a) \frac{\partial^2 \overline{w}(\hat{x},\hat{y},\tau)}{\partial \tau^2} \delta(\hat{x} - \hat{x}_a) \delta(\hat{y} - \hat{y}_a) \right] d\tau \\ &= \boldsymbol{R}(t) \end{aligned} \tag{153}$$

It is noted that the notations for the modal correlation and position correlation are distinguish by a normal-faced and a bold-faced "R". PSD of position correlation is denoted by bold-faced letters **PSD**, which is made difference from normal letters PSD for modal correlation. Therefore, the correlation of the i^{th} modal load, for measured pressure differential, is obtained by

$$\begin{aligned} R_{ii}(t) &= \textstyle\int_{-\infty}^{t} \Big(\int_A \int \Delta p(x, y, t - \tau) g^i(x, y) dx dy \Big) \Big(\int_A \int \Delta p(\hat{x}, \hat{y}, \tau) g^i(\hat{x}, \hat{y}) dx dy \Big) d\tau \\ &= \textstyle\int_A \int \int_A \int \Big(\int_{-\infty}^{t} \Delta p(x, y, t - \tau) \Delta p(\hat{x}, \hat{y}, \tau) d\tau \Big) g^i(\hat{x}, \hat{y}) g^i(x, y) d\hat{x} d\hat{y} dx dy \\ &= \textstyle\int_A \int \int_A \int \boldsymbol{R}(t) g^i(\hat{x}, \hat{y}) g^i(x, y) d\hat{y} dx dy = \boldsymbol{R}(t) \Big(\int_A \int g^i(\hat{x}, \hat{y}) d\hat{x} d\hat{y} \Big)^2 \end{aligned} \tag{154}$$

The correlation of the i^{th} modal load, for measured acceleration at a point, is obtained by

$$\begin{aligned}
&R_{ii}(t) = \int_{-\infty}^{t} \Big(\int_A \int \tfrac{m}{A} \tfrac{\partial^2 \overline{w}(x,y,t-\tau)}{\partial \tau^2} \delta(x-x_a)\delta(y-y_a) g^i(x,y) dx dy \Big) \\
&\Big(\int_A \int \tfrac{m}{A} \tfrac{\partial^2 \overline{w}(\hat{x},\hat{y},\tau)}{\partial \tau^2} \delta(\hat{x}-\hat{x}_a)\delta(\hat{y}-\hat{y}_a) g^i(\hat{x},\hat{y}) d\hat{x} d\hat{y} \Big) d\tau \\
&= \int_A \int \int_A \int \Big(\int_{-\infty}^{t} \tfrac{m}{A} \Big[\tfrac{\partial^2 \overline{w}(x,y,t-\tau)}{\partial \tau^2} \delta(x-x_a)\delta(y-y_a) \tfrac{\partial^2 \overline{w}(\hat{x},\hat{y},\tau)}{\partial \tau^2} \delta(\hat{x}-\hat{x}_a)\delta(\hat{y}-\hat{y}_a) \Big] g^i(x,y) d\hat{x} d\hat{y} dx dy \\
&= \int_A \int \int_A \int \boldsymbol{R}(t) g^i(\hat{x},\hat{y}) g^i(x,y) d\hat{y} dx dy = \boldsymbol{R}(t) \Big(\int_A \int g^i(\hat{x},\hat{y}) d\hat{x} d\hat{y} \Big)^2
\end{aligned} \tag{155}$$

Then, the PSD of the i^{th} modal load is obtained by

$$PSD_i(\omega) = \int_{\infty}^{-\infty} R_{ii}(t) e^{-j\omega t} dt = \boldsymbol{PSD}(\omega) \Big(\int_A \int g^i(\hat{x},\hat{y}) d\hat{x} d\hat{y} \Big)^2 \tag{156}$$

In the above equations, $g^i(x,y)$ can be replaced by an arbitrary weighting function g(x,y) to determine the associated generalized aerodynamic loading.

A.1.2 Controller Design: Crossover Point Theory[32]

A crossover point, i.e. a single natural frequency resulting for the two degrees of freedom system in equation (26), is obtained when the roots of the closed-loop characteristic equation, i.e. the denominator of equation (37), are repeated complex conjugate pairs. It yields,

$$(s^2 + 2\zeta_1\omega_1 s + \omega_1^2)(s^2 + 2\zeta_{c1}\omega_{c1} s + \omega_{c1}^2) + \gamma_1 \omega_{c1}^2 n_s^1 \overline{a}\overline{b} s^2 = (s^2 + 2\zeta_f \omega_f s + \omega_f^2)^2 \tag{157}$$

where ω_f and ζ_f are the natural frequency and damping ratio of the closed-loop system, respectively. There are five unknowns ζ_{c1}, ω_{c1}, γ_1, ω_f, ζ_f. Equating the coefficients in the power of s,

$$\begin{aligned}
&\zeta_1\omega_1 + \zeta_{c1}\omega_{c1} = 2\zeta_f\omega_f \\
&\omega_1^2 + \omega_{c1}^2 + 4\zeta_{c1}\omega_{c1}\zeta_1\omega_1 + \omega_{c1}^2\gamma_1 n_s^1 \overline{a}\overline{b} = 2\omega_f^2 + 4\zeta_f^2\omega_f^2 \\
&\zeta_{c1}\omega_1 + \zeta_1\omega_{c1} = 2\xi_f\omega_f \\
&\omega_1\omega_{c1} = \omega_f^2
\end{aligned} \tag{158}$$

A practical choice of parameters to satisfy equation (158) is

$$\begin{aligned}
&\omega_{c1} = \omega_f = \omega_1 \\
&\zeta_f = \tfrac{\zeta_{c1}+\zeta_1}{2} \\
&\gamma_1 n_s^1 = \tfrac{(\zeta_{c1}-\zeta_1)^2}{\overline{a}\overline{b}}
\end{aligned} \tag{159}$$

The controller and closed-loop system have the same frequency as the open-loop system ω_1. Since the damping of the open-loop system is usually quite small about 0.1-0.2% [4][64][65], the damping of the closed loop system can be significantly increased by designing large controller damping. From equation (159), the desired controller gain is proportional to the selected controller damping, and is reduced by increasing the generalized flexibility influence parameters of the actuator and sensor $\overline{a}$ and $\overline{b}$, or by increasing the number of the stacks. From equations (36) and 37), the ratio of response spectrum of the closed-loop system to that of the open-loop system is obtained.

$$\left|\frac{\Xi_1^{closed}(j\omega)}{\Xi_1^{open}(s)}\right|^2 = \left|\frac{(s^2+2\zeta_1\omega_1 s+\omega_1^2)(s^2+2\zeta_1\omega_1 s+\omega_1^2)}{(s^2+2\zeta_1\omega_1 s+\omega_1^2)(s^2+2\zeta_{c1}\omega_{c1} s+\omega_{c1}^2)+\gamma_1\omega_{c1}^2 n_s^1 \overline{a}\overline{b}s^2}\right|^2 \tag{160}$$

At the worst scenario $\omega = \omega_1$, after considering the conditions in equations (157, 159), the reduction of the closed-loop response is calculated by

$$\delta = 1 - \left|\frac{\Xi_1^{closed}(j\omega)}{\Xi_1^{open}(s)}\right|^2 = 1 - \left|\frac{4\zeta_1\zeta_{c1}}{(\zeta_{c1}+\zeta_1)^2}\right|^2 \tag{161}$$

Appendix B

ABAQUS 5.8 INPUT FILE OF CANTILEVER BEAM CONTROLLED BY ACCELERATION FEEDBACK CONTROL AND AN OPSA

```
*HEADING
 Closed loop model of a Cantilever beam with springs and Dload instead of stack
**
** Coordinates are in inches
**
*NODE
 1,     0.,0.,0.
 193,   0.,0.,24.
 1601,  2.,0.,0.
 1793,  2.,0.,24.
 8001,  0.,0.5,0.
 8193,  0.,0.5,24.
 9601,  2.,0.5,0.
 9793,  2.,0.5,24.
*NODE,NSET=MNT1U
 16405,  0.5,1.5,0.5
 16413,  0.5,1.5,1.5
 17205,  1.5,1.5,0.5
 17213,  1.5,1.5,1.5
*NODE,NSET=MNT2U
 16421,  0.5,1.5,2.5
 16425,  0.5,1.5,3.0
 17221,  1.5,1.5,2.5
```

```
 17225,  1.5,1.5,3.0
*NODE, NSET=MNT1STCK
 19000,  0.902,1.098,1.55
 19001,  1.098,1.098,1.55
 19002,  1.098,0.902,1.55
 19003,  0.902,0.902,1.55
*NODE, NSET=MNT2STCK
 19010,  0.902,1.098,2.45
 19011,  1.098,1.098,2.45
 19012,  1.098,0.902,2.45
 19013,  0.902,0.902,2.45
*NODE, NSET=DBLK1
 19004,  0.902,1.098,1.60
 19005,  1.098,1.098,1.60
 19006,  1.098,0.902,1.60
 19007,  0.902,0.902,1.60
*NODE, NSET=DBLK2
 19014,  0.902,1.098,2.40
 19015,  1.098,1.098,2.40
 19016,  1.098,0.902,2.40
 19017,  0.902,0.902,2.40
**
** Create nodes for beam
**
*NGEN,NSET=FIX1
 1,1601,200
*NGEN,NSET=FIX2
 8001,9601,200
*NFILL,NSET=FIX
```

```
 FIX1,FIX2,4,2000
*NGEN,NSET=END1
 193,1793,200
*NGEN,NSET=END2
 8193,9793,200
*NFILL,NSET=END
 END1,END2,4,2000
*NFILL,NSET=CBEAM
 FIX,END,192,1
**
** Create nodes for mount1
**
*NSET,NSET=MNT1BC1
 8405,8605,8805,9005,9205
*NGEN,NSET=MNT1BC2
 16405,17205,200
*NFILL,NSET=MNT1BCA
 MNT1BC1,MNT1BC2,4,2000
*NSET,NSET=MNT1BC3
 8413,8613,8813,9013,9213
*NGEN,NSET=MNT1BC4
 16413,17213,200
*NFILL,NSET=MNT1BCB
 MNT1BC3,MNT1BC4,4,2000
*NFILL,NSET=MOUNT1
 MNT1BCA,MNT1BCB,4,2
**
** Create nodes for mount2
**
```

```
*NSET,NSET=MNT2BC1
 8421,8621,8821,9021,9221
*NGEN,NSET=MNT2BC2
 16421,17221,200
*NFILL,NSET=MNT2BCA
 MNT2BC1,MNT2BC2,4,2000
*NSET,NSET=MNT2BC3
 8425,8625,8825,9025,9225
*NGEN,NSET=MNT2BC4
 16425,17225,200
*NFILL,NSET=MNT2BCB
 MNT2BC3,MNT2BC4,4,2000
*NFILL,NSET=MOUNT2
 MNT2BCA,MNT2BCB,2,2
**
*NSET, NSET=SENSOR
 8993
**
** Make master elements for beam and mounts
**
*ELEMENT,TYPE=C3D20R
 1, 1,401,4401,4001, 5,405,4405,4005, 201,2401,4201,2001,
     205,2405,4205,2005, 3,403,4403,4003
 4000, 8405,8805,12805,12405, 8409,8809,12809,12409,
      8605,10805,12605,10405, 8609,10809,12609,10409, 8407,8807,12807,12407
 4200, 8421,8821,12821,12421, 8425,8825,12825,12425,
      8621,10821,12621,10421, 8625,10825,12625,10425, 8423,8823,12823,12423
**
** Create elements for beam
```

```
**
*ELGEN,ELSET=CBEAM
 1,4,400,1,48,4,10,2,4000,2000
*ELSET, ELSET=LOCSTRESS
 2,3,12,22,32,42,52,62,13,23,33,43,53,63,2002,2003
 2012,2022,2032,2042,2052,2062,2013,2023,2033,2043,2053,2063
**
** Create elements for mounts
**
*ELGEN,ELSET=MOUNT1
 4000,2,400,1,2,4,10,2,4000,100
*ELGEN,ELSET=MOUNT2
 4200,2,400,1,1, , ,2,4000,100
*ELEMENT,TYPE=C3D4,ELSET=MNT1STCK
 5000, 12813,13013,14813,19001
 5001, 12813,14813,12613,19000
 5002, 12813,12613,10813,19003
 5003, 12813,10813,13013,19002
*ELEMENT,TYPE=C3D4,ELSET=MNT2STCK
 5010, 12821,12621,14821,19010
 5011, 12821,14821,13021,19011
 5012, 12821,13021,10821,19012
 5013, 12821,10821,12621,19013
*ELEMENT,TYPE=C3D8R,ELSET=DLBLK
 16000,19003,19002,19001,19000,19007,19006,19005,19004
 16001,19017,19016,19015,19014,19013,19012,19011,19010
*ELSET,ELSET=MTBEAM
 CBEAM,MOUNT1,MOUNT2,MNT1STCK,MNT2STCK,DLBLK
**
```

```
** Create spring elements
**
*ELEMENT,TYPE=SPRING2,ELSET=SPRINGS
 20001,19004,19014
 20002,19005,19015
 20003,19006,19016
 20004,19007,19017
**
** spring stiffness is in lbf/in
**
*SPRING,ELSET=SPRINGS
 3,3
 109543.4392959
**
** Material properties for steel
**
*SOLID SECTION,MATERIAL=STEEL,ELSET=MTBEAM
*MATERIAL,NAME=STEEL
**
** Youngs modulus is in lbf/in^2
**
*ELASTIC
 29.E6,0.3
**
** Density is in lbf*sec^2/in^4
**
*DENSITY
 0.0007355
**
```

```
** The following raleigh damping is based on 1.5% damping
**
*DAMPING, ALPHA=4.8280, BETA=2.2596E-5
**
**
*BOUNDARY
 FIX1,ENCASTRE
 FIX2,ENCASTRE
 2001,ENCASTRE
 4001,ENCASTRE
 6001,ENCASTRE
 3601,ENCASTRE
 5601,ENCASTRE
 7601,ENCASTRE
*AMPLITUDE, DEFINITION=PERIODIC, NAME=LOADAMP, TIME=TOTAL TIME
 1,187.38,0.0,0.0
 0.,1.
*USER SUBROUTINES
      SUBROUTINE URDFIL(LSTOP,LOVRWRT,KSTEP,KINC,DTIME,TIME)
C
      INCLUDE 'ABA_PARAM.INC'
c
      COMMON /ACC/ ACCEL
C
      DIMENSION ARRAY(513),JRRAY(NPRECD,513),TIME(2)
      EQUIVALENCE (ARRAY(1),JRRAY(1,1))
c
 200  FORMAT(1X,'Acceleration at node',I5,1x,
     &'in the y-direction = ',F11.2)
```

```
C
C FIND CURRENT INCREMENT.
C
      CALL POSFIL(KSTEP,KINC,ARRAY,JRCD)
      DO K1=1,999999
         CALL DBFILE(0,ARRAY,JRCD)
         IF (JRCD .NE. 0) GO TO 210
         KEY=JRRAY(1,2)
C
C RECORD 103 CONTAINS VALUES FOR ACCELERATION
C
         IF (KEY.EQ.103) THEN
               ACCEL = ARRAY(5)
               WRITE(6,200)ARRAY(3),ACCEL
               WRITE(7,200)ARRAY(3),ACCEL
         END IF
       END DO
 210  CONTINUE
      RETURN
      END
c
      SUBROUTINE DLOAD (F,KSTEP,KINC,TIME,NOEL,NPT,LAYER,KSPT,
     &                  COORDS,JLTYP)
c
      INCLUDE 'ABA_PARAM.INC'
c
      COMMON /ACC/ ACCEL
c
      DIMENSION TIME(2),COORDS(3)
```

```
      REAL RKH,G,wc,zc,Clamdac,Comegac,x1(6000),x2(6000)
c
 100  FORMAT(1X,'ACCEL in DLOAD is = ',F11.2)
      WRITE(6,100)ACCEL
      WRITE(7,100)ACCEL
c
      RKH = 0.001
      G = -2.5
      wc = 187.38
      zc = 0.144075
      Clamdac = 2.*zc*wc
      Comegac = wc*wc
      KSTEP1INC = 5000
c
      If(KSTEP.EQ.1 .AND. KINC.EQ.1)THEN
         x1(1) = 0.
         x2(1) = 0.
         F = -1*G*Comegac*x2(KINC)
      ELSE IF(KSTEP.EQ.1 .AND. KINC.GT.1)THEN
C
C     This will numerically integrate using RK5
c
      v = x1(KINC-1)
      u = x2(KINC-1)
      RK11 = RKH*(ACCEL-Clamdac*v-Comegac*u)
      RK12 = RKH*v
C
      v = x1(KINC-1)+RK11/4.
      u = x2(KINC-1)+RK12/4.
```

```
      RK21 = RKH*(ACCEL-Clamdac*v-Comegac*u)
      RK22 = RKH*v
C
      v = x1(KINC-1)+3./32.*RK11+9./32.*RK21
      u = x2(KINC-1)+3./32.*RK12+9./32.*RK22
      RK31 = RKH*(ACCEL-Clamdac*v-Comegac*u)
      RK32 = RKH*v
C
      v = x1(KINC-1)+1932./2197.*RK11-7200./2197.*RK21
     &+7296./2197.*RK31
      u = x2(KINC-1)+1932./2197.*RK12-7200./2197.*RK22
     &+7296./2197.*RK32
      RK41 = RKH*(ACCEL-Clamdac*v-Comegac*u)
      RK42 = RKH*v
C
      v = x1(KINC-1)+439./216.*RK11-8.*RK21
     &+3680./513.*RK31-845./4104.*RK41
      u = x2(KINC-1)+439./216.*RK12-8.*RK22
     &+3680./513.*RK32-845./4104.*RK42
      RK51 = RKH*(ACCEL-Clamdac*v-Comegac*u)
      RK52 = RKH*v
C
      v = x1(KINC-1)-8./27.*RK11+2.*RK21-3544./2565.*RK31
     &+1859./4104.*RK41-11./40.*RK51
      u = x2(KINC-1)-8./27.*RK12+2.*RK22-3544./2565.*RK32
     &+1859./4104.*RK42-11./40.*RK52
      RK61 = RKH*(ACCEL-Clamdac*v-Comegac*u)
      RK62 = RKH*v
C
```

```
      x1(KINC) = x1(KINC-1)+16./135.*RK11+6656./12825.*RK31
     &+28561./56430.*RK41-9./50.*RK51+2./55.*RK61
      x2(KINC) = x2(KINC-1)+16./135.*RK12+6656./12825.*RK32
     &+28561./56430.*RK42-9./50.*RK52+2./55.*RK62
C
      F = -1*G*Comegac*x2(KINC)
      ELSE
C
C     This will numerically integrate using RK5
C     for the second step
c
      v = x1(KINC+KSTEP1INC-1)
      u = x2(KINC+KSTEP1INC-1)
      RK11 = RKH*(ACCEL-Clamdac*v-Comegac*u)
      RK12 = RKH*v
C
      v = x1(KINC+KSTEP1INC-1)+RK11/4.
      u = x2(KINC+KSTEP1INC-1)+RK12/4.
      RK21 = RKH*(ACCEL-Clamdac*v-Comegac*u)
      RK22 = RKH*v
C
      v = x1(KINC+KSTEP1INC-1)+3./32.*RK11+9./32.*RK21
      u = x2(KINC+KSTEP1INC-1)+3./32.*RK12+9./32.*RK22
      RK31 = RKH*(ACCEL-Clamdac*v-Comegac*u)
      RK32 = RKH*v
C
      v = x1(KINC+KSTEP1INC-1)+1932./2197.*RK11-7200./2197.*RK21
     &+7296./2197.*RK31
      u = x2(KINC+KSTEP1INC-1)+1932./2197.*RK12-7200./2197.*RK22
```

```
     &+7296./2197.*RK32
      RK41 = RKH*(ACCEL-Clamdac*v-Comegac*u)
      RK42 = RKH*v
C
      v = x1(KINC+KSTEP1INC-1)+439./216.*RK11-8.*RK21
     &+3680./513.*RK31-845./4104.*RK41
      u = x2(KINC+KSTEP1INC-1)+439./216.*RK12-8.*RK22
     &+3680./513.*RK32-845./4104.*RK42
      RK51 = RKH*(ACCEL-Clamdac*v-Comegac*u)
      RK52 = RKH*v
C
      v = x1(KINC+KSTEP1INC-1)-8./27.*RK11+2.*RK21-3544./2565.*RK31
     &+1859./4104.*RK41-11./40.*RK51
      u = x2(KINC+KSTEP1INC-1)-8./27.*RK12+2.*RK22-3544./2565.*RK32
     &+1859./4104.*RK42-11./40.*RK52
      RK61 = RKH*(ACCEL-Clamdac*v-Comegac*u)
      RK62 = RKH*v
C
      x1(KINC+KSTEP1INC) = x1(KINC+KSTEP1INC-1)+16./135.*RK11
     &+6656./12825.*RK31+28561./56430.*RK41-9./50.*RK51+2./55.*RK61
      x2(KINC+KSTEP1INC) = x2(KINC+KSTEP1INC-1)+16./135.*RK12
     &+6656./12825.*RK32+28561./56430.*RK42-9./50.*RK52+2./55.*RK62
C
      F = -1*G*Comegac*x2(KINC+KSTEP1INC)
c
      ENDIF
C
      write(6,150)KSTEP,KINC,F
      write(7,150)KSTEP,KINC,F
```

```
 150  FORMAT('At KSTEP =',I5,1x,'and KINC =',I5,1x,'F =',F15.5)
c
      RETURN
      END
*****
*STEP,INC=5000
 Dynamic Analysis without Stress
*DYNAMIC
 0.001,5.0
*DLOAD,OP=NEW
 16000,P2NU
 16001,P1NU
**
** loading is in lbf for CLOAD
**
*CLOAD, AMPLITUDE=LOADAMP, OP=NEW
 8993, 2, -0.9
*OUTPUT, HISTORY, FREQUENCY=1
*NODE OUTPUT, NSET=SENSOR
 U
 A
*OUTPUT, FIELD, FREQUENCY=0
*RESTART, WRITE, OVERLAY
*EL PRINT, FREQUENCY=0
*NODE PRINT, FREQUENCY=0
*NODE FILE, NSET=SENSOR, FREQUENCY=1
 U
 A
*END STEP
```

```
**
*STEP, INC=150
 Dynamic Analysis with Stresses
*DYNAMIC, INITIAL=NO
 0.001, 0.15
*OUTPUT, HISTORY, OP=ADD, FREQUENCY=1
*NODE OUTPUT, NSET=SENSOR
 U
 A
*ELEMENT OUTPUT, ELSET=LOCSTRESS
 S
 COORD
*OUTPUT, FIELD, FREQUENCY=1
*ELEMENT OUTPUT
 S
*RESTART, WRITE, FREQUENCY=1
*EL PRINT, FREQUENCY=0
*EL FILE, FREQUENCY=1
 S
*NODE PRINT, FREQUENCY=0
*NODE FILE, NSET=SENSOR, FREQUENCY=1
 U
 A
*END STEP
```

Appendix C

CANTILEVER BEAM MODEL

In 2000 Maxime Bayon De Noyer[71] successfully used an experimental cantilever beam to develop the acceleration feedback controller that was later modified to develop a model for the F-15 vertical tail and to reduce buffet induced vibrations in a F-15 vertical tail. In his research, two offset piezoceramic stack actuators (OPSA) were installed on one side of the beam. The first OPSA was installed near the fixed end of the cantilever beam and was used to control the beam vibrations. The second OPSA was installed next to the first OPSA as seen in Figure (98) and was used to create disturbance moments. To control the first mode of the beam vibrations, an acceleration feedback controller was designed. The results of this experiment showed a significant reduction of RMS acceleration in the first mode.

In this chapter, the cantilever beam model is refined so that the linear acceleration feedback controller is augmented with an adaptive neural network to accommodate unmodeled dynamics in the plant model.

An Euler-Bernoulli model for the beam (Figure (114) is given as follows

$$\begin{aligned} &EI\frac{\partial^4 v}{\partial v^4} + A\rho\frac{\partial^2 v}{\partial t^2} + \frac{\partial}{\partial x}[M_c(t)\delta(x-L_1)] - \frac{\partial}{\partial x}[M_c(t)\delta(x-(L_2))] \\ &+\frac{\partial}{\partial x}[M_d(t)\delta(x-(L_3)] - \frac{\partial}{\partial x}[M_d(t)\delta(x-(L_4))] = 0 \end{aligned} \tag{162}$$

where the x-axis is along the longitudinal axis of the beam, E is the Youngs modulus of the beam, I is the beam moment of inertia, A is the beam cross-sectional area, ρ is the beam material density, M_c is the control moment (See Figure 114), M_d is the disturbance moment OPSA, F_s is the induced force by the stack, L_1 is the distance from the base of the beam to the first OPSA mount along the x-axis, and L_2 is the length of the stack. It is assumed that the beam has constant height and width.

The final solution can be assumed to come from a separation of variables form as follows

$$v = \sum_{i=1}^{N} \phi_i(x)\xi_i(t) \tag{163}$$

where $\phi(x)$ is the mode shape and $\xi(t)$ is the time portion. Bayon de Noyer et al.[15] derived an approximate equivalent stiffness of the piezoceramic stack as

$$k_s = \frac{A_s Y_s^E}{L_2} \tag{164}$$

$$k^e = \frac{A_s Y_s^E d_{33}}{t_{layer}} \tag{165}$$

where A_s is the stack cross-sectional area, t_{layer} is the thickness of one piezoceramic layer in a stack, d_{33} is the out of plane coefficient for the piezoceramic material, and Y_s^E is the Youngs modulus of the stack. Piezoceramic stacks use the direct d_{33} piezoelectric coefficient instead of the transverse d_{31} coefficient used in wafers.

In the OPSA system, the piezoceramic stack is capable of rotating in the support mounts but is not allowed to bend or twist during the deformation of the structure. This means that the stack is allowed only to extend or contract during the deformation of the structure. The contact with the structure is assumed to be through a pre-compression of the piezoceramic stack in OPSA. This pre-compression is from the compression bolt as shown in Figure (3) and the applied field. Because all individual layers in a piezoceramic stack are subjected to the same voltage, a uniform axial strain is assumed. The axial deformation of piezoceramic stack is associated with the deformation of the structural surface. This derivation assumes that the beam is mounted with ideally fixed supports and the stack is always in contact with the mounts. Therefore, the total moment M applied at the mounts is the sum of the applied force of the stack plus the force due to the stiffness of the stack (See Figure 114).

$$M_c(t) = h\left(F(t) + k_s h\left(-\frac{\partial v(L_1,t)}{\partial x} + \frac{\partial v(L_2,t)}{\partial x}\right)\right) \tag{166}$$

$$M_d(t) = h\left(F(t) + k_s h\left(-\frac{\partial v(L_3,t)}{\partial x} + \frac{\partial v(L_4,t)}{\partial x}\right)\right) \tag{167}$$

where h is the offset distance of the stack.

The electric field is assumed uniform and the effects of the spontaneous electric field are considered to be negligible. With these assumptions, the axial force is given to be

$$F_s(t) = -A_s Y_s^E d_{33} E_{field}(t) \tag{168}$$

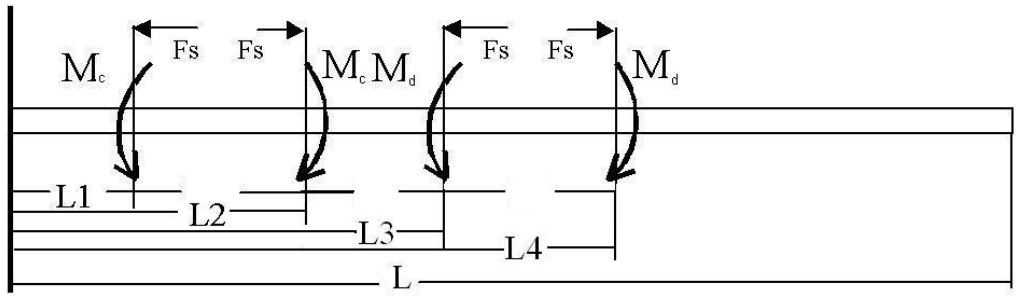

Figure 114: Moments applied by OPSA

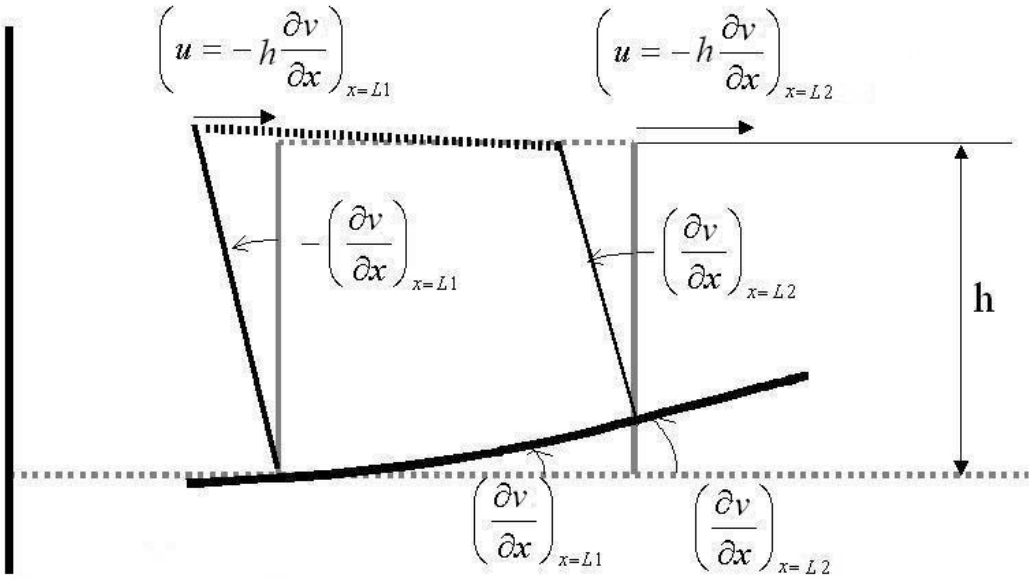

Figure 115: Displacement of OPSA mounts

In this equation, $E_{field}(t)$ is equal to the ratio of the control signal voltage over the thickness of each PZT layer. The expression for $E_{field}(t)$ is

$$E_{field}(t) = \frac{V_c(t)}{t_{layer}} = \frac{\gamma_i \alpha \eta_i(t)}{t_{layer}} \tag{169}$$

where $V_c(t)$ is the applied control voltage, γ_i is the controller gain, and α is the transduction constant. In the frequency domain this becomes

$$\bar{E}_{field}(s) = \frac{\gamma_i \alpha \omega^2 \bar{\eta}_i(s)}{t_{layer}} \tag{170}$$

The boundary conditions of the beam are as follows.

$$v(0,t) = 0 \tag{171}$$

$$\frac{\partial v}{\partial x}(0,t) = 0 \tag{172}$$

$$EI\frac{\partial^2 v}{\partial x^2}(L,t) = 0 \tag{173}$$

$$EI\frac{\partial^3 v}{\partial x^3}(L,t) = 0 \tag{174}$$

C.1 Open loop response for the cantilever beam

Specifically for this analysis, the open loop system is written using eqn. (162) as

$$EIv^{IV} + m\ddot{v} + \frac{\partial}{\partial x}[M_d(t)\delta(x-(L_3)] - \frac{\partial}{\partial x}[M_d(t)\delta(x-(L_4))] = 0 \tag{175}$$

The solution for the open loop beam displacement w(x,t) of the first mode is obtained using the Galerkin method. By using cantilever mode shape as a trial function eqn. (175) is given as

$$\begin{aligned} &EI\xi(t)\phi''''(x) + m\phi(x)\ddot{\xi}(t) \\ &+\tfrac{\partial}{\partial x}\left[h\left(F_d(t) + \xi(t)k_s h\left(\phi'(L4) - \phi'(L3)\right)\right)\delta\left(x - L3\right)\right] \\ &-\tfrac{\partial}{\partial x}\left[h\left(F_d(t) + \xi(t)k_s h\left(\phi'(L4) - \phi'(L3)\right)\right)\delta\left(x - L4\right)\right] = 0 \end{aligned} \tag{176}$$

To simplify equation (176) the following constant is defined

$$\Psi_2 = k_s h\left(\phi'(L4) - \phi'(L3)\right) \tag{177}$$

Rewriting equation (176) with the constants in eqn. (177) gives

$$\begin{aligned} &EI\xi(t)\phi''''(x) + m\phi(x)\ddot{\xi}(t) \\ &+\tfrac{\partial}{\partial x}\left[h\left(F_d(t) + \xi(t)\Psi_2\right)\delta\left(x - L3\right)\right] \\ &-\tfrac{\partial}{\partial x}\left[h\left(F_d(t) + \xi(t)\Psi_2\right)\delta\left(x - L4\right)\right] = 0 \end{aligned} \tag{178}$$

If it assumed that the trial and testing functions are the first cantilever mode shapes

$$\tilde{w} = \frac{dv(x,t)}{d\xi(t)} = \phi(x) \tag{179}$$

where $\phi(x)$ is the first mode of the cantilever beam which satisfies the boundary conditions.

The error function is multiplied by (179) and integrated over the length of the beam to give

$$\begin{aligned} &m\int_0^L \phi^2(x)dx\ddot{\xi}(t) + \left(EI\int_0^L \phi(x)\phi''''(x)dx + \Psi_2\Psi_4\right)\xi(t) \\ &= -h\Psi_4 F_d(t) \end{aligned} \tag{180}$$

where

$$\Psi_4 = \phi'(L3) - \phi'(L4) \tag{181}$$

Rearranging eqn. (180)

$$\ddot{\xi}(t) + \frac{\left(EI \int_0^L \phi(x)\phi''''(x)dx + \Psi_2\Psi_4 \right)}{m \int_0^L \phi^2(x)dx}\xi(t) = -\frac{h\Psi_4}{m \int_0^L \phi^2(x)dx}F_d(t) \tag{182}$$

C.2 Closed loop of cantilever beam

For the closed loop development the linear controller design will be derived first then the augmentation from the adaptive neural network will follow. In this development, only acceleration from the plant is measured for control. It is assumed that the plant is internally stable when perfect tracking or regulation is achieved. In order to solve equation (162) using the Galerkin method and the cantilever beam mode shape as in the open loop the following is obtained

$$\begin{aligned}
&EI\xi(t)\phi''''(x) + m\phi(x)\ddot{\xi}(t) \\
&+\tfrac{\partial}{\partial x}\left[h\left(F_c(t) + \xi(t)k_s h\left(\phi'(L2) - \phi'(L1)\right)\right)\delta\left(x - L1\right)\right] \\
&-\tfrac{\partial}{\partial x}\left[h\left(F_c(t) + \xi(t)k_s h\left(\phi'(L2) - \phi'(L1)\right)\right)\delta\left(x - L2\right)\right] \\
&+\tfrac{\partial}{\partial x}\left[h\left(F_d(t) + \xi(t)k_s h\left(\phi'(L4) - \phi'(L3)\right)\right)\delta\left(x - L3\right)\right] \\
&-\tfrac{\partial}{\partial x}\left[h\left(F_d(t) + \xi(t)k_s h\left(\phi'(L4) - \phi'(L3)\right)\right)\delta\left(x - L4\right)\right] = 0
\end{aligned} \tag{183}$$

To simplify equation (183) the following constant is defined

$$\Psi_1 = k_s h\left(\phi'(L2) - \phi'(L1)\right) \tag{184}$$

Rewriting equation (183) with the constants in eqn. (184) gives

$$\begin{aligned}
&EI\xi(t)\phi''''(x) + m\phi(x)\ddot{\xi}(t) \\
&+\tfrac{\partial}{\partial x}\left[h\left(F_c(t) + \xi(t)\Psi_1\right)\delta\left(x - L1\right)\right] \\
&-\tfrac{\partial}{\partial x}\left[h\left(F_c(t) + \xi(t)\Psi_1\right)\delta\left(x - L2\right)\right] \\
&+\tfrac{\partial}{\partial x}\left[h\left(F_d(t) + \xi(t)\Psi_2\right)\delta\left(x - L3\right)\right] \\
&-\tfrac{\partial}{\partial x}\left[h\left(F_d(t) + \xi(t)\Psi_2\right)\delta\left(x - L4\right)\right] = 0
\end{aligned} \tag{185}$$

If it assumed that the trial function is the first mode of equation (163) then the test function is defined by eqn. (179).

Equation (185) is multiplied by (179) and integrated over the length of the beam to give

$$\begin{aligned} & m\int_0^L \phi^2(x)dx\ddot{\xi}(t) + \left(EI\int_0^L \phi(x)\phi''''(x)dx + \Psi_1\Psi_3 + \Psi_2\Psi_4\right)\xi(t) \\ & = -h\Psi_3 F_c(t) - h\Psi_4 F_d(t) \end{aligned} \tag{186}$$

where

$$\Psi_3 = \phi'(L1) - \phi'(L2) \tag{187}$$

Rearranging eqn. (186) and substituting eqn. (168) and (169) gives

$$\ddot{\xi}(t) + \omega_s^2\xi(t) = \Upsilon_c\eta_1(t) - \Upsilon_d F_d(t) \tag{188}$$

where

$$\omega_s^2 = \frac{\left(EI\int_0^L \phi(x)\phi''''(x)dx + \Psi_1\Psi_3 + \Psi_2\Psi_4\right)}{m\int_0^L \phi^2(x)dx} \tag{189}$$

$$\Upsilon_c = \frac{h\Psi_3}{m\int_0^L \phi^2(x)dx} A_s Y_s^E d_{33}\frac{\gamma_i\alpha}{t_{layer}} \tag{190}$$

$$\Upsilon_d = \frac{h\Psi_4}{m\int_0^L \phi^2(x)dx} \tag{191}$$

The form of the controller is a second order system and is written as follows

$$\ddot{\eta}_n(t) + 2\omega_n\zeta_n\dot{\eta}_n(t) + \omega_n^2\eta_n(t) = \beta\ddot{v}(L,t) = \beta\ddot{\xi}_n(t)\phi_n(L) = V_o(t) \tag{192}$$

where $\eta(t)$ is in volts.

The control voltage is shown to be

$$u(t) = V_c(t) = \Gamma\hat{\beta}\ddot{\eta}(t) = \Gamma\omega^2\eta(t) \tag{193}$$

where Γ is the controller gain.

Given the system model, with additional structural damping for the first mode

$$\ddot{\xi}(t) + 2\omega_{s1}\zeta_{s1}\dot{\xi}_1(t) + \omega_{s1}^2\xi(t) = \Upsilon_c\eta_1(t) - \Upsilon_d F_d(t) \tag{194}$$

In the Laplace domain this becomes

$$\begin{aligned}\Xi_1(s)s^2 + 2\omega_{s1}\zeta_{s1}\Xi_1(s)s + \omega_{s1}^2\Xi_1(s) &= \Upsilon_c\omega_{c1}^2\bar{\eta}_i(s) - \Upsilon_d\bar{F}_d(s)\\ \bar{\eta}_1(s)s^2 + 2\omega_{c1}\zeta_{c1}\bar{\eta}_1(s)s + \omega_{c1}^2\bar{\eta}_1(s) &= \Xi_1(s)s^2b\end{aligned} \tag{195}$$

Subscripts s and c identify structure and controller respectively.

To account for geometric location of the actuator and sensor, b is defined as the sensor influence coefficient and a_1 is the actuator influence coefficient.

Solving eqn.(195b) for $\Xi_1(s)$

$$\Xi_1(s) = \frac{\bar{\eta}_1(s)(s^2 + 2\omega_{c1}\zeta_{c1}s + \omega_{c1}^2)}{s^2b} \tag{196}$$

Equation (196) is substituted into eqn.(195) to give

$$\frac{\bar{\eta}_1(s)(s^2 + 2\omega_{c1}\zeta_{c1}s + \omega_{c1}^2)}{s^2b}(s^2 + 2\omega_{s1}\zeta_{s1} + \omega_{s1}^2) = a_1\Upsilon_c\omega_{c1}^2\bar{\eta}_1(s) - \Upsilon_d\bar{F}_d(s) \tag{197}$$

Equation (197) is used to show the transfer function between the disturbance voltage and the control signal as

$$\frac{\bar{\eta}_1(s)}{\bar{F}_d(s)} = \frac{\Upsilon_d s^2 b}{((s^2 + 2\omega_{c1}\zeta_{c1}s + \omega_{c1}^2)(s^2 + 2\omega_{s1}\zeta_{s1} + \omega_{s1}^2) - a_1\Upsilon_c\omega_{c1}^2 s^2 b)} \tag{198}$$

Appendix D

LIAPUNOV EQUATION

Consider the homogeneous linear system

$$\dot{\mathbf{x}} = \mathbf{A}\mathbf{x} \tag{199}$$

where **A** is the state matrix and **x** is the state vector. The Liapunov equation associated with this system is given as[42]

$$\bar{A}^T B + B\bar{A} = -C \tag{200}$$

where C is assumed positive semi-definite and B is the symmetric positive definite unknown array of the desired Liapunov function. This equation is typically used to determine stability when the Liapunov function is of first order form. The Liapunov function is of the form

$$V(x) = x^T B x \tag{201}$$

If this is differentiated

$$\frac{d}{dt}[V(x)] = \dot{x}^T B x + x^T B \dot{x} \tag{202}$$

Substituting (199) into (202) yields

$$\begin{aligned} &\tfrac{d}{dt}\left[V(x)\right] = x^T A^T B x + x^T B A x \\ &= x^T \left(A^T B + BA\right) x \\ &= -x^T C x \end{aligned} \tag{203}$$

If V(x) is to be a Liapunov function the matrix C has to be positive semi-definite and B must be chosen so that it satisfies eqn.(200).

REFERENCES

[1] *Frequency Domain System Identification Toolbox for MATLAB v. 3.3.*

[2] Anderson, W. D., Patel, S. R., and Black, C. L., "Low-speed wind tunnel buffet testing on the f-22," *Journal of Aircraft*, vol. 43, pp. 879–85, July-Aug 2006.

[3] Appa, K., Ausman, J., Khot, J. N. S., and Brenner, M. J., "Buffet load alleviation using a smart actuation system," in *Collection of Technical Papers - AIAA/ASME/ASCE/AHS/ASC Structures, Structural Dynamics and Materials Conference*, vol. 5, pp. 3568–3578, 2001.

[4] Ashley, H., Rock, S. M., Digumarthi, R., Channey, K., and Eggers, A. J., "Active control for fin buffet alleviation," Tech. Rep. WL-TR-93-3099, NASA, 1994.

[5] Bachalo, W. D., "Experiments on supersonic boundary-layer separation in three dimensions," *Journal of Applied Mechanics, Transactions ASME*, vol. 42, no. 2, pp. 289–294, 1975.

[6] Balas, M., "Active control of flexible systems," *Journal of Optimization Theory and Applications*, vol. 25, pp. 415–436, July 1978.

[7] Bisplinghoff, R. L., Ashley, H., and Halfman, R. L., *Aeroelasticity*. Cambridge, Mass., Addison-Wesley Pub. Co., 1955.

[8] Bowong, S., "Adaptive synchronization of chaotic systems with unknown bounded uncertainties via backstepping approach," *Nonlinear Dynamics*, vol. 49, pp. 59 – 70, 2007.

[9] Breitsamter, C. and Laschka, B., "Aerodynamic active control for ef-2000 fin buffet load alleviation," in *Aerospace Sciences Meeting and Exhibit*, 2000.

[10] Burnham, J. K., Pitt, D. M., White, E. V., Henderson, D. A., and Moses, R. W., "An advanced buffet load alleviation system," in *Collection of Technical Papers - AIAA/ASME/ASCE/AHS/ASC Structures, Structural Dynamics and Materials Conference*, vol. 5, pp. 3579–3588, 2001.

[11] Calise, A. J., Lee, S., and Sharma, M., "Development of a reconfigurable flight control law for tailless aircraft," *Journal of Guidance, Control, and Dynamics*, vol. 24, pp. 896–902, 2001.

[12] Calise, A. J., Yang, B.-J., and Craig, J. I., "Augmentation of an existing linear controller with an adaptive element," in *Proceedings of the American Control Conference*, vol. 2, pp. 1549–1554, 2002.

[13] Calise, A. J., Yang, B.-J., and Craig, J. I., "Augmenting adaptive approach to control of flexible systems," *Journal of Guidance, Control, and Dynamics*, vol. 27, pp. 387–396, May/June 2004.

[14] de Noyer, M. B. and Hanagud, S., "Comparison of h2 optimized design and crossover point design for acceleration feedback control," in *Collection of Technical Papers - AIAA/ASME/ASCE/AHS/ASC Structures, Structural Dynamics & Materials Conference*, vol. 4, pp. 3250–3258, 1998.

[15] de Noyer, M. B. and Hanagud, S., "Single actuator and multi-mode acceleration feedback control," *Journal of Intelligent Material Systems and Structures*, vol. 9, no. 7, pp. 522–533, 1998.

[16] de Noyer, M. P. B., Roberts, P., and Hanagud, S., "Active damping by acceleration feedback control and redistribution of stresses in the structure," in *American Society of Mechanical Engineers, Aerospace Division*, vol. 59, pp. 373–380, 1999.

[17] Drakunov, S. V., Ozguner, U., and Lenning, L., "Use of neural networks and sliding modes in vibration damping," in *Proceedings of SPIE - The International Society for Optical Engineering*, vol. 1919, pp. 174–181, 1993.

[18] El-Badawy, A. A. and Nayfeh, A. H., "Buffet alleviation of twin-tailed fighter aircraft using saturation-based control," in *Proceedings of the International Modal Analysis Conference - IMAC*, vol. 2, pp. 928–934, 2001.

[19] El-Badawy, A. A. and Nayfeh, A. H., "Use of linear and nonlinear vibration absorbers for buffet alleviation of twin-tailed fighter aircraft," in *Proceedings of the SPIE - The International Society for Optical Engineering*, vol. 4326, pp. 397–407, 2001.

[20] Ferman, M. A., Huttsell, L. J., and Turner, E. W., "Experiments with tangential blowing to reduce buffet response on an f-15 model," *Journal of Aircraft*, vol. 41, pp. 903–910, July/August 2004.

[21] Ferman, M. A., Liguore, S. L., Smith, C. M., and Colvin, B. J., "Composite 'exoskin' doubler extends f-15 vertical tail fatigue life," in *Collection of Technical Papers - AIAA/ASME Structures, Structural Dynamics and Materials Conference*, no. n pt 1, pp. 398–407, 1993.

[22] Flynn, G. A., Morrison, J. F., and Mabey, D. G., "Buffet alleviation on swept and unswept wings at high incidence," *Journal of Aircraft*, vol. 38, no. 2, pp. 368–378, 2001.

[23] Frasier, R. A. and Duncan, W. J., "The accident investigation sub-committee on the accident to the aeroplane g-aazk at meopham, kent, england on july 21, 1930," Tech. Rep. 1360, British R&M, July 1933.

[24] Funahashi, K., "On the approximate realization of continuous mappings by neural networks," *Neural Networks*, vol. 2, no. 3, pp. 183 –192, 1989.

[25] Fung, Y., *An introduction to the theory of aeroelasticity.* Galcit aeronautical series, New York, Wiley, 1955.

[26] Gee, K., Murman, S. M., and Schiff, L. B., "Computation of f/a-18 tail buffet," *Journal of Aircraft*, vol. 33, pp. 1181–1189, Nov-Dec 1996.

[27] Gee, K., Rizk, Y. M., and Schiff, L. B., "Forebody tangential slot blowing on an aircraft geometry," *Journal of Aircraft*, vol. 31, pp. 922–928, July-Aug 1994.

[28] Ghee, T. A., Gonzalez, H. A., and Findlay, D. B., "Tail buffet alleviation through the use of wing-strake fillet shapes," *Journal of Aircraft*, vol. 39, pp. 100–108, January/February 2002.

[29] Goh, C. J. and Yan, W. Y., "Approximate pole placement for acceleration feedback control of flexible structures," *Journal of Guidance, Control, and Dynamics*, vol. 19, pp. 256–9, Jan.-Feb 1996.

[30] H. Demuth, M. B., *Neural Network Toolbox User's Guide*. The Mathworks Inc.

[31] Hanagud, S., de Noyer, M. B., Luo, H., Henderson, D., and Nagaraja, K. S., "Tail buffet alleviation of high performance twin tail aircraft using piezo-stack actuators," in *Collection of Technical Papers - AIAA/ASME/ASCE/AHS/ASC Structures, Structural Dynamics and Materials Conference*, vol. 2, pp. 1054–1064, 1999.

[32] Hanagud, S., de Noyer, M. B., Luo, H., Henderson, D., and Nagaraja, K. S., "Tail buffet alleviation of high-performance twin-tail aircraft using piezostack actuators," *AIAA Journal*, vol. 40, pp. 619–627, April 2002.

[33] Hanagud, S., Luo, H., and Lestari, W., "Detection of an edge notch defect by using a single mode based methods," in *43rd Structures, Structural Dynamics and Materials Conference*, vol. 2, pp. 989–998, 2002.

[34] Harter, J., "Damage tolerance management of the x-29 vertical tail." In AGARD, An Assessment of Fatigue Damage and Crack Growth Prediction Techniques, 1994.

[35] Hauch, R. M., Jacobs, J. H., Ravindra, K., and Dima, C., "Reduction of vertical tail buffet response using active control," *Journal of Aircraft*, vol. 33, pp. 617–622, May-June 1996.

[36] Healey, M. D., "F/a-18 e/f vertical tail buffet design, analysis and test," in *44th AIAA/ASME/ASCE/AHS/ASC Structures, Structural Dynamics, and Materials Conference*, vol. 6 of *Collection of Technical Papers - AIAA/ASME/ASCE/AHS/ASC Structures, Structural Dynamics and Materials Conference*, pp. 4415–4426, 2003.

[37] Hebbar, S. K., Platzer, M. F., and Frink, W. D., "Effect of leading-edge extension fences on the vortex wake of an f/a-18 model," *Journal of Aircraft*, vol. 32, pp. 680–682, May-Jun 1995.

[38] Hibbitt, Karlsson & Sorensen, I., "Abaqus/standard user guide, version 5.8," 1997.

[39] Hovakimyan, N. and Calise, A., "Adaptive output feedback control of uncertain multi-input multi-output systems using single hidden layer neural networks," in *Proceedings of the 2002 American Control Conference*, 2002.

[40] Hovakimyan, N., Nardi, F., Calise, A. J., and Kim, N., "Adaptive output feedback control of uncertain systems using single hidden layer neural networks," *IEEE Transactions on Neural Networks*, vol. 13, pp. 1420–1431, Nov. 2002.

[41] Humphreys, Q., Shi, P., and Gao, H., "Adaptive variable structure and commanding shaped vibration control of flexible spacecraft," *Journal of Guidance, Control, and Dynamics*, vol. 30, pp. 804–815, 2007.

[42] Inman, D. J., *Vibration : with control, measurement, and stability*. Englewood Cliffs, N.J. : Prentice Hall, 1989.

[43] Jacobs, J. H., Hedgecock, C. E., Lichtenwalner, P. F., Pado, L. E., and Washburn, A. E., "Use of artificial intelligence for buffet environments," in *Collection of Technical Papers - AIAA/ASME Structures, Structural Dynamics and Materials Conference*, pp. 1952–1960, 1993.

[44] Jha, R. and He, C., "Design and experimental validation of adaptive neurocontroller for beam vibration suppression using piezoelectric actuators," in *2001 ASME*

International Mechanical Engineering Congress and Exposition, vol. 64 of *American Society of Mechanical Engineers, Aerospace Division (Publication) AD*, pp. 271–281, American Society of Mechanical Engineers, 2001.

[45] Juang, J. N. and Phan, M., "Robust controller designs for second-order dynamic systems: a virtual passive approach," *Journal of Guidance, Control, and Dynamics*, vol. 15, pp. 1192–8, Sept.-Oct. 1992.

[46] Kandil, O. A., Yang, Z., and You, R., "Effectiveness of adaptive flow control for twin-tail buffet," in *AIAA Applied Aerodynamics Conference, 18th*, pp. 714–724, 2000.

[47] Kandil, O. A., Massey, S. J., and Kandil, H. A., "Computations of vortex-breakdown induced tail buffet undergoing bending and torsional vibrations," in *Collection of Technical Papers - AIAA/ASME/ASCE/AHS/ASC Structures, Structural Dynamics & Materials Conference*, no. 2, pp. 977–992, 1994.

[48] Komerath, N. M., Liou, S. G., Schwartz, R. J., and Kim, J. M., "Flow over a twin-tailed aircraft at angle of attack. part i. spatial characteristics," *Journal of Aircraft*, vol. 29, pp. 413–420, May-June 1992.

[49] Komerath, N. M., Schwartz, R. J., and Kim, J. M., "Flow over a twin-tailed aircraft at angle of attack, part ii. temporal characteristics," *Journal of Aircraft*, vol. 29, pp. 553–558, Jul-Aug 1992.

[50] Lazarus, K. B., Saarmaa, E., and Agnes, G. S., "Active smart material system for buffet load alleviation," in *Proceedings of SPIE - The International Society for Optical Engineering*, vol. 2447, pp. 179–192, 1995.

[51] Lee, B. H. K., "Vertical tail buffeting of fighter aircraft," *Progress in Aerospace Sciences*, vol. 36, pp. 193–279, Apr-May 2000.

[52] Lee, B. H. K. and Brown, D., "Wind-tunnel studies of f/a-18 tail buffet," *Journal of Aircraft*, vol. 29, pp. 146–152, Jan-Feb 1992.

[53] Lestari, W., *Damage of composite structures : detection technique, dynamic response and residual strength.* PhD thesis, School of Aerospace Engineering, Georgia Institute of Technology, 2001.

[54] Lewis, F. L., Yesildirek, A., and Liu, K., "Multilayer neural-net robot controller with guaranteed tracking performance," *IEEE Transactions on Neural Networks*, vol. 7, pp. 388–399, March 1996.

[55] Lichtenwalner, P. F., Little, G. R., Pado, L. E., and Scott, R. C., "Adaptive neural control for active flutter suppression," in *American Society of Mechanical Engineers, Fluids Engineering Division (Publication) FED*, vol. 242, pp. 3–8, 1996.

[56] Lichtenwalner, P. F., Little, G. R., and Scott, R. C., "Adaptive neural control of aeroelastic response," in *Proceedings of SPIE - The International Society for Optical Engineering*, vol. 2717, pp. 199–209, 1996.

[57] Long, T. W., Hanzevack, E. L., and Caggiano, S., "Noncolocated vibration control using neural networks," in *Proceedings of the 1995 IEEE International Symposium on Intelligent Control*, pp. 9–14, 1995.

[58] Lu, Z., Shi, X., Wang, X., and Xu, M., "Active structure vibration control using dynamic neural networks: modeling error, nonlinear, parameter imprecise and disturbance," in *American Society of Mechanical Engineers, Design Engineering Division*, vol. 93, pp. 363–370, 1996.

[59] Luo, Q. and Tong, L., "Exact static solutions to piezoelectric smart beams including peel stresses. ii. numerical results, comparison and discussion," *International Journal of Solids and Structures*, vol. 39, no. 18, pp. 4697–4722, 2002.

[60] Mattice, M. and Vigna, C. L., "Innovative active control of gun barrels using smart materials," in *Proceedings of SPIE - The International Society for Optical Engineering*, vol. 3039, pp. 630–641, 1997.

[61] Meyn, L. A. and James, K. D., "Full-scale wind-tunnel studies of f/a-18 tail buffet," *Journal of Aircraft*, vol. 33, pp. 589–595, May-June 1996.

[62] Moore, J. W., Spangler, R. L., Lazarus, K. B., and Henderson, D. A., "Buffet load alleviation using distributed piezoelectric actuators," in *American Society of Mechanical Engineers, Aerospace Division*, vol. 52, pp. 485–490, 1996.

[63] Morton, S. A., Cummings, R. M., and Kholodar, D. B., "High resolution turbulence treatment of f/a-18 tail buffet," in *45th AIAA/ASME/ASCE/AHS/ASC Struct., Struct. Dyn. and Mater. Conf.; 12th AIAA/ASME/AHS Adapt. Struct. Conf.; 6th AIAA Non-Deterministic Approaches Forum; 5th AIAA Gossamer Spacecraft Forum*, vol. 3 of *Collection of Technical Papers - AIAA/ASME/ASCE/AHS/ASC Structures, Structural Dynamics and Materials Conference*, pp. 1811–1823, 2004.

[64] Moses, R. W., "Vertical-tail-buffeting alleviation using piezoelectric actuators: some results of the actively controlled response of buffet-affected tails (acrobat) program," in *Proceedings of SPIE - The International Society for Optical Engineering*, vol. 3044, pp. 87–98, 1997.

[65] Moses, R. W., "Contributions to active buffeting alleviation programs by the nasa langley research center," in *Collection of Technical Papers - AIAA/ASME/ASCE/AHS/ASC Structures, Structural Dynamics and Materials Conference*, vol. 2, pp. 1034–1042, 1999.

[66] Narendra, K., *Handbook of intelligent control : neural, fuzzy, and adaptive approaches*. New York : Van Nostrand Reinhold, 1992.

[67] Nersesov, S. G. and Haddad, W. M., "On the stability and control of nonlinear dynamical systems via vector lyapunov functions," *IEEE TRANSACTIONS ON AUTOMATIC CONTROL,*, vol. 51, pp. 203–215, 2006.

[68] Nitzsche, F., Zimcik, D. G., and Langille, K., "Active control of vertical fin buffeting with aerodynamic control surface and strain actuation," in *Collection of*

Technical Papers - AIAA/ASME/ASCE/AHS/ASC Structures, Structural Dynamics & Materials Conference, vol. 2, pp. 1467–1477, 1997.

[69] Nitzsche, F., Zimcik, D. G., Ryall, T. G., Moses, R. W., and Henderson, D. A., "Control law synthesis for vertical fin buffeting alleviation using strain actuation," tech. rep., AIAA, 1999.

[70] Nitzsche, F., Zimcik, D. G., Ryall, T. G., Moses, R. W., and Henderson, D. A., "Closed-loop control tests for vertical fin buffeting alleviation using strain actuation," *Journal of Guidance, Control, and Dynamics*, vol. 24, no. 4, pp. 855–857, 2001.

[71] Noyer, M. P. B. D., *Tail buffet alleviation of high performance twin tail aircraft using offset piezoceramic stack actuators and acceleration feedback control*. PhD thesis, Georgia Institute of Technology, 2000.

[72] Outman, V. and Lambert, A., "Transonic separation," *Journal of the Aeronautical Sciences*, vol. 15, pp. 671–674, November 1948.

[73] Pado, L. E. and Jacobs, J. H., "Hybrid cascading neural network for modeling fighter aircraft buffet pressures," in *Intelligent Engineering Systems Through Artificial Neural Networks*, vol. 3, pp. 877–884, ASME, November 1993.

[74] Pado, L. E. and Lichtenwalner, P. F., "Neural predictive control for active buffet alleviation," in *Collection of Technical Papers - AIAA/ASME/ASCE/AHS/ASC Structures, Structural Dynamics and Materials Conference*, vol. 2, pp. 1043–1053, 1999.

[75] Pado, L. E., Lichtenwalner, P. F., Liguore, S. L., and Drouin, D., "Neural predictive control for active buffet alleviation," in *Proceedings of SPIE - The International Society for Optical Engineering*, vol. 3326, pp. 47–57, 1998.

[76] Pado, L. E. and Damle, R. R., "Predictive neuro control of vibration in smart structures," in *Proceedings of SPIE - The International Society for Optical Engineering*, vol. 2715, pp. 567–575, 1996.

[77] Pan, Y.-J., Marquez, H., and Chen, T., "Robust output feedback tracking control for a class of mimo nonlinear systems," in *American Control Conference, 2005. Proceedings of the 2005*, 2005.

[78] Pearcey, H. H., "Method for prediction of onset of buffeting and other separation effects from wind tunnel tests on rigid models," AGARD – Reports 223, North Atlantic Treaty Organization (NATO), Paris, France, 1958.

[79] Pettit, C. L., Brown, D. L., Banford, M. P., and Pendleton, E., "Full-scale wind-tunnel pressure measurements of an f/a-18 tail during buffet," *Journal of Aircraft*, vol. 33, pp. 1148–1156, Nov-Dec 1996.

[80] PI, P., "www.polytecpi.com (06-15-03)."

[81] Preumont, A., Dufour, J. P., and Malekian, C., "Active damping by a local force feedback with piezoelectric actuators," *Journal of Guidance, Control, and Dynamics*, vol. 15, pp. 390–395, Mar-April 1992.

[82] Redmond, J. and Barney, P., "Vibration control of stiff beams and plates using structurally integrated pzt stack actuators," *Journal of Intelligent Material Systems and Structures*, vol. 8, pp. 525–535, June 1997.

[83] Roberts, P., de Noyer, M. B., and Hanagud, S., "Nonlinear effects of the offset piezoceramic stack actuator," in *Collection of Technical Papers - AIAA/ASME/ASCE/AHS/ASC Structures, Structural Dynamics and Materials Conference*, 2000.

[84] Rock, S., Ashley, H., Digumarthi, R., and Chaney, K., "Active control for fin buffet alleviation," in *AIAA Guidance, Navigation and Control Conference, Monterey, CA.*, pp. 1051–1056, 1993.

[85] Sastry, S., *Nonlinear systems : analysis, stability, and control*. New York : Springer, 1999.

[86] Scott, R. C., "Active control of wind-tunnel model aeroelastic response using neural networks," in *Proceedings of SPIE - The International Society for Optical Engineering*, vol. 3991, pp. 232–243, 2000.

[87] Seeman, W., Wolf, K., Straub, A., Hagedorn, P., and Chang, F., "Bonding stresses between piezoelectric actuators and elastic beams," in *Proceedings of SPIE - The International Society for Optical Engineering*, vol. 3041, pp. 665–675, 1997.

[88] Sharma, M. and Calise, A. J., "Neural-network augmentation of existing linear controllers," *Journal of Guidance, Control, and Dynamics*, vol. 28, pp. 12–19, January/February 2005.

[89] Sheta, E. F., "Effect of stream-wise fences on twin-tail buffet responses," in *AIAA Applied Aerodynamics Conference*, pp. 703–713, 2000.

[90] Sheta, E. F., Harrand, L. J., and Huttsell, L. J., "Active vortical flow control for alleviation of twin-tail buffet of generic fighter aircraft," *Journal of Fluids and Structures*, vol. 15, pp. 769–789, August 2001.

[91] Sheta, E. F., "Buffet alleviation of f/a-18 aircraft using lex fences," in *44th AIAA/ASME/ASCE/AHS/ASC Structures, Structural Dynamics, and Materials Conference*, vol. 6 of *Collection of Technical Papers - AIAA/ASME/ASCE/AHS/ASC Structures, Structural Dynamics and Materials Conference*, pp. 4438–4448, 2003.

[92] Sheta, E. F., "A multidisciplinary analysis of tail buffeting alleviation using stream-wise fences," *Journal of Vibration and Control*, vol. 9, pp. 583–604, May 2003.

[93] Sheta, E. F., "Alleviation of vertical tail buffeting of f/a-18 aircraft," *Journal of Aircraft*, vol. 41, pp. 322–330, March/April 2004.

[94] Sheta, E. F., Moses, R. W., Huttsell, L. J., and Harrand, V. J., "Active control of f/a-18 vertical tail buffeting using piezoelectric actuators," in *44th*

AIAA/ASME/ASCE/AHS/ASC Structures, Structural Dynamics, and Materials Conference, vol. 6 of *Collection of Technical Papers - AIAA/ASME/ASCE/AHS/ASC Structures, Structural Dynamics and Materials Conference*, pp. 4427–4437, 2003.

[95] Sim, E. and Lee, S. W., "Active vibration control of flexible structures with acceleration feedback," *Journal of Guidance, Control, and Dynamics*, vol. 16, pp. 413–415, Mar-Apr 1993.

[96] Soderman, P. T. and Aiken, T. N., "Full-scale wind-tunnel tests of a small unpowered jet aircraft with a t-tail," Tech. Rep. NASA-TN-D-6573, NASA, 1971.

[97] Spangler, R. L. and Jacques, R. N., "Testing of an active smart material system for buffet load alleviation," in *Collection of Technical Papers - AIAA/ASME/ASCE/AHS/ASC Structures, Structural Dynamics and Materials Conference*, vol. 2, pp. 1023–1033, 1999.

[98] Spencer, M. G., Sanner, R. M., and Chopra, I., "Adaptive neurocontroller for vibration suppression and shape control of a flexible beam," *Journal of Intelligent Material Systems and Structures*, vol. 9, pp. 160–170, March 1998.

[99] Suleman, A., Costa, A. P., and Moniz, P. A., "Experimental flutter and buffeting suppression using piezoelectric actuators and sensors," in *Proceedings of the SPIE - The International Society for Optical Engineering*, vol. 3674, pp. 72–81, 1999.

[100] Tai, T. C., "Flow separation patterns over an f-14a aircraft wing," *Journal of Aircraft*, vol. 28, pp. 818–827, December 1991.

[101] Tavoularis, S., Marineau-Mes, S., and Lee, B. H. K., "Tail buffet of f/a-18 at high incidence with sideslip and roll (part 1)," *Journal of Aircraft*, vol. 38, pp. 10–16, Jan. 2001.

[102] Tavoularis, S., Marineau-Mes, S., and Lee, B. H. K., "Tail buffet of f/a-18 at high incidence with sideslip and roll (part 2)," *Journal of Aircraft*, vol. 38, pp. 17–21, Jan. 2001.

[103] Varadan, V. V., Young-Hun, L., and Varadan, V. K., "Closed loop finite-element modeling of active/passive damping in structural vibration control," *Smart Materials and Structures*, vol. 5, pp. 685–694, Oct. 1996.

[104] Wang, T. C. and Sinha, A., "Active structure vibration control using dynamic neural networks: modeling error, nonlinear, parameter imprecise and disturbance," in *American Society of Mechanical Engineers, Design Engineering Division*, vol. 93, pp. 363–370, 1996.

[105] Yang, B., Craig, J., Hovakimyan, N., and Calise, A., "Experimental validation of an augmenting approach to adaptive control of uncertain nonlinear systems," in *AIAA Guidance, Navigation, and Control Conference and Exhibit*, 2003.

[106] Yang, B.-J., Calise, A. J., and Craig, J. I., "Adaptive output feedback control of a flexible base manipulator," *JOURNAL OF GUIDANCE, CONTROL, AND DYNAMICS*, vol. 30, pp. 1068–1080, 2007.

[107] Yang, B.-J., Hovakimyan, N., and Calise, A. J., "Output feedback control of an uncertain system using an adaptive observer," in *42nd IEEE Conference on Decision and Control*, vol. 2 of *Proceedings of the IEEE Conference on Decision and Control*, pp. 1705–1710, 2003.

[108] Young, J. W. and Hansen, C. H., "Control of flexural vibration in stiffened structures using multiple piezoceramic actuators," *Applied Acoustics*, vol. 49, pp. 17–48, Sep. 1996.